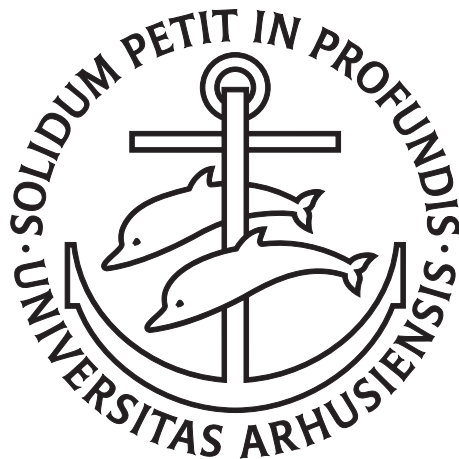

Applications of Nonlinear Optics and Optical Fibers



Thomas Vestergaard Andersen

Department of Physics and Astronomy &
NKT Academy, Department of Chemistry
University of Aarhus, Denmark

PhD thesis

April 2006

This thesis is submitted to the Faculty of Science at the University of Aarhus, Denmark, in order to fulfill the requirements for obtaining the PhD degree in Physics. The studies have been carried out at the Department of Physics and Astronomy under the supervision of Prof. Søren Keiding.



List of Publications

Journals:

- [I] *High-power intracavity frequency doubling of a Ti:Sapphire femtosecond oscillator.*
T. V. Andersen, J. Thøgersen, S. R. Keiding, J. J. Larsen. Appl. Phys. B, Vol **76** (6), 639-644 (2003).
- [II] *Supercontinuum generation in a photonic crystal fiber with two zero dispersion wavelengths.*
K. M. Hilligsøe, T. V. Andersen, H. N. Paulsen, C. K. Nielsen, K. Mølmer, S. R. Keiding, R. Kristiansen, K. P. Hansen, J. J. Larsen. Opt. Express, **12**, 1045 (2004).
- [III] *Continuous-wave wavelength conversion in a photonic crystal fiber with two closely lying zero dispersion wavelengths.*
T. V. Andersen, K. M. Hilligsøe, C. K. Nielsen, J. J. Larsen, J. Thøgersen, S. R. Keiding. Optics Express, **12** (17), 4113 (2004).
- [IV] *Stability analysis of an all-fiber coupled cavity Fabry-Perot additive pulse modelocked laser.*
C. K. Nielsen, T. V. Andersen, S. R. Keiding. J. Quantum Electronics **41** (2), 198 (2005).
- [V] *All-fiber actively Q-switched Yb-laser.*
T. V. Andersen, P. Perez-Milan, R. Duchowicz, S. R. Keiding, S. Agger, M. Andrés. Opt. Comm. **260** (1), 251 (2006)
- [VI] *Supercontinuum generation by femtosecond single and dual wavelength pumping in photonic crystal fibers with two zero dispersion wavelengths.*
T. Schreiber, T. V. Andersen, D. Schimpf, J. Limpert, A. Tünnermann. Optics Express **13**, 9556-9569 (2005)

- [VI] *High repetition rate tunable femtosecond pulses and broadband amplification from a fiber laser pumped parametric amplifier.*
T. V. Andersen, O. Schmidt, J. Limpert, A. Tünnermann, C. Aguergaray, E. Cormier. *Optics Express* **14**, 4765-4773 (2006)

Conference Contributions:

- [i] *Large mode area photonic crystal fiber laser passively Q-switched with Cr⁴⁺:YAG.*
S. Buchter, Y. Qian, T. V. Andersen, J. R. Folkenberg, C. F. Pedersen, P. M. Skovgård, H. Simonsen. The proceedings of SPIE Conference, 2004.
- [ii] *Supercontinuum generation in a photonic crystal fiber with two closely lying zero dispersion wavelengths.*
K. M. Hilligsøe, T. V. Andersen, H. N. Paulsen, C. K. Nielsen, K. Mølmer, S. R. Keiding, R. Kristiansen, K. P. Hansen, J. J. Larsen. CLEO/IQEC and PhAST Technical Digest on CDROM (The Optical Society of America, Washington, DC, 2004), CWK5.
- [iii] *Supercontinuum generation by femtosecond single and dual wavelength pumping in photonic crystal fibers with two zero dispersion wavelengths.*
T. Schreiber, T. V. Andersen, D. Schimpf, J. Limpert, A. Tünnermann. Photonics West, San José, 2006
- [iv] *High repetition rate tunable femtosecond pulses and broadband amplification from fiber laser pumped parametric amplifier.*
T. V. Andersen, O. Schmidt, J. Limpert, A. Tünnermann, C. Aguergaray, E. Cormier. Advanced Solid State Photonics (ASSP), Lake Tahoe, 2006
- [iv] *Ultrashort pulse generation by fiber laser pumped parametric amplification.*
T. V. Andersen, O. Schmidt, J. Limpert, A. Tünnermann, C. Aguergaray, E. Cormier. CLEO/IQEC and PhAST, Long Beach, California, 2006

Contents

Contents	v
1 Introduction	1
2 Nonlinear optics and optical fibers	7
2.1 Nonlinear optics	8
2.2 Basic properties of optical fibers	10
2.2.1 The nonlinear Schrödinger equation	12
2.2.2 Dispersion	13
2.2.3 Self phase modulation	16
2.3 Rare Earth doped fibers	17
2.4 Photonic crystal fibers	19
2.5 Super continuum generation in PCFs	22
3 Intracavity frequency doubling of a Ti:Sapphire oscillator	25
3.1 Introduction	26
3.2 Intracavity second harmonic generation	26
3.2.1 Setup	26
3.2.2 Cavity dispersion	29
3.2.3 Characterization	30
3.3 Optical parametric amplification	31
3.4 Summary	32
4 Continuous wave four-wave mixing in a photonic crystal fiber	35
4.1 Introduction	36
4.2 Four wave mixing	36
4.3 Phasematching in CF NL-PM-750	38
4.4 Experimental results	40
4.5 Summary	43

5	Q-switched fiber laser	45
5.1	Introduction	46
5.2	Experimental setup	47
5.3	Results	50
5.4	Outlook	53
5.5	Summary	54
6	Fiber dispersion measurements with white-light interferometry	57
6.1	Introduction	58
6.2	Experimental setup	59
6.3	Theory	60
6.4	Example - HC 1060-02 air guiding fiber	61
6.5	Summary	64
7	Dual-wavelength pumping of photonic crystal fibers	65
7.1	Introduction	66
7.2	Experimental setup	66
7.3	Results	67
7.4	Picosecond dual-wavelength pumping	72
7.5	Nanosecond dual-wavelength pumping	73
7.6	Summary	74
8	Fiber laser pumped optical parametric amplifier	75
8.1	Introduction	76
8.2	Theory of optical parametric amplification	77
8.2.1	Non-collinear optical parametric amplification	79
8.3	Experimental setup	81
8.4	Tunable parametric amplification	83
8.4.1	Broadband phasematching	83
8.4.2	Narrowband phasematching	84
8.5	Short-pulse amplification	86
8.6	Summary and outlook	90
9	Summary and acknowledgements	91
9.1	Summary	92
9.1.1	Perspectives	93
9.2	Acknowledgements	94
A	List of abbreviations	95
B	Numerical model	97
	References	105

Chapter 1

Introduction

Optical fibers are probably one of the most important scientific achievements in the last century. They form the backbone of our communication infrastructure and allow us to access almost any information in a matter of seconds through the internet. But there is more to optical fibers than their well-known ability to guide signals around the globe and this thesis will investigate some of their alternative applications.

This project is a collaboration between the Århus University and the NKT-Photonics group. NKT-Photonics is a constellation of relatively small spin-off companies of which three have been relevant for the work presented here: Koheras, Crystal Fibre and NKT-Research & Innovation (NKT-Research). Koheras produces various types of fiber lasers, mainly for sensing and surveillance purposes, while Crystal Fibre is manufacturing a special type of optical fibers - the photonic crystal fibers (PCFs). NKT-Research carries out relevant basic research to support further development of the companies within the NKT-Photonics group.

The NKT-Photonics adventure really took off in the year 2000 when the NKT-owned spin-off company, Giga was sold to Intel for about 1.3 billion Euros. The sale spurred further growth of other spin-offs - among those Koheras and Crystal Fibre - and significant investments were made in production facilities and fundamental research. Additionally, the NKT-Academy [1] was founded and numerous photonics-related PhD-projects were initiated in Denmark and abroad. At the University of Århus, the present and three additional NKT-Academy PhD-projects were started in 2001-2002 in collaboration with Søren Keiding at the Institute of Chemistry. The initial work was focused on understanding and using the properties of the recently emerged PCFs made by Crystal Fibre. The new fibers drew much attention at the time, mostly because of the spectacular super continuum generation which had been demonstrated by Herrmann in 2001 [2, 3]. The prospect of using the demonstrated bandwidth of more than 1000 nm for telecommunication purposes brought the PCFs to the front pages and rose the expectations for the future of Crystal Fibre. Shortly after however, the telecommunication market collapsed and numerous companies disappeared from the scene. In the following months it became clear that it would take years for the telecommunication industry to recover, so NKT-Photonics decided to shift the focus away from telecommunication applications and development of new fiber lasers for industry, sensing and medicine became the main priority. The shift made sense since the existing knowledge about fiber lasers in Koheras could be combined with the unique fibers from Crystal Fibre to give a competitive edge.

As a NKT-Academy student with close contact to NKT-Research, the transition also had an impact on the focus areas of my PhD. My first year was dedicated to finding new applications of the PCFs and I focused on parametric amplification of super continua from PCFs and continuous wave four-wave mixing (chapters

3 and 4). With NKT-Research focussing on fiber lasers it was natural to shift to this field as well and I started working on fiber amplifiers and Q-switching of fiber lasers. These projects were made in direct collaboration with NKT-Research and their partner at the University of Valencia, Spain. The results are described in chapter 5.

In the following two years Crystal Fiber developed new types of PCFs. With the production of fiber lasers in mind, the original small core, highly nonlinear, fibers were now accompanied by a variety of doped Large Mode Area (LMA) fibers. The versatility of the PCF technology enabled scaling of the fiber dimensions without sacrificing mode quality. The increased mode size implied very low nonlinearity and thereby the capacity to guide high power levels.

Driven by the new fibers from Crystal Fibre and other fiber manufacturers, the development of high power fiber lasers has virtually exploded and today fiber lasers can almost match conventional solid state lasers in terms of output power. Q-switched fiber lasers and femtosecond fiber oscillators are also emerging in these years and rapidly approach the performance level of traditional systems. The USA-based company IMRA [4] and Frank Wise's group at Cornell University [5] have been major driving forces in the development of fiber oscillators. Today, more than ten nanojoule femtosecond pulses can be obtained from environmentally stable fiber oscillators [6].

The high-power development has mainly been pushed by the German company IPG [7] and Andreas Tünnermann's group in Jena [8]. IPG has demonstrated more than 1.5 kW of continuous wave from a fiber laser [7] and is now developing commercial fiber laser systems. The group in Jena has pushed the limits of average power and pulse energy from fiber lasers and has been a valuable cooperator for Crystal Fibre in the development process. The combination of cutting edge fiber technology and high power expertise has led to rapid progress. One of the latest results from Jena is a 100 W 220 fs laser [9].

I stayed in Jena during summer and fall of 2005 and worked on super continuum generation in collaboration with Thomas Schreiber, a NKT-Academy student and member of the Jena group. Specifically, we investigated super continuum generation in PCFs with femtosecond pulses in a two-pump configuration. The experiments were motivated by a newly developed nanosecond whitelight source from Koheras which was based on a similar dual-pump scheme. The femtosecond experiments were therefore made to obtain a deeper understanding of the fundamental processes of the dual-pumping scheme. The outcome of this work is described in chapter 7.

The last part of my stay in Jena was dedicated to a larger project combining the work with super continua and high power fiber lasers. Returning to the former idea of making parametric amplification of super continua from PCFs (chapter

3), a high power fiber laser pumped parametric amplifier was built. The experiment demonstrated a new way of making optical parametric amplification and introduced fiber lasers as pump sources for such setups. The potential and advantages of fiber laser pumped optical parametric amplifiers will be described in chapter 8.

Outline of the thesis

The thesis starts with a broad introduction to nonlinear optics and optical fibers with emphasis on PCFs and nonlinear fiber optics. The following chapters chronologically describe the main topics of this project.

Chapter 2 Nonlinear optics and optical fibers.

A brief introduction to nonlinear optics and a description of the fundamental properties of optical fibers. The nonlinear Schrödinger equation is derived and microstructured fibers are introduced.

Chapter 3 Intracavity frequency doubling of a Ti:Sapphire oscillator.

The first part of my PhD was focused on re-designing a femtosecond Ti:Sapphire laser cavity. The aim was to make intracavity frequency doubling in order to obtain a strong blue pump source which could pump a parametric amplifier. The synchronized seed for the amplifier was a supercontinuum generated in a PCF by the remaining fundamental power from the Ti:Sapphire oscillator. The chapter is based on publication I. (see publication list)

Chapter 4 Continuous wave four-wave-mixing in a photonic crystal fiber.

The unique dispersion of some PCFs allows nonlinear effects to take place at low power levels. Four-wave-mixing is usually only important in the spectral region close to the zero dispersion wavelength, but in PCFs it can take place over hundreds of nanometers. The chapter is based on publication II.

Chapter 5 Q-switched fiber laser.

This chapter describes the work with nanosecond Q-switched fiber lasers. Several approaches to obtain pulsed sources were attempted and this chapter will describe the work with an all-fiber Q-switched laser based on modulation of a fiber Bragg grating. The chapter is based on publication III.

Chapter 6 Fiber dispersion measurements with white-light interferometry.

One of the main advantages of PCFs is the ability to tailor the dispersion profile. Precise knowledge of the dispersion is crucial for understanding the nonlinear effects taking place in the fibers. White-light interferometry is a simple, reliable technique to measure dispersion and this chapter describes a fiber based setup

made on request from NKT-Research. Dispersion profiles from well-known fibers as well as novel designs are presented.

Chapter 7 Dual-wavelength pumping of photonic crystal fibers.

Co-propagating two femtosecond pulses in a PCF is shown to result in super continua displaying exceptional flatness in the blue and green part of the spectrum. The underlying mechanism is identified as cross-phase modulation. Deeper understanding of the process may help to improve existing white-light sources relying on the dual-pump technique. The chapter is based on publications IV and iii.

Chapter 8 Fiber laser pumped optical parametric amplifier.

The power scalability of fiber lasers make them ideal pump sources for high average power optical parametric amplifiers. Building on the idea from Chapter 3, a super continuum generated in a PCF is amplified in a nonlinear crystal pumped by the frequency doubled output from a fiber amplifier. The chapter is based on publication V and iv.

Chapter 9 Summary and acknowledgements.

Chapter 2

Nonlinear optics and optical fibers

A brief introduction to nonlinear optics and the fundamentals of fiber optics. The governing equations for pulse propagation in optical fibers are described and micro-structured fibers are introduced.

2.1 Nonlinear optics

The field of nonlinear optics is complex and encompasses myriads of interesting effects and practical applications. In spite of its richness, most of the effects can be described accurately with just a few equations. This introduction to nonlinear optics is therefore limited to a simple analysis of Maxwell's equations which govern the propagation of light.

In dielectric media and in absence of free charges or currents the equations are given by

$$\vec{\nabla} \cdot \mathbf{D}(\mathbf{r}, t) = 0 \quad (2.1)$$

$$\vec{\nabla} \cdot \mathbf{B}(\mathbf{r}, t) = 0 \quad (2.2)$$

$$\vec{\nabla} \times \mathbf{E}(\mathbf{r}, t) = -\frac{\partial \mathbf{B}(\mathbf{r}, t)}{\partial t} \quad (2.3)$$

$$\vec{\nabla} \times \mathbf{H}(\mathbf{r}, t) = \frac{\partial \mathbf{D}(\mathbf{r}, t)}{\partial t} \quad (2.4)$$

where \mathbf{D} is the electric displacement and \mathbf{B} , \mathbf{E} are the magnetic and electric fields respectively. \mathbf{H} and \mathbf{D} are related to the magnetic and electric fields according to

$$\mathbf{B}(\mathbf{r}, t) = \mu_0 \mathbf{H}(\mathbf{r}, t) \quad \mathbf{D}(\mathbf{r}, t) = \epsilon_0 \mathbf{E}(\mathbf{r}, t) + \mathbf{P}(\mathbf{r}, t) \quad (2.5)$$

where \mathbf{P} is the polarization and μ_0, ϵ_0 are the permeability and permittivity of free space respectively. Equations 2.1-2.5 can be decoupled and, by assuming $\vec{\nabla} \cdot \mathbf{E} = 0$, the following expression is obtained

$$-\nabla^2 \mathbf{E}(\mathbf{r}, t) + \frac{1}{c^2} \frac{\partial^2 \mathbf{E}(\mathbf{r}, t)}{\partial t^2} = -\mu_0 \frac{\partial^2 \mathbf{P}(\mathbf{r}, t)}{\partial t^2} \quad (2.6)$$

where c is the speed of light in vacuum. The polarization is given by

$$\mathbf{P}(\mathbf{r}, t) = \epsilon_0 \chi \mathbf{E}(\mathbf{r}, t) \quad (2.7)$$

where χ is the optical susceptibility. χ can be calculated by an iterative procedure employing first order perturbation methods [10] and the polarization is therefore conveniently expressed as a sum of a linear term and nonlinear terms

$$\mathbf{P} = \mathbf{P}_l + \mathbf{P}_{nl} = \epsilon_0 \chi^{(1)} \cdot \mathbf{E} + \epsilon_0 \sum_{j>2} \chi^{(j)} \mathbf{E}^{(j)} \quad (2.8)$$

Introducing the linear refractive index $n^2(\omega) = \epsilon(\omega) = 1 + \chi^{(1)}$, eq. 2.6 can be written as

$$-\nabla^2 \mathbf{E}(\mathbf{r}, t) + \frac{n(\omega)^2}{c^2} \frac{\partial^2 \mathbf{E}(\mathbf{r}, t)}{\partial t^2} = -\mu_0 \frac{\partial^2 \mathbf{P}_{nl}(\mathbf{r}, t)}{\partial t^2} \quad (2.9)$$

where $\epsilon(\omega)$ is the dielectric function. This expression shows that the nonlinear polarization acts as a source term for a driven wave equation. In absence of \mathbf{P}_{nl} the radiation simply propagates as a free wave with speed $v = c/n$.

Most nonlinear effects are well described with this equation and can be related to a given $\chi^{(j)}$ -tensor. For example, the real part of $\chi^{(2)}$ is responsible for second harmonic generation (SHG) and the real part of $\chi^{(3)}$ enables third harmonic generation, self-phase-modulation (SPM), self-focusing and four-wave-mixing. The imaginary part of $\chi^{(3)}$ is responsible for two-photon absorption, Raman-gain and more. Still higher order processes are weak and can usually be neglected. In optical fibers all even orders of χ vanish due to inversion symmetry in the amorphous SiO_2 [10] and the only significant nonlinear contribution is therefore from $\chi^{(3)}$. The nonlinear polarization is then reduced to

$$\mathbf{P}_{nl}(\mathbf{r}, t) = \epsilon_0 \int \int \int_{-\infty}^{\infty} \chi^{(3)}(t, t_1, t_2, t_3) \mathbf{E}(\mathbf{r}, t_1) \mathbf{E}(\mathbf{r}, t_2) \mathbf{E}(\mathbf{r}, t_3) dt_1 dt_2 dt_3 \quad (2.10)$$

where $\chi^{(3)}(t, t_1, t_2, t_3)$ is approximated by $\chi^{(3)}(t, t_1, t_2, t_3) = \chi^{(3)} R(t - t_1) \delta(t - t_2) \delta(t - t_3)$ [11]. The interaction between light and the vibrational modes of silica are included through the following functional form of $R(t)$

$$R(t) = (1 - f_R) \delta(t) + f_R h_R(t) \quad (2.11)$$

f_R is the fractional part of the response dominated by Raman scattering and h_R is the Raman response function which can be estimated through analysis of the Raman gain curve [11–13]. Figure 2.1 illustrates Raman scattering where energy is lost due to vibrational excitation of the material. In absence of Raman

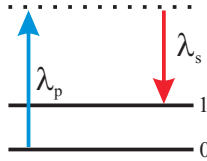


Figure 2.1: The excitation energy between the vibrational states $|0\rangle$ and $|1\rangle$ in silica is lost to the material in Raman scattering.

scattering, the nonlinear response is dominated by the fast motion of electrons and the polarization can be modelled by replacing $h_R(t)$ with a delta function [12].

In the following section, basic properties of optical fibers will be investigated. The equations governing the mode structure and pulse propagation will be developed and the electronic nonlinear response (Kerr nonlinearity) will be included to obtain the nonlinear Schrödinger equation.

2.2 Basic properties of optical fibers

Conventional optical fibers guide light by total internal reflection. A core with high index of refraction is surrounded by a cladding with lower index of refraction and the index-difference determines how tightly the light is confined in the core. Various index-profiles have been made in order to enhance the guiding properties [14], but the most commonly used type is the simple step index fiber. Figure 2.2 shows typical dimensions of such a fiber. A small silica core with a diameter of 5-12 μm with index n_1 is surrounded by a cladding layer of roughly 125 μm in diameter with index n_2 . An additional layer of a polymer is added to enhance the strength of the fiber and leaves the fiber with an outer diameter of 250 μm . The fiber's numerical aperture, $NA = \sqrt{n_{\text{core}} - n_{\text{clad}}}$ directly relates

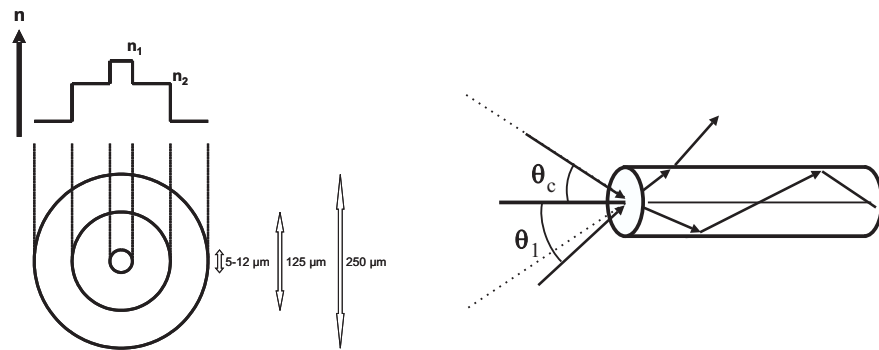


Figure 2.2: Left: Schematic view of a step-index fiber. The size of the core depends on the purpose of the fiber, but single-mode fibers in the near-infrared typically have core diameters of 5-12 μm . Right: At incident angles below the critical angle given by $\theta_c = \sin^{-1}(NA)$ the rays are captured by the fiber, while bigger angles allow the light to escape through the cladding.

the index-difference to the maximally allowed angle between the fiber axis and the wave-vectors of the incident light: $NA = \sin(\theta_c)$ (see right panel of figure 2.2). The choice of coupling optics therefore depends on the size of the fiber core as well as on the fibers ability to capture the light.

In single-mode fibers the typical index difference between core and cladding is of the order of 0.2-1% so NA-values are not exceeding 0.25 ($\theta_c < 15^\circ$). Hard focussing is therefore not possible and high brightness sources are generally needed to get significant coupling into a guided mode. Increasing the NA makes it easier to couple light into the fiber and also reduces bend losses since the condition for total internal reflection is relaxed. The price is however that the fiber may support several spatial modes, which greatly diminish the beam quality after the fiber. In most applications, it is desired, if not mandatory, to

have only one spatial mode.

To get a better understanding of the important quantities in fiber optics, it is beneficial to return to eq. 2.9. Neglecting the nonlinear terms, the equation is conveniently solved in Fourier-space by replacing the operator $\frac{\partial^2}{\partial t^2}$ with $-\omega^2$

$$\nabla^2 \mathbf{E}(\mathbf{r}, \omega) = \frac{\omega^2}{c^2} n^2(\omega) \mathbf{E}(\mathbf{r}, \omega) \quad (2.12)$$

A superposition of plane waves is a solution to this equation and since the light must also be confined in the transverse dimension of the fiber, a linearly polarized solution must be of the form

$$\mathbf{E}(\mathbf{r}, \omega - \omega_0) = \hat{x} F(x, y) \cdot A(z, \omega - \omega_0) \cdot e^{-i(\beta_0 z - \omega_0 t)} \quad (2.13)$$

where F is the transverse field distribution, A is a slowly varying envelope, ω_0 is a fast carrier frequency and β_0 is the wave-number corresponding to the central frequency. A is normalized such that $|A|^2$ represents the optical power. The product of the independent transverse and longitudinal parts leads to two conditional equations [12, 15]

$$\left(\frac{\partial^2}{\partial x^2} + \frac{\partial^2}{\partial y^2} \right) F(x, y) + n^2(\omega) \frac{\omega^2}{c^2} F(x, y) = \beta^2 F(x, y) \quad (2.14)$$

$$2i\beta_0 \frac{\partial}{\partial z} A(z, \omega) + 2\beta_0(\beta - \beta_0) A(z, \omega) = 0 \quad (2.15)$$

where the second derivative of the slowly varying envelope $A(z, \omega - \omega_0)$ has been neglected and the approximation $(\beta^2 - \beta_0^2) \sim 2\beta_0(\beta - \beta_0)$ has been used in deriving eq. 2.15. Both measures are justified as long as $\Delta\omega \ll \omega$. Equation 2.14 is known as the scalar Helmholtz equation and it leads to the conditions for the guided modes and their field distribution $F(x, y)$ in the fiber. Propagation along the fiber is governed by equation 2.15 which will finally result in a nonlinear Schrödinger equation.

The scalar Helmholtz equation (eq. 2.14) is an eigenvalue problem where β is an eigenvalue of the transverse field distribution $F(x, y)$. In absence of nonlinear polarization, the solutions for $F(x, y)$ are superpositions of Bessel and Neumann functions and it can be shown that there are only confined modes when $k^2 n_1^2 > \beta^2 > k^2 n_2^2$ [16]. There may be several values of β fulfilling this condition in which case the fiber is multi-mode - meaning that more than one spatial field distribution is possible in the fiber. Figure 2.3 illustrates the intensity distribution for the fundamental mode and two higher order modes. The uniform fundamental spatial mode is preferred for most practical applications because of its high brightness.

The so-called normalized frequency V is introduced to quantify when single-mode operation can be obtained and it can be shown that the following condi-

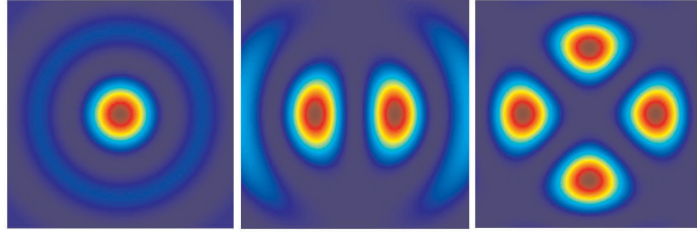


Figure 2.3: Simulated transverse intensity distributions for the fundamental mode LP_{01} and the two higher order modes LP_{11} and LP_{21} . Nomenclature and further reading can be found in [14].

tions must be fulfilled [16]

$$V = k_0 a (n_{core}^2 - n_{clad}^2)^{1/2} = \frac{2\pi}{\lambda} a \cdot NA < 2.405 \quad (2.16)$$

where λ is the wavelength in vacuum and a is the fiber core radius. V is an important design parameter and eq. 2.16 indicates the trade-offs faced when designing optical fibers. In order to ensure single-mode operation of the fiber, the core size and the NA of the fiber must be balanced to keep V below 2.405. Increasing the core size thus requires a corresponding decrease in NA and vice versa.

2.2.1 The nonlinear Schrödinger equation

When the Kerr-nonlinearity is included in eq. 2.9, the effective refractive index $\tilde{n}(\omega)$ is modified by the weak nonlinear term $\epsilon_{nl} = \frac{3}{4}\chi^{(3)}|E|^2$

$$\tilde{n}^2 = \epsilon = 1 + \chi^{(1)} + \frac{3}{4}\chi^{(3)}|E|^2 \quad (2.17)$$

The change in \tilde{n} is small so

$$\tilde{n}^2 = (n + \Delta n)^2 \sim n^2 + 2n\Delta n \quad (2.18)$$

which allows us to solve eq. 2.14 with first order perturbation methods: First n^2 is used to find the field distribution $F(x,y)$ and the propagation parameter β . The 'eigenfunctions' $F(x,y)$ are then used to calculate the first order correction to β due to the term $2n\Delta n$

$$\tilde{\beta}(\omega) = \beta(\omega) + \Delta\beta \quad (2.19)$$

The unperturbed linear propagation constant is approximated by a Taylor-expansion around the carrier frequency, ω_0

$$\beta(\omega) = \beta_0 + \beta_1(\omega - \omega_0) + \frac{1}{2}\beta_2(\omega - \omega_0)^2 + \frac{1}{6}\beta_3(\omega - \omega_0)^3 + \dots \quad (2.20)$$

where $\beta_i = \frac{\partial^i \beta}{\partial \omega^i} |_{\omega_0}$.

This expression is inserted in eq. 2.15 and a Fourier transformation back to the time domain gives the following equation for the time-dependent slowly varying envelope

$$\frac{\partial A}{\partial z} + \sum_{n=1} \beta_n \frac{i^{n-1}}{n!} \frac{\partial^n}{\partial t^n} A = i\Delta\beta A \quad (2.21)$$

For a given field distribution, $\Delta\beta$ is given by:

$$\Delta\beta = \frac{\omega_0 \int \int_{-\infty}^{\infty} \Delta n |F(x, y)|^2 dx dy}{c \int \int_{-\infty}^{\infty} |F(x, y)|^2 dx dy} \quad (2.22)$$

with

$$\Delta n = \frac{3}{8n} \text{Re}[\chi^{(3)}] |E|^2 + i \left(\frac{1}{2n} \text{Im}[\chi^{(1)}] + \frac{3}{8n} \text{Im}[\chi^{(3)}] |E|^2 \right) \quad (2.23)$$

Neglecting the imaginary parts of $\chi^{(j)}$ (absorption) eq. 2.22 simplifies considerably:

$$\Delta\beta = \frac{n_2 \omega_0}{c A_{eff}} |A|^2 = \gamma |A|^2 \quad (2.24)$$

where n_2 is the nonlinear refractive index which in silica is $\sim 3 \cdot 10^{-20} (W \cdot m)^{-1}$ and A_{eff} is the effective mode area. The final result thus becomes

$$\frac{\partial A}{\partial z} + \sum_{n=1} \beta_n \frac{i^{n-1}}{n!} \frac{\partial^n}{\partial t^n} A = i\gamma |A|^2 A \quad (2.25)$$

where γ is termed the nonlinear parameter. Equation 2.25 describes the basic effects during propagation of an optical pulse in single-mode fibers and is referred to as the nonlinear Schrödinger equation.

2.2.2 Dispersion

When electromagnetic radiation is incident on a material, the constituting atoms are polarized and the resulting macroscopic polarization radiates at the same frequency as the incoming light, but with a frequency dependent delay [17]. Different frequencies therefore propagate with different speeds in the material

which causes a spreading, or dispersion, in time. There are several causes of temporal dispersion in optical systems. Presence of atomic resonances cause continuous absorption and emission of matched frequencies which are thereby delayed. Multi-mode beams may be dispersed in time if the various modes experience different indexes of refraction due to their spatial extension. This is important in multi-mode optical fibers where higher order modes extend far into the cladding of the fiber and thereby see a lower index of refraction (see figure 2.3). Finally there is waveguide dispersion which is only important in single mode fibers. It arises because the mode is not completely confined to the core of the fiber. Depending on the size of the core and the index difference between core and cladding, a part of the mode will leak into the cladding and thus experience a lower index. Waveguide dispersion can be tailored by varying the mentioned parameters and it is possible to shift the zero dispersion wavelength (ZDW) of the fiber considerably. This has been done successfully with telecommunication fibers where it is advantageous to have zero dispersion in the low-loss window around 1550 nm [18] and with PCFs where ZDWs can be realized deep into the visible [19].

All types of dispersion, are included in the expansion of $\beta(\omega)$ in eq. 2.20. The first terms are related to the group velocity (β_1), group velocity dispersion (β_2), third order dispersion (β_3) and so forth. It is useful to change to a coordinate system moving with the group velocity (retarded frame) with the following transformation $T = t - z/v_{group} = t - \beta_1 z$. Equation 2.21 is then reduced to

$$\frac{\partial A}{\partial z} + \sum_{n=2} \beta_n \frac{i^{n-1}}{n!} \frac{\partial^n}{\partial T^n} A = i\gamma |A|^2 A \quad (2.26)$$

The effect of group velocity dispersion (GVD) can be illustrated by neglecting higher order dispersion terms and nonlinearities ($\gamma = 0$). Fourier transforming eq. 2.26 then yields

$$\frac{\partial A(z, \omega)}{\partial z} - \frac{i}{2} \beta_2 \omega^2 A(z, \omega) = 0 \quad (2.27)$$

which is solved by

$$A(z, \omega) = A(0, \omega) \exp\left(\frac{i}{2} \beta_2 \omega^2 z\right) \quad (2.28)$$

The solution shows that the pulse spectrum is not changed by GVD, but a frequency dependent phase is introduced. Transforming back to the time-domain results in the following expression for the time dependent pulse envelope

$$A(z, T) = \frac{1}{2\pi} \int_{-\infty}^{\infty} A(0, \omega) \exp\left(\frac{i}{2} \beta_2 \omega^2 z - i\omega T\right) d\omega \quad (2.29)$$

For a gaussian input pulse $A(0, T) = \exp(-\Gamma_0 T^2) \cdot \exp(i\omega_0 T)$ the integral is

easily solved to give

$$A(z, T) = \exp\left(i\left[\phi_0 + \omega_0 T + \frac{2\Gamma_0^2 \beta_2 z T^2}{1 + (2\Gamma_0 \beta_2 z)^2}\right]\right) \cdot \exp\left(-\frac{\Gamma_0 T^2}{1 + (2\Gamma_0 \beta_2 z)^2}\right) \quad (2.30)$$

which reveals that the pulse acquires a time dependent phase and is temporally broadened. The phase is quadratic in time which means that the instantaneous carrier frequency $\omega(T) = \frac{\partial \phi}{\partial T}$ is linearly chirped. The sign of β_2 determines whether the pulse is up-chirped (red faster than blue) or down-chirped. Figure 2.4 shows a simulated 150 fs gaussian pulse after propagation through 1.3 meter of a normally dispersive 5 μm single-mode fiber when nonlinearity and higher order dispersion are neglected. The initially unchirped pulse picks up a linear chirp over the entire pulse with the leading edge of the pulse being redshifted and the trailing edge blueshifted.

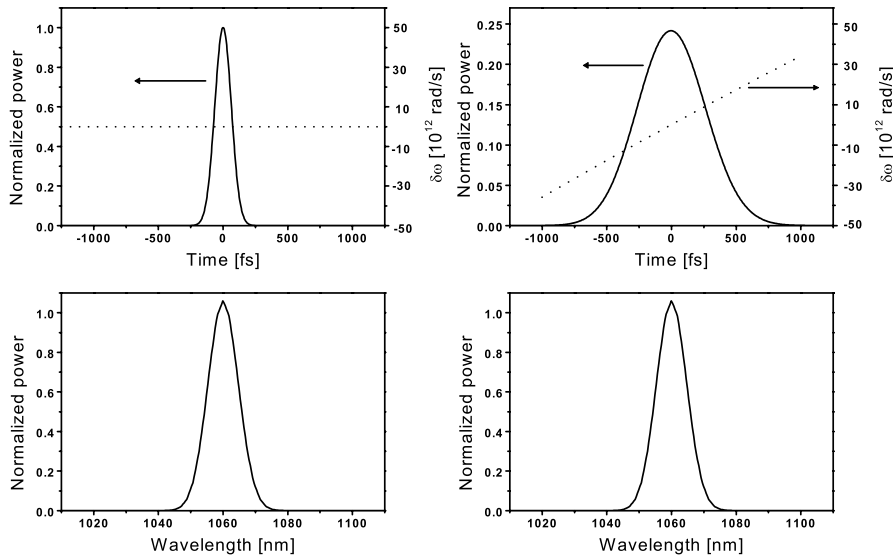


Figure 2.4: Upper row: Temporal profile of a 0.67 nJ 150 fs gaussian pulse before (left) and after (right) propagation through 1.3 m of a 5 μm single-mode fiber when higher order dispersion and nonlinearity are neglected. The dotted lines show the change in instantaneous carrier frequency across the pulse envelope. The linear chirp due to the group velocity dispersion is evident in the right panel. The sign of β_2 determines whether the red (normal dispersion) or the blue (anomalous) spectral components are faster. The bottom row shows the unchanged spectrum of the pulse.

Higher order dispersion terms can usually be neglected but in case of ultra-short pulses or wavelengths close to the zero dispersion wavelength (ZDW) of

the fiber, third and even fourth order dispersion may have to be included in eq. 2.26. Like β_2 , the higher order terms do not change the spectrum of the pulse but significantly alter the temporal shape [12].

From a practical point of view, second order dispersion is not a problem since a linear chirp is conveniently removed by simple prism or grating sequences [20]. In contrast, higher order dispersion is not easily compensated and therefore leads to decreased pulse quality.

2.2.3 Self phase modulation

The effect of the nonlinear term in eq. 2.26 is best illustrated by neglecting dispersion. The equation then reduces to

$$\frac{\partial A}{\partial z} = i\gamma|A|^2 A \quad (2.31)$$

which is solved by

$$A(z, T) = A(0, T) \exp(i\gamma|A(z, T)|^2 z) \quad (2.32)$$

Equation 2.32 shows that the nonlinearity does not change the pulse shape but merely imposes a nonlinear phase which depends on the temporal profile of the pulse itself - hence the effect is named self phase modulation (SPM).

Figure 2.5 shows a simulated 0.67 nJ 150 fs gaussian pulse after propagation through 30 cm of a 5 μm single-mode fiber when dispersion is neglected. The chirp is seen to be linear at the center and nonlinear at the wings of the pulse. The central chirp is similar to the chirp caused by positive GVD (see figure 2.4) with red frequency components being shifted to the leading edge of the pulse and blue components to the trailing edge.

The joint action of positive GVD and SPM is therefore to rapidly chirp and broaden the pulse. However, negative GVD can in some cases balance the linear part of the SPM chirp and the pulse can propagate without changing its form in time and frequency. This type of solution is called a fundamental soliton [12]. Physically, the negative GVD shifts the blue spectral components to the leading edge of the pulse where they get redshifted back again by SPM. Fundamental solitons can propagate through thousands of kilometers of fiber without degrading and have been used successfully for data transmission in telecommunication lines [21].

If the dispersion is not exactly balanced by SPM, the pulse will "breathe" in the sense that it broadens and contracts periodically in time and frequency as it propagates along the fiber. This type of solution is called a higher order soliton and fission of such solitons is fundamental for the understanding of super continuum generation in optical fibers.

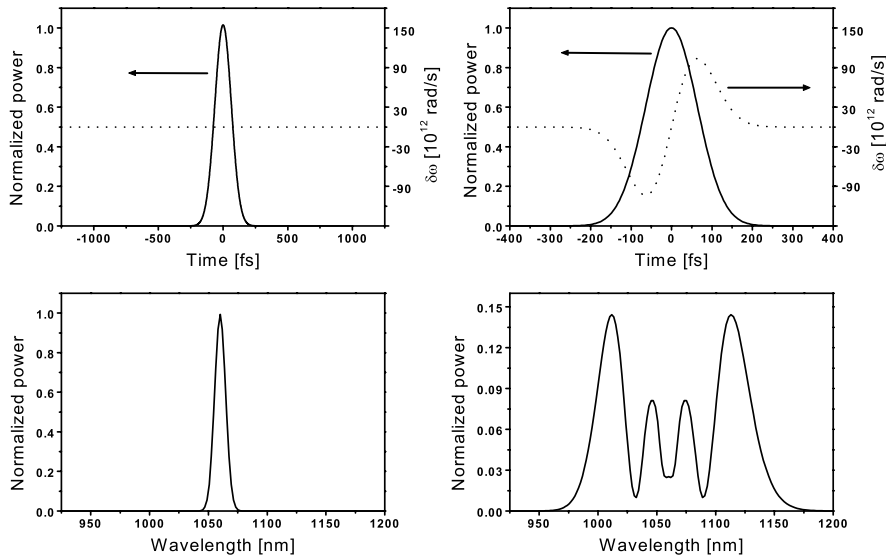


Figure 2.5: The upper row show the temporal profile of a 0.67 nJ 150 fs gaussian pulse before (left) and after (right) propagation through 0.3 m 5 μm single-mode fiber when dispersion is neglected. The central part of the pulse gets linearly chirped while the wings of the pulse pick up higher order phase. The bottom row shows the spectral evolution and the creation of new frequencies is clearly seen.

Full modelling of propagation of ultrashort pulses in optical fibers requires inclusion of higher order nonlinear effects. Especially Raman scattering proves to be important, but also cross-phase modulation, self-steepening and four wave mixing have to be included. The derivation of the extended nonlinear Schrödinger equation follows the derivation presented in section 2.2.1 but all elements of $\chi^{(3)}$ must be included. As the mathematics get extensive the result will merely be introduced without proof when super continuum generation in PCFs is discussed in section 2.5.

2.3 Rare Earth doped fibers

Rare Earth (RE) doped glass has been investigated and used as a laser media for more than four decades. Since the eighties, RE doped fibers have been available and fiber lasers and amplifiers have been an active field of research ever since. When RE elements are dissolved in a glass host, they become triply ionized by removal of the two outer 6s electrons and an inner 4f electron [22]. The optical properties of the dopants are then determined by the partially filled 4f orbital

and since the outer 5p and 5s electrons effectively shield the 4f electrons from the field of the host material, the laser characteristics, such as wavelength and gain bandwidth, are almost independent of the host. Today, optical fibers can be doped with a variety of REs with Erbium, Ytterbium (Yb), Neodymium and Thulium being the most used. In this thesis, only Yb-doped fibers have been employed.

The optical transitions in Yb take place between the $F_{5/2}$ and the $F_{7/2}$ levels. The field of the silica host causes Stark splitting as illustrated in figure 2.6 (left) and homogeneous broadening turns the discrete levels into energy bands [22]. It is noteworthy that these two bands are energetically isolated, so out-of-band transitions (ex. excited state absorption) are not possible. The energy gap

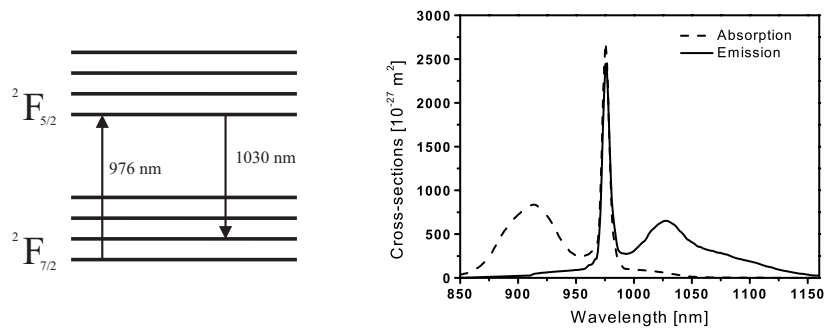


Figure 2.6: Left: Energy levels for the optical transition of 4f electrons in Yb^{3+} . Right: Cross-section for absorption and emission in Yb-doped silica [23].

between the two 'ground states' of the bands correspond to a wavelength of 976 nm and the system can therefore be pumped with commercially available telecom pump diodes. The most probable event for an electron excited to the ground state of $F_{5/2}$, is to return to the first Stark level of the lower band. This transition releases a photon with an energy corresponding to $\lambda = 1030$ nm. In the same manner, excited atoms can relax into higher Stark levels in $F_{7/2}$ and wavelengths from 976 nm to almost 1200 nm can be realized. The transitions have different probabilities as illustrated in figure 2.6 (right) which shows the cross-section of emission and absorption as a function of wavelength.

The upper state life time is approximately $900 \mu\text{s}$ so spontaneous emission takes place on this timescale. Because of the tight confinement of light in optical fibers, the spontaneously emitted photons have high probability of exciting a guided mode and can therefore be amplified along the fiber. Amplified spontaneous emission (ASE) is a main limitation of the extractable energy from standard single mode Yb-doped fiber lasers.

2.4 Photonic crystal fibers

In the beginning of the 1990's, the field of fiber optics was dominated by telecommunication applications. The physics behind light propagation in fibers was fully understood and, apart from being media for data transmission, fibers were also used as nonlinear frequency converters, sensors and even lasers. The invention of Erbium-doped fiber amplifiers really pushed the development of fiber based communication lines and an impressive development of fiber based optical components took place. On a more fundamental physical level, there was however not much development. This changed dramatically in 1996 when Russell suggested and demonstrated a revolutionary new type of optical fiber [24]. Instead of guiding light by total internal reflection, these fibers relied on a bandgap effect similar to what is known from semiconductors. Russell suggested to make defects in the silica matrix to prevent light at a given wavelength from propagating in the transverse direction and thereby confine it to the core of the fiber [19]. The mathematical description of the photonic bandgap is not straightfor-

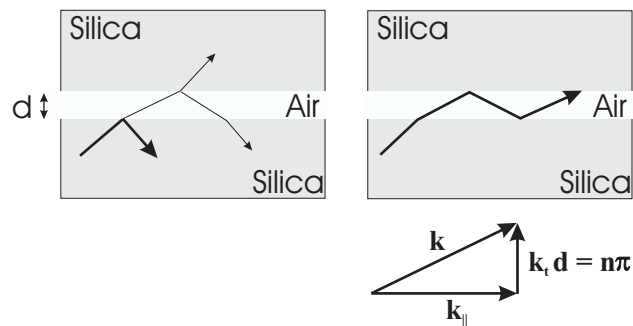


Figure 2.7: Light encountering an air defect in the silica matrix will be reflected or transmitted depending on the incident angle. If the product of the transverse wavevector and the thickness of the defect is an odd integer of π , the light can be resonantly guided in the defect.

ward [25] so a more intuitive picture can be beneficial. Figure 2.7 shows rays propagating in a silica slab with an air defect of thickness d . Depending on the incident angle, the light will be transmitted or reflected at the silica/air interfaces. However, if the transverse wavelength matches the dimension of the defect a resonance occurs and light can be guided in the defect. At a given incidence angle, a range of wavelengths will be guided in the defect and thus escape the silica slab. But if the size of the defect is reduced to the order of a wavelength, resonances are no longer possible and all wavelengths will remain in the silica. It is therefore possible to confine light by surrounding it by such defects. This is the basic idea of photonic bandgap fibers (PBGs). Figure 2.8 shows a cross

section of a PBG fiber made by Blaze Photonics. An air-core is surrounded by an array of air holes which run along the length of the fiber. Transverse propagation is prohibited because of the non-resonant nature of both the air holes and the thin silica bridges which support the structure. Such fibers can

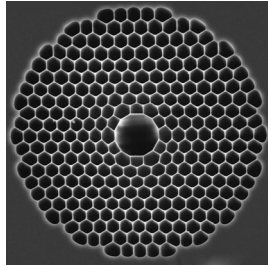


Figure 2.8: SEM image of an air-guiding photonic bandgap fiber. The light is confined to the central core by surrounding it with anti-resonant structures. The diameter of the core is roughly $9 \mu\text{m}$. Picture provided by Crystal Fibre.

be designed to be single-mode in a certain wavelength interval by making sure that higher order modes have resonances in the defects and thus are radiated away in the air cladding.

The production of PBG fibers is nontrivial and although Russel's initial idea was based on air-guiding of this type, the first realization of a bandgap fiber was actually with a solid core [19]. This class of fibers is named photonic crystal fibers (PCFs) and although the guiding mechanism is in principle the same as in the PBG fibers, the simpler picture of total internal reflection is usually adopted to describe these fibers. As for conventional fibers, the index difference between the core and the cladding determines the guiding properties and again it is possible to define a V-parameter which relates the NA of the fiber to the number of supported modes. The main difference between PCFs and standard fibers is the strong wavelength dependence of the effective index of the PCF cladding due to presence of the air defects. In standard fibers the index-difference between core and cladding is almost independent of wavelength and for a given core size and NA, the fiber is only single-mode above a certain wavelength (eq. 2.16). Only by decreasing the core size or the NA, the fibers can be kept single-mode at lower wavelengths, but the price is decreasing coupling to the guided mode. In PCFs the wavelength-dependent cladding index arises because shorter wavelengths are more confined to the silica core whereas longer wavelengths extend more into the cladding and thus see a lower index. The wavelength dependent NA makes it possible to keep the V-parameter below the single-mode cut-off for all wavelengths and it has been shown that an air-filling fraction of $d/\Lambda > 0.4$ leads to this 'endlessly single mode' situation [26, 27]. An additional advantage of the potentially high index-difference (air to silica)

between core and cladding is the possibility of making NA values as high as 0.6 which enables efficient coupling to even very small cores.

Figure 2.9 shows a schematic drawing of a PCF where the core is actually a defect in a regular array of air holes of diameter d . The distance, Λ , between air holes is called the pitch. The right side of the figure shows a real image of a PCF produced by Crystal Fibre.

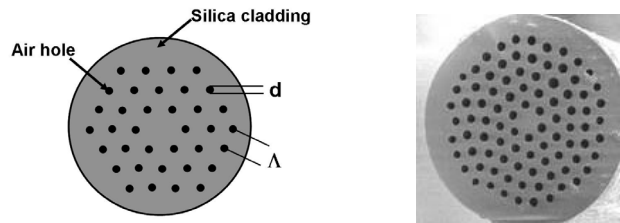


Figure 2.9: Left: Schematic drawing of a PCF. A solid core represents a defect in a regular array of air holes. The size of the air holes and the distance between them (pitch) are crucial for guiding and dispersion properties and must be kept constant throughout the fiber. Right: Realization of a PCF. In this case the defect is made up of several missing air holes in the center of the fiber, leading to a large mode area fiber

The dispersion of these fibers can also be tailored to a great extent. Tuning of the parameters d and Λ can add significant waveguide dispersion and shift the zero dispersion wavelength far into the visible. Herrmanns demonstration of super continuum generation in a PCF relied on shifting the ZDW to 800 nm where Ti:Sapphire oscillators can deliver sub-100 fs pulses. In absence of dispersion, the ultrashort pulses stay short and the fiber therefore exhibits a huge nonlinear response.

It was later demonstrated that the core size of the PCFs can be scaled to much larger dimensions. Like in conventional fibers, a decrease in NA allows an increase of the core dimensions while maintaining single-mode operation. Crystal Fibre has recently realized a huge $60 \mu\text{m}$ diameter core intrinsically single mode fiber, which is designed for high power application where nonlinearities must be minimized [28]. Figure 2.10 shows the double clad structure with a solid core surrounded by two microstructured areas. The inner rings of air holes confine light in the low NA single mode core while the outer ring of large air holes constitutes the pump cladding and causes a huge NA of 0.6 for the pump light. The high NA enables the use of cheap low-brightness diodes to pump the fiber and the modal overlap between the core and the $180 \mu\text{m}$ multi-mode pump core ensures efficient pump absorption in the strongly Yb-doped core. The combination of heavy doping and large core area enable high energy storage in the fiber leading to extremely efficient lasing and amplification.

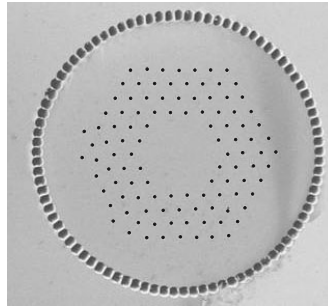


Figure 2.10: Large mode area, double clad photonic crystal fiber. The core is made by removing 19 air holes and is heavily Ytterbium-doped with an absorption of roughly 25 dB/m. As a consequence very efficient lasing can be realized with short ~ 0.5 meter fibers which in combination with the large core area, minimize nonlinear effects.

2.5 Super continuum generation in PCFs

Supercontinuum generation (SCG) in optical fibers has been extensively investigated in the last decade due to the improvements in production of microstructured fibers. The super continua have been an important part of the work in this thesis and a brief description of the theory is therefore given.

SCG in PCFs is a rather amazing effect to observe. Spectra spanning more than 1000 nm can be generated with sub-nJ pulses directly from oscillators. Figure 2.11 illustrates the process when 50 fs pulses from a Ti:Sapphire oscillator are coupled into a 20 cm long $1.7 \mu\text{m}$ core PCF. The input power is increased from left to right and the spectrum broadens accordingly as apparent from the right panel where white light is seen from the core of the fiber. The shown far-field clearly reveals the hexagonal structure of the fiber.

Before the demonstration of PCFs, super continua of similar bandwidth were usually obtained by focusing μJ pulses in Sapphire glass. Such continua often degrade due to accumulated material damage and can be highly unstable [29]. Super continua generated in PCFs are more attractive for many purposes since they are stable and come in a perfect spatial mode due to the single-mode nature of the fibers. As a consequence new PCF-based white-light sources have already emerged and found use in optical frequency metrology [30] and tomography [31].

The physical background of supercontinuum generation in PCFs with femtosecond pulses has been described theoretically [2] and experimental verifications of the model have been reported many times [3, 32–35]. It describes SCG as a process where a higher-order soliton is formed by a short pump pulse in the anomalous dispersion region of a fiber. This higher-order soliton breaks up into red-shifting fundamental solitons due to perturbations such as third or-

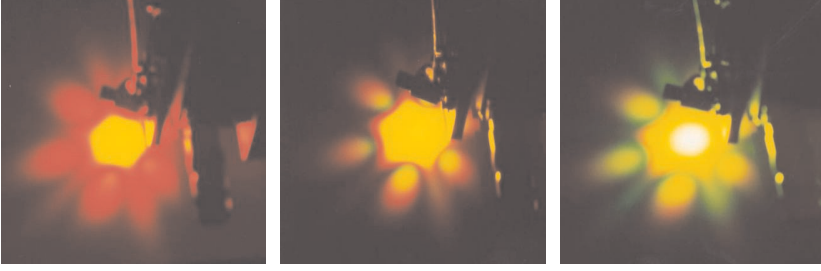


Figure 2.11: Super continuum generation in a 1.7 μm core PCF pumped with 50 fs pulses from a Ti:Sapphire oscillator. At a pulse energy of approximately 1 nJ a broad super continuum is generated as evident from the white core in the right picture.

der dispersion, stimulated Raman scattering and self-steepening. The spectral overlap between the breathing soliton and phasematched linear waves results in emission of non-solitonic radiation (NSR) in the normal dispersion region - often deep into the visible. If the dispersion profile of the fiber is known, the phasematching condition can be evaluated and the wavelength of the NSR can be calculated. In general, the NSR is shifted towards the blue when the pump wavelength is moved away from the ZDW.

The propagation of ultrashort pulses is accurately described by the extended nonlinear Schrödinger equation. It includes the linear effect of loss/gain α , dispersion β_n , SPM, self-steepening and the fractional contribution of the delayed Raman response function with the parameters f_R and $h_R(t)$ [12]. With the same notation as in section 2.2.1, the slowly varying pulse envelope $A(z,T)$ is determined by

$$\frac{\partial A}{\partial z} + \frac{\alpha}{2}A + \sum_{n=2} \beta_n \frac{i^{n-1}}{n!} \frac{\partial^n}{\partial T^n} A = i\gamma \left[(1 - f_R) \left(|A|^2 A - \frac{i}{\omega_0} \frac{\partial}{\partial T} (|A|^2 A) \right) + \dots \right. \\ \left. f_R \left(1 + \frac{i}{\omega_0} \frac{\partial}{\partial T} \right) \left(A(z,T) \int_0^\infty h_R(\tau) |A(z, T - \tau)|^2 d\tau \right) \right] \quad (2.33)$$

Equation 2.33 is capable of reproducing the SCG process described above to a great extent, even when an octave spanning spectrum is created.

A soliton is characterized by its soliton number, N

$$N^2 = \frac{\gamma P_0 T_0^2}{|\beta_2|} \quad (2.34)$$

where P_0, T_0 are the input peak power and pulse duration. A higher-order soliton ($N > 1.5$) breathes and reshapes its original form periodically - but even small perturbations cause it to break up into its constituent fundamental

solitons. Each of these obtain peak powers and pulse durations according to [36]

$$P_k = \frac{(2N - 2k + 1)^2}{N^2} P_p, \quad T_k = \frac{T_0}{2N - 2k + 1} \quad (2.35)$$

Upon fission, the fundamental solitons experience the soliton self-frequency shift (SSFS) due to the overlap of its spectrum with the Raman gain spectrum. The soliton emitted first ($k=1$) has the highest peak power and is therefore shifted faster towards the infrared spectral region. Four wave mixing (FWM) and cross-phase modulation (XPM) fill the gap between the infrared pump and the visible NSR when temporal overlap and phasematching between the various components are present. FWM and XPM will be described in greater detail in chapters 4 and 7.

Chapter 3

Intracavity frequency doubling of a femtosecond Ti:Sapphire oscillator

A Ti:Sapphire femtosecond cavity is extended and intracavity frequency doubled. The purpose is to obtain a powerful 400 nm source to pump an optical parametric amplifier. The remaining fundamental power from the oscillator is used to generate a super continuum in a PCF which serves as a synchronized seed signal for the parametric amplifier.

3.1 Introduction

The main focus of this work has been to rebuild a Ti:Sapphire femtosecond oscillator to enable intra cavity frequency doubling while still having enough fundamental power to generate a super continuum in a PCF. The second harmonic (SH) beam is used to pump an optical parametric amplifier (OPA) seeded with the synchronized output from the PCF. The large nonlinear response of PCFs enables generation of visible seed pulses - even with infrared pJ pump pulses [37] and tunability across the gain bandwidth of the OPA can be obtained by means of crystal angle tuning and by varying the power coupled to the PCF.

3.2 Intracavity second harmonic generation

Generation of sub-100 femtosecond pulses in the blue spectral region can conveniently be done by frequency doubling of Ti:sapphire lasers. By using a low repetition rate amplified laser system, high peak powers and thereby high conversion efficiency can be obtained. If higher repetition rates are needed, the output directly from the oscillator can be frequency doubled, but the relatively low peak power implies a reduced conversion [10]. A good compromise between the two techniques can be made by placing the doubling crystal inside the cavity of the oscillator where the peak power is typically 10-100 times larger than extracavity. Intracavity frequency doubling (IFD) of Ti:sapphire femtosecond oscillators was first demonstrated by Petrov [38] in 1991 and has later been pursued by several authors [39–41]. Depending on the application, an IFD-system can be constructed aiming at the shortest possible pulses or with the highest possible power in mind. In 1992 Ellingson *et al* [40] reported 1.6 nJ, 89 fs pulses at 430 nm and Kang has obtained 1.5 nJ at 422 nm with a pulse duration of 29 fs [39].

In the work presented here, the intention has been to maximize average power which resulted in 73 fs, 4 nJ pulses at 405 nm. The more than two-fold increase in pulse energy compared to previous reports is a result of using a thicker nonlinear crystal and the extended cavity length which reduces the repetition rate to 50 MHz.

3.2.1 Setup

The setup for IFD is shown in Figure 3.1. A commercially available Ti:sapphire femtosecond oscillator ("Mira Seed" from Coherent Inc.) is redesigned by introducing a mirror M3 about 10 cm from the slit and the output coupler. The mirror is put on a translational stage in order to facilitate the return to normal operation of the laser and the stage is secured in the cavity floor. Once inserted,

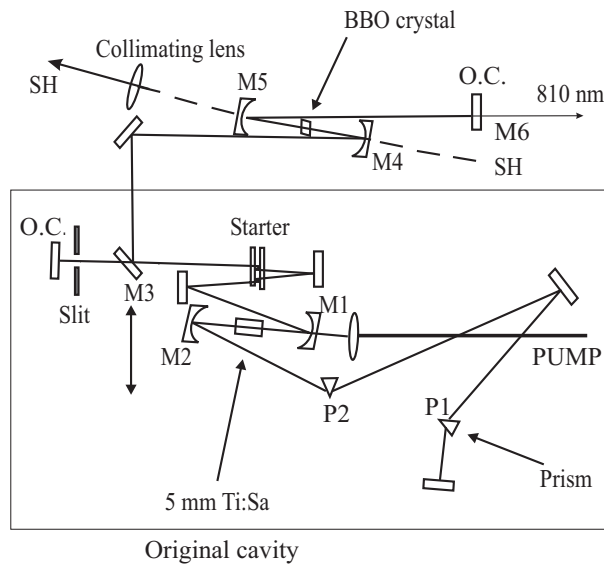


Figure 3.1: Schematic view of the setup. O.C., output couplers. P1,P2 fused silica prisms. Starter is a mirror which can vibrate. M3 is put on translational stage.

the mirror reflects the light out of the existing laser box and into a new arm consisting of 4 mirrors positioned on the laser table. Two spherical mirrors, (M4 and M5) with a radius of curvature of 5 cm, create a second focus in which a 0.5 mm thick AR coated β -BBO crystal cut at 29° is placed. The crystal is mounted in a system of three rotational stages and a translational stage makes it possible to vary the crystal position between M4 and M5. The spherical mirrors are high reflectors at 810 nm and transmit approximately 90% at 405 nm. M5 is placed on a translational stage so the separation between the two mirrors can be varied with high accuracy.

The modelocking mechanism in the cavity is the Kerr-nonlinearity which causes a lensing effect in the Ti:Sapphire crystal. As a result, high intensity fluctuations have different beam parameters (width, divergence) than a continuous wave (CW) beam. The former can be favored by placing a narrow slit at the point in the cavity where the high intensity beam is smaller than the CW beam. The slit then causes losses for the CW but not for the fluctuation, which is then allowed to grow further in intensity. Initialization of pulsed operation can therefore be made by inducing an intensity fluctuation simply by tapping a cavity mirror or otherwise perturbing the cavity [42].

The right position for the slit is estimated by simple ABCD-matrix calculations [43] and when the slit is put in the predicted position, the laser actually modelocks. However, when the BBO crystal is inserted in the secondary focus, modelocking is not possible. The high cavity losses associated with increased SHG because of pulsed operation make a CW solution more favorable and stable modelocking can not be sustained. Trial and error have however revealed that a slight reduction of the separation, d , between the two spherical mirrors M4, M5 leads to very stable modelocking. In fact, modelocking seems to be facilitated by the presence of the nonlinear crystal and, at certain values of d , the laser even modelocks without any slit. This effect originates from an improved spatial overlap of the pump and signal mode in the Ti:Sapphire crystal. With the extended cavity set for modelocking, the CW mode is larger than usual when it impinges on the spherical mirrors M1 and M2 surrounding the Ti:Sapphire crystal. In contrast, the modelocked beam resembles the beam produced by the original setup and is thereby more similar to the pump mode. Thus, the CW mode is not weakened by a slit but by a poor overlap with the pump.

With the right settings, the system is highly functional and easy to operate. It locks simply by vibrating a cavity mirror ("starter" in Figure 3.1) and it operates for as long as we have tested (10 hours+) with good power stability. An Ar-ion laser is used to pump the Ti:Sapphire crystal and any drift in the output power is closely related to instability of the pump. Figure 3.2 (left) shows

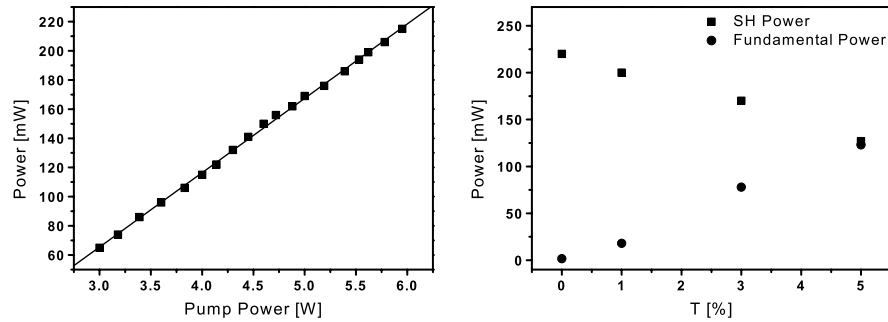


Figure 3.2: Left: Second Harmonic power as function of pump power for a fundamental output coupling of 1% . Right: Output powers for the SH (squares) and fundamental beam (dots) as function of 810 nm output coupling through mirror M6.

SH power as function of pump power when 1% of the fundamental is coupled out of the cavity. No saturation is found which implies that higher outputs can be achieved.

Experiments have shown that 12-15 mW at 810 nm are needed to signifi-

cantly broaden the spectrum in the nonlinear fiber. A certain output coupling of fundamental intensity must therefore be included when designing the cavity for SHG. Figure 3.2 (right) shows SH power and fundamental power as a functions of the transmission of the cavity end-mirror, M6 at a constant pump rate of 5.7 W. Maximum SH output of 220 mW at 405 nm through M4 is achieved when the output coupler M6 is replaced by a high reflector. This gives a conversion efficiency of 3.9% and corresponds to pulse energies of 4.4 nJ. A sufficient amount of fundamental light for pumping the PCF is achieved when the transmission of the output coupler is 1%. In that case 22 mW at 810 nm is obtained simultaneously with 200 mW at 405 nm.

3.2.2 Cavity dispersion

Optimal SH power is very dependent on the net cavity group velocity dispersion (GVD) and the cavity prisms are therefore essential for achieving maximum output. By adjusting the position of prism P1 in figure 3.1, the SH output can be tuned from 70 mW to 210 mW without losing modelocking. The travelling pulse is responding to local GVD, which makes the pulse-duration vary within the cavity [41, 44]. By minimizing the pulse duration at the position of the BBO crystal, maximum SH output is obtained. As the short pulse travels through the crystal it is chirped so its second pass through the crystal will produce less SH. Optimizing the system, 220 mW can be obtained in one arm while 110 mW is measured in the other. In general, maximum power is achieved when prism glass is retracted from the cavity to give negative net GVD. By doing so, bandwidth is reduced which means that there is a tradeoff between power and minimum pulse duration. In presence of negative GVD, the laser operates in soliton mode and a higher order soliton is circulating in the cavity. Close to zero GVD, third order dispersion (TOD) effects become significant and a perturbation of the soliton takes place, resulting in emission of non-solitonic radiation [45–47]. Figure 3.3 shows how the fundamental and SH spectra change as net GVD in the cavity is increased. The appearance of the non-solitonic peak at 780 nm in the fundamental spectrum is a clear indication of a perturbed soliton and near-zero cavity GVD. The spectrum of the SH does not change much during this process, but the power output decreases. As net GVD is further increased a CW-spike (not shown) appears in the fundamental spectrum and modelocking is no longer stable.

To obtain the highest SH power the amount of prism glass is minimized, setting a large negative net GVD. This gives near-Gaussian spectra as seen in Figure 3.3(a) and 3.3(f) and reliable operation.

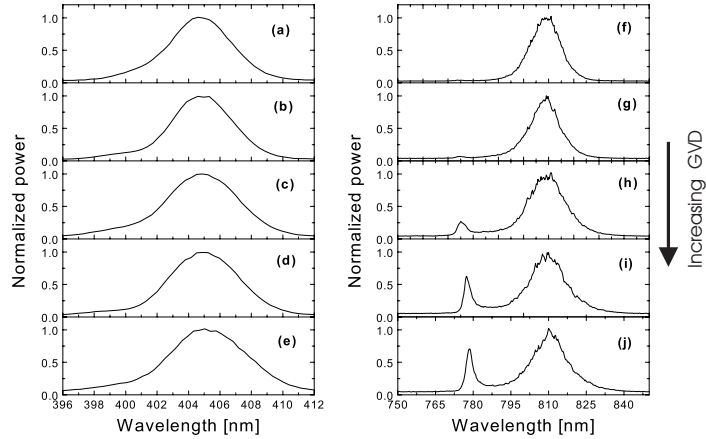


Figure 3.3: Fundamental (f-j) and second harmonic (a-e) spectra as function of prism-setting. Top curve corresponds to maximum negative GVD.

3.2.3 Characterization

Outside the cavity the SH beam is collimated by an AR coated fused silica lens with a focal length of 20 cm. The SH beam is initially vertically polarized but is sent through a half-wave plate resulting in a horizontally polarized beam. The p-polarized pulses are then compressed with two Brewster-cut fused silica prisms, resulting in 180 mW, 73 fs pulses. The fundamental pulses are collimated with a telescope and compressed to 55 fs. Figure 3.4(c) shows the trace from an interferometric autocorrelation of the fundamental pulses. The signal is measured by two-photon absorption in a GaAsP photo diode [48]. Figure 3.4(a) shows the spectrum of the fundamental pulses with a 19 nm FWHM giving a time-bandwidth product $\delta\tau\delta\nu = 0.45$ indicating almost transform-limited pulses.

To characterize the SH pulses, a collinear cross correlation of the 405 nm and 810 nm pulses is made. A 25 μm thick BBO crystal aligned for sum frequency mixing (SFM) is used as nonlinear medium, and the weak signal is measured with a photomultiplier tube and a lock-in amplifier. The group velocity mismatch for SFM in BBO is 881 fs/mm [49], so the crystal thickness of 25 μm limits the temporal resolution to 23 fs but with a fundamental pulse duration of 55 fs this is not a limiting factor. The trace is shown in figure 3.4(d). The correlation is seen to be nearly Gaussian with a FWHM of 93 fs which translates into a FWHM of 73 fs for the 405 nm pulses. Figure 3.4(b) shows the spectrum of the SH with a FWHM of 4.8 nm which then gives a time-bandwidth product of 0.63. The high product is likely due to non-compensated TOD in the

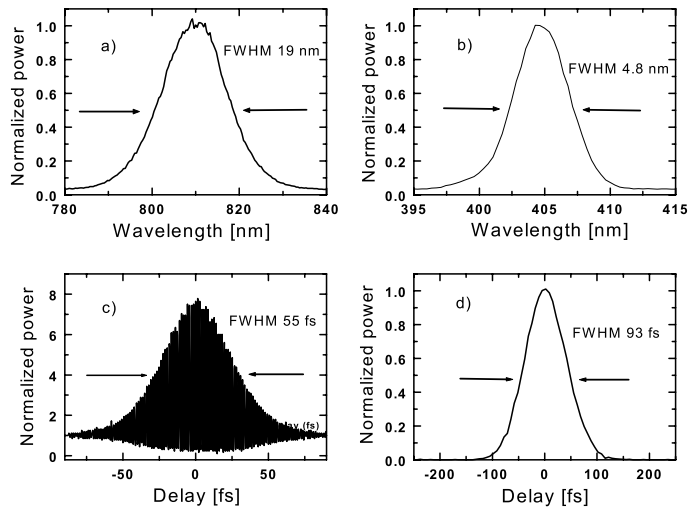


Figure 3.4: a) Spectrum of the fundamental pulses. b) Spectrum of SH pulses. c) Autocorrelation of the fundamental. d) Cross-correlation of fundamental and SH.

prism-compressor.

The red beam is found to be a nearly perfect TEM_{00} mode while the blue is slightly distorted due to the astigmatism induced by the spherical mirrors. The astigmatism also introduces a small spatial dispersion in the beam.

3.3 Optical parametric amplification

Optical parametric amplification (OPA) is a highly interesting method to generate short pulses in the visible and near-infrared. Chapter 8 will explain OPA in more detail. Here it suffices to say that OPA is a $\chi^{(2)}$ process in which an intense pump beam is converted into signal and idler beams when a phasematching condition is fulfilled. Nonlinear crystals, such as BBO, are useful media for these processes as the difference in refractive index along the crystal axes enables phasematching by simple angle-tuning of the crystal. The efficiency of the process depends mainly on the intensity of the pump and the extent of spatial and temporal overlap between beams.

The main goal of this work was to demonstrate that amplification of seed pulses generated in a PCF can take place with the blue pump power available from the frequency doubled oscillator. The seed beam is generated by launching 14 mW of the 55 fs, 810 nm beam into a $1.7 \mu\text{m}$ core PCF (Crystal fibre NL-

PM-750). The low dispersion, in addition to the small core, results in a large nonlinear response and figure 3.5 (left) shows how the relatively weak pump pulses generate large bandwidth and a pronounced peak at 650 nm (NSR). The

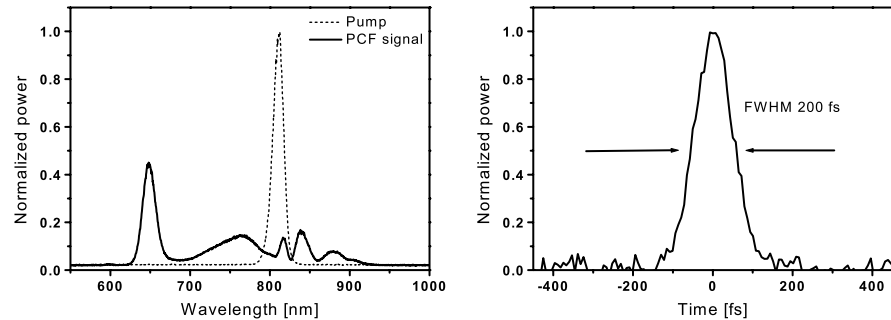


Figure 3.5: Left: Dashed and full line show the spectrum before and after the photonic crystal fiber. Right: Amplified signal at 650 nm.

visible output is overlapped spatially and temporally with the pump beam in a 1 mm BBO crystal oriented for SFM of 405 nm and 650 nm. With a collinear geometry, the beams are focused with a 10 cm focal length achromatic lens to spotsizes of roughly $80 \mu\text{m}$. After the crystal, detection of the amplified signal is done by dispersing the beam in a prism and using a 400 nm mirror and an iris as filters to ensure that only 650 nm light impinges on a photo diode. The diode records the signal through a lock-in amplifier and figure 3.5 (right) shows the signal obtained when the temporal delay between the 400 nm and 650 nm pulses is scanned. The amplified signal has a FWHM of 200 fs and proves that OPA is possible with this type of setup. The signal is however very weak. Even with harder focussing and a non-collinear geometry between pump and signal [50], amplification can not be seen by the eye (650 nm) or a power meter and lock-in detection is necessary.

3.4 Summary

The work with this setup demonstrated OPA directly from an oscillator through intracavity frequency doubling and broadband generation in a PCF. The amplified signal is however too weak to be of any use and the experiments show that more pump power is needed to make this process work efficiently. According to the literature, OPA-systems typically operate at pump intensities of the order of $10 \text{ GW}/\text{cm}^2$. With 180 mW, 73 fs pulses at 50 MHz and a spot size of roughly $80 \mu\text{m}$, the intensity in the present experiments is about two orders of magnitude too small. While some improvements can be made by focussing the

pump beam harder or optimizing the modal overlap in the BBO crystal, it will not be possible to find two orders of magnitude.

However, the idea of using a PCF as a white-light source for OPA is quite interesting and is actually being pursued by other groups now [51]. Chapter 8 will describe a second and more successful attempt of making this type of setup but this time with a high power fiber laser as pump source.

Chapter 4

Continuous wave four-wave mixing in a photonic crystal fiber

Degenerate four wave mixing in a highly nonlinear PCF is investigated. The dispersion profile of the fiber enables phasematching over a broad spectral range even at vanishing power levels and continuous wave wavelength conversion is therefore possible. The fiber could potentially be used as gain media for an optical parametric oscillator or as an optical switch.

4.1 Introduction

The work presented in this chapter was inspired by previous experiments with super continuum generation (SCG) in a highly nonlinear PCF with two zero-dispersion-wavelengths (ZDW) [52]. The experiments revealed that the SCG process was dominated by degenerate four-wave mixing (FWM) and not soliton fission as is usually the case [3]. The presence of two ZDW changed the dispersion of the fiber to such an extent that phasematching for FWM was fulfilled in the entire anomalous dispersion regime. Since FWM has very high gain [12], soliton dynamics were effectively arrested and the output consisted of two peaks centered at the ZDWs in accordance with predictions based on calculated FWM phasematching curves. The output was largely unaffected by the input pulse parameters and the simulations showed that FWM would always dominate and even take place at continuous wave power levels.

The experiments presented here confirm these ideas and demonstrate means of wavelength conversion without the need of intense pulses.

4.2 Four wave mixing

Degenerate FWM in optical fibers is a well known nonlinear process in which signal and idler (anti-Stokes and Stokes) photons are generated from two pump photons as illustrated in figure 4.1. It is a third order process and the conver-

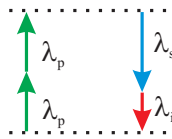


Figure 4.1: Generation of signal and idler photons from two pump photons via virtual levels.

sion efficiency of the process depends crucially on a phasematching condition (eq. 4.7), which in turn depends on the dispersion properties of the fiber. In presence of phasematching, FWM can have significant gain and can be used for efficient upconversion as well as downconversion [12]. For that reason, FWM has been exploited to make fiber-based optical parametric oscillators (FOPOs) and even optical switches for WDM systems [53]. Sharping *et al* [54] have reported a FOPO based on FWM of 600 fs pulses in a PCF and in 2002 Marhic demonstrated a FOPO using continuous wave FWM in a 100 m long PCF. By creating a cavity with fiber Bragg gratings for the signal wavelength at 1560 nm, the idler output could be tuned more than 80 nm by varying the pump wavelength [55].

In this chapter, continuous wave FWM in a polarization maintaining PCF with two ZDWs is presented. The dispersion profile enables phasematched FWM to take place in the anomalous dispersion region and several nanometers below the high frequency ZDW. A tunable output can therefore be obtained by pumping the fiber in this range while seeding with an appropriate idler.

The theory of FWM is well described in the literature [56]. In case of degenerate FWM, the electric field can be represented by

$$E(z, t) = 2E_p e^{i(k_p z - \omega_p t)} + E_s e^{i(k_s z - \omega_s t)} + E_i e^{i(k_i z - \omega_i t)} + c.c. \quad (4.1)$$

The nonlinear polarization $P_{nl} = \epsilon_0 \chi^{(3)} EEE$ of the material is then found to oscillate at many different frequencies, but for this analysis only the terms oscillating at $\omega_p, \omega_s, \omega_i$ are interesting. The following equations for the slowly varying envelopes of the three fields can then be derived [12]

$$\frac{\partial A_p}{\partial z} = i\gamma[(|A_p|^2 + 2(|A_i|^2 + |A_s|^2))A_p + 2A_i A_s A_p^* \exp(i\Delta\beta z)] \quad (4.2)$$

$$\frac{\partial A_{i(s)}}{\partial z} = i\gamma[(|A_{i(s)}|^2 + 2(|A_p|^2 + |A_{s(i)}|^2))A_{i(s)} + A_p^2 A_{s(i)}^* \exp(-i\Delta\beta z)] \quad (4.3)$$

where A_p , A_i and A_s are the normalized field amplitudes of the pump, idler and signal respectively and $\Delta\beta$ is the difference in the propagation constants given by $\Delta\beta = \beta_s + \beta_i - 2\beta_p$. Equation 4.2 and 4.3 generally have to be solved numerically but assuming an un-depleted pump ($\frac{\partial A_p}{\partial z} = 0$) it is possible to obtain an analytical expression for the signal power [12, 56]

$$P_s(L) = P_s(0)(1 + \gamma P_0/g)^2 \sinh^2(gL) \quad (4.4)$$

where g is the gain:

$$g = \sqrt{(\gamma P_0)^2 - \left(\frac{\kappa}{2}\right)^2} \quad (4.5)$$

with κ given by

$$\kappa = \Delta\beta + 2\gamma P_0 \quad (4.6)$$

and P_0 is the pump power. Maximum gain of $g = \gamma P_0$ is obtained when $\kappa = 0$, which occurs when the nonlinear phase shift ($2\gamma P_0$) is compensated by a negative wave vector mismatch, $\Delta\beta$. Expanding $\beta(\omega)$ around the pump frequency results in the phasematching condition:

$$\Omega_s^2 \beta_2 + \frac{1}{12} \Omega_s^4 \beta_4 + \frac{1}{360} \Omega_s^6 \beta_6 + \dots + 2\gamma P_0 = 0 \quad (4.7)$$

where β_2 , β_4 and β_6 are the second, fourth and sixth derivative of β with respect to ω evaluated at the pump frequency and Ω_s is the frequency shift from the pump to the signal/idler frequencies.

In conventional single mode fibers, the higher order terms are generally small and it is sufficient to include only β_2 when evaluating eq. 4.7 (except at the ZDW). In this approximation, phasematching can only occur in the anomalous dispersion regime where a negative β_2 can compensate for the positive nonlinear phase shift [12]. In highly nonlinear PCFs the significant waveguide dispersion can profoundly change the dispersion profile and higher order terms can no longer be neglected [57, 58].

4.3 Phasematching in CF NL-PM-750

The fiber in these experiments is the widely used NL-PM-750 (Crystal Fibre) which is highly nonlinear and has two ZDWs at 755 nm and 1235 nm respectively. Figure 4.2 displays the GVD in the fiber and the strong curvature of the profile implies that the higher derivatives of $\beta(\omega)$ are important. By fitting a

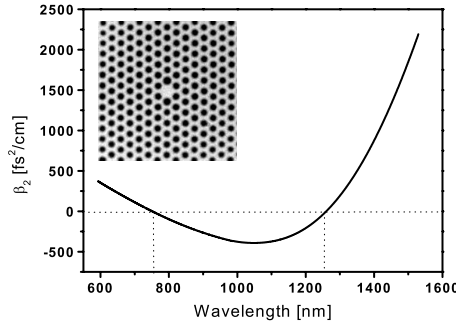


Figure 4.2: Dispersion profile measured by white light interferometry. Insert shows the cross section of the fiber. The core is surrounded by six air holes of which two are slightly bigger than the rest, resulting in birefringence. Picture and data provided by Crystal Fibre A/S.

Taylor expansion to the curve, the higher order dispersion terms can be calculated and figure 4.3 (left) shows β_2 , β_4 , β_6 and β_8 as functions of wavelength between the two ZDWs. The shown curves have been scaled according to

$$\beta_{n,scaled} = \frac{2}{n!} (10^{15} \text{ s}^{-1})^{(n-2)} \beta_n. \quad (4.8)$$

in order to compare the strength of each term in eq. 4.7. The figure indicates how the size and changing signs of the higher order terms may result in phasematching in the anomalous dispersion regime even without a nonlinear phase

contribution. Figure 4.3 (right) shows that phasematching may also take place in the normal dispersion regime close to the ZDW where the negative β_4 and β_8 can compensate for the positive β_2 and β_6 . Figure 4.4 shows a phasematch-

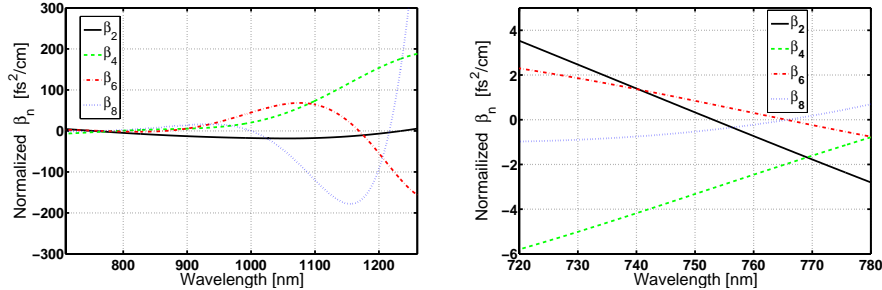


Figure 4.3: Left: The scaled dispersion terms β_2 , β_4 , β_6 and β_8 as functions of wavelength. Right: A zoom on the high-frequency ZDW shows that β_4 and β_8 are negative below the ZDW. They can therefore compensate for the positive β_2 and β_6 .

ing diagram based on the measured β_2 without a nonlinear phase contribution (peak power, $P_0 = 0$). Phasematched signal and idler wavelengths are found on vertical lines for a given pump wavelength. The curve differs from similar phasematching curves for PCFs with only one ZDW, for which phasematching at low power is only possible slightly below the ZDW [35]. In the present fiber, however, phasematching is fulfilled in the anomalous dispersion region and several nanometers below the high-frequency ZDW.

At higher pump powers the phasematching is eventually perturbed by the nonlinear contribution $2\gamma P_0$. With a pump peak power of 1000 W, a new set of closely lying phasematched wavelengths appears in the anomalous regime, while the normal regime remains virtually unaltered - see left panel of figure 4.4. The curves show that phasematched wavelengths are found between 500 nm and 1800 nm so a widely tunable output is possible.

Figure 4.4 (right) shows a zoom on the phasematching curve close to the low-wavelength ZDW at approximately 755 nm and illustrates how tuning of the pump from ~ 741 nm to 755 nm, allows generation of phasematched wavelengths continuously between 500 nm and 1500 nm. Furthermore, there are pump wavelengths for which two sets of phasematched wavelengths are possible simultaneously. This multiple frequency generation has previously been predicted [59–61], but has so far not been confirmed experimentally. Figure 4.4 (left) also indicates that multiple frequency generation is possible in the entire negative dispersion region when the fiber is pumped with high power. It would be interesting to study this phenomenon in more detail since it could bring further understanding of the SCG processes in this class of fiber [52].

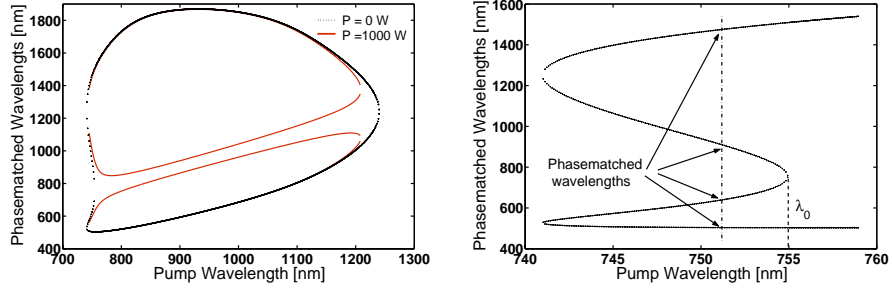


Figure 4.4: Left: Phasematching with $\gamma P_0 = 0$. Phasematched Stokes and anti-Stokes wavelengths are found on vertical lines. Right: Closeup of the phasematching curve at the lowest ZDW. Below ~ 755 nm, two sets of wavelengths can be phasematched simultaneously as indicated by arrows.

4.4 Experimental results

The phasematching curves in figure 4.4 predict that a tunable output from 500 nm-1500 nm can be obtained by tuning the pump wavelength in the vicinity of the ZDW at 755 nm while seeding with an appropriate idler. To demonstrate this, the output from a Ti:Sapphire laser operating in CW mode at 750-830 nm and a laser diode centered at 975 nm are overlapped and coupled into a 20 meter long piece of the PCF with a microscope objective (figure 4.5). The fiber has a

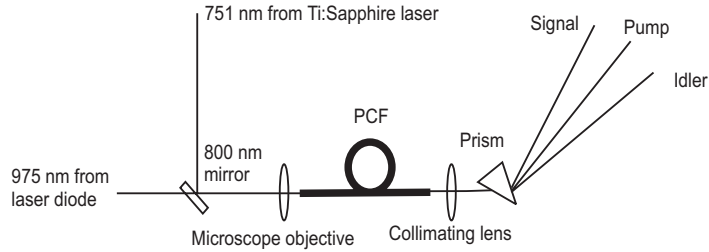


Figure 4.5: Experimental setup

$1.7 \mu\text{m}$ core surrounded by six air holes of which two are larger than the rest - as seen in the insert in figure 4.2. The resulting birefringence of $\Delta n > 3 \cdot 10^{-4}$ is enough to make the fiber highly polarization maintaining. The pitch of the fiber is $1.2 \mu\text{m}$ while the average hole size is $0.55 \mu\text{m}$ [62]. To ensure excitation of only one polarization mode, the fiber is mounted in a rotational stage and

aligned with its major axis parallel to the polarization of the Ti:Sapphire laser. Light from the 975 nm diode is polarized in the same orientation by appropriately bending the delivery fiber [14]. When the pump wavelength is scanned to 774 nm, a signal appears at 641 nm as shown in figure 4.6 a). By tuning the

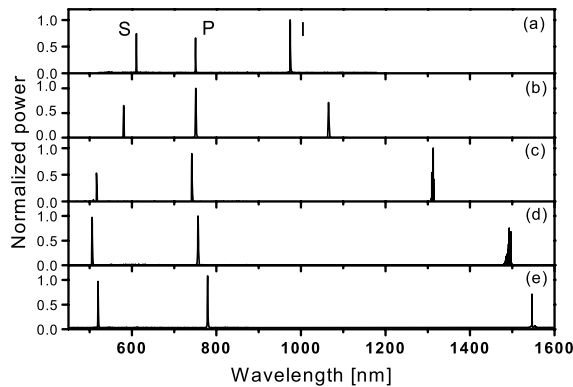


Figure 4.6: Spectra at phasematching. In (c), (d) and (e) the visible and infrared spectra were recorded with different detectors and joined here for clarity. In some cases the output from the fiber is filtered to avoid saturation of the detector. The relative size of the peaks does therefore not represent the actual power distribution. In all figures, the left peak is the signal while the middle and right peaks are pump and idler respectively.

pump wavelength and seeding with idler sources at 1064 nm, 1312 nm, 1493 nm and 1549 nm, similar results are obtained as illustrated in figure 4.6(b)-(e). All signal outputs are found to be linearly polarized along the same axis as the pump light, meaning that the birefringence of the fiber keeps the light in one polarization state. Coupling into the other polarization axis of the fiber results in a similar set of linearly polarized phasematched wavelengths. Figure 4.7 shows the measured sets of phasematched wavelengths along each of the two axes. The filled squares connected with full lines indicate measured values while the dotted line is the theoretical curve previously shown in figure 4.4. The discrepancy between the measured and calculated phasematching is due to the fact that the dispersion is measured by white light interferometry [63] using an unpolarized light source. The GVD in figure 4.2 is therefore an average of the GVD in the two polarization axes of the fiber (arbitrarily labelled as major and minor axis respectively) and the calculated phasematching diagram does therefore not relate directly to any of the measured data sets in figure 4.7. However, the qualitative shape of the phasematching curve is readily recognized in both axes (full lines) and extrapolation can be made to predict where phasematching can be found.

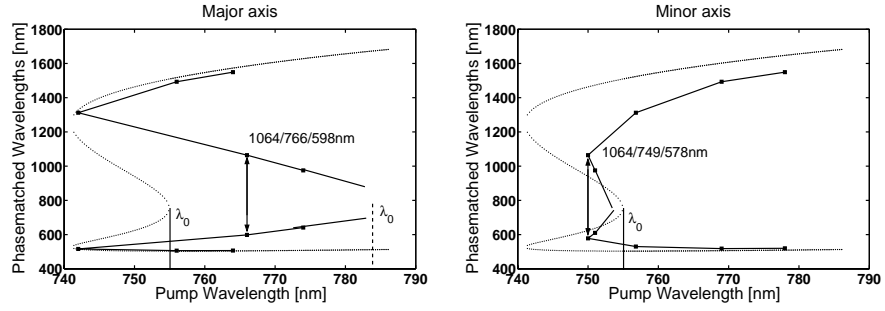


Figure 4.7: Measured phasematched wavelengths along the two axes. Each axis has its own zero-dispersion wavelength which shifts the phasematching curve. The dotted line is the calculated phasematching curve from figure 4.4 while the solid line connects the measured datapoints shown as squares. The experimental data indicate that the major axis has zero dispersion at $\lambda_0=785$ nm.

Figure 4.8 (left) shows the output power at 518 nm as a function of 769 nm pump power, when phasematching with a 1493 nm idler is obtained along the minor axis of the fiber. The curve is in qualitative accordance with the analytical approximation in eq. 4.4 and displays a maximum signal power of $12 \mu\text{W}$ when the fiber is pumped with 200 mW and seeded with 40 mW of the idler at 1493 nm. This corresponds to a conversion efficiency from idler to signal power

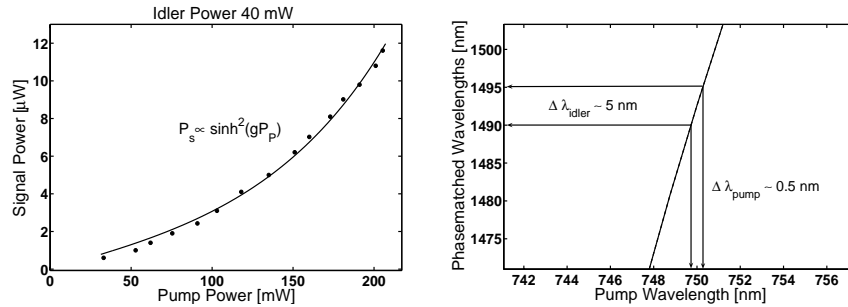


Figure 4.8: Left: Measured power at 518 nm as a function of pump power when the idler power is 40 mW. The full line is the analytical approximation given in eq. 4.4 Right: The steep slope of the phasematching curve implies that only a part of the pump is actually matched to the laser diode at 1493 nm.

of 0.3%, which is lower than expected from numerical integration of eq. 4.2 and 4.3. It is however necessary to include the spectral width of the sources in the calculation. Figure 4.8 (right) illustrates how the steep slope of the phasematching curve maps the 5 nm wide spectrum of the laser diode at 1493 nm

onto an interval of 0.5 nm on the pump axis. The Ti:Sapphire laser is designed for pulsed operation so even when it is forced to run CW, the line-width is about 4 nm. Therefore, only a part of the pump power actually participates in the mixing process which explains that the measured conversion efficiency is lower than expected. The theoretical expressions (eq. 4.2-4.3) predict that 200 mW of pump power, combined with 40 mW of idler power, should result in 2 mW at the signal wavelength if the bandwidths were matched. This corresponds to an idler-to-signal conversion efficiency of 5%. With the advent of high power, narrow line width diode lasers [64] such conversions will be possible with simple and compact setups. Additional improvements can be obtained by seeding the fiber at the signal wavelength as well. This could be done with a simple re-coupling of signal power or by creating a cavity around the fiber (FOPO) [54, 65]. It should be noted that fluctuations in the core dimensions along the length of the fiber are known to cause a reduction in bandwidth and gain of the FWM process [66] so the quality of the fibers is also critical for optimum performance.

4.5 Summary

Continuous wave FWM in a PCF with two zero-dispersion wavelengths is demonstrated. The dispersion profile of the fiber allows phasematched degenerate FWM to take place in the anomalous dispersion regime at low CW pump powers and the experiments verify predicted phasematching at five different pump wavelengths. In combination with calculated phasematching curves, the experiments indicate that a large span of wavelengths can be matched by tuning the pump laser only a few nanometers in the vicinity of the lowest ZDW. A conversion efficiency of 0.3 % from an idler at 1493 nm to a signal at 518 nm is obtained but is limited by the low spectral density of the available pump. Improved conversion can be obtained by employing narrow-band pump sources or using the fiber in a FOPO setup.

Chapter 5

Q-switched fiber laser

An all-fiber Q-switched laser is developed with industrial applications in mind. The experiments presented here serve as a proof of principle and show that pulsed sources can be made with simple means.

Aiming at the marking industry, NKT-Research set out to make pulsed fiber lasers. Typical target parameters were 100 ns pulses at a repetition rate of 10 kHz so Q-switching was the natural route to take. The basic idea was to use existing (cheap) telecom components to make a pulsed source and then amplify the output in a high power double-clad large mode area (LMA) fiber. Several Q-switching schemes were tested, and in this chapter an all-fiber solution will be described. The laser was developed in collaboration with Miguel Andrés' group at the University of Valencia in Spain.

5.1 Introduction

Fiber lasers represent an attractive alternative to conventional solid state lasers due to superior beam quality, efficiency and compactness. In recent years the performance of fiber lasers has greatly improved, and pulsed as well as continuous wave fiber lasers can now deliver power levels comparable to those of standard workhorses such as the Nd:YAG [67, 68].

Q-switching is a well known technique to obtain powerful pulses of 1-500 ns duration and Q-switched lasers are used extensively in laboratories and in industry. Q-switching of fiber lasers has been demonstrated in a variety of ways [22] and the potential simplicity of such lasers makes them interesting for various applications in medicine, sensing and material processing. In general, Q-switched fiber lasers are however flawed by the inclusion of a bulk switching device such as acousto-optic modulators [69] or saturable absorbers [70–73]. These components greatly increase the complexity of the setups since light must be coupled in and out of the fiber. The necessary mechanical stability may be incompatible with practical applications and it is therefore highly interesting to develop all-fiber alternatives. Self-Q-switching in optical fibers due to Brillouin and Rayleigh scattering [74, 75] may be exploited for this purpose, and it has also been suggested to use Samarium-doped fiber as a saturable absorber to Q-switch Er-doped lasers [76]. However, in passively Q-switched lasers, important parameters such as pulse duration and repetition rate are partly determined by the characteristics of the saturable absorber and cannot be controlled directly. For some applications, it is necessary to control these factors and simpler all-fiber actively Q-switched solutions are therefore desirable.

There are very few examples of all-fiber actively Q-switched lasers in the literature. In 1993, Chandonnet *et al* used a side-polished coupler to modulate the cavity losses and obtained Q-switching in an Er-doped fiber laser [77]. Another attempt relied on modulating a Bragg grating with a piezoelectric element, but to get sufficient modulation it was necessary to work at the mechanical resonance of the piezoelectric and operation was therefore bound to take place at harmonics of this resonance frequency [78].

More recently, an all-fiber actively Q-switched laser based on magnetostric-

tive modulation of a Bragg grating was reported. With the chosen dimensions of the magnetostrictive rod (MSR), there were no limiting resonance frequencies below 10 MHz and it was possible to obtain 200 ns pulses from an Er-doped fiber laser at repetition rates from 1-125 kHz [79].

In this chapter, improvements of this latter technique are presented and Q-switching of an Yb-based laser is demonstrated. The improvements and the change to Yb-doped fiber have resulted in powerful and stable pulses at 1052 nm and has enabled Q-switching at repetition rates up to 200 kHz. The laser constitutes the first realization of an all-fiber actively Q-switched Yb-doped laser.

5.2 Experimental setup

Figure 5.1 shows the setup. A standard 976 nm pump diode is connected to the doped fiber by a 976/1052 nm Wavelength Division Multiplexer (WDM). An additional 976/1030 nm WDM is used to remove unwanted amplified spontaneous emission (ASE) around 1030 nm which would otherwise cause lasing on reflections from the pump front facet and spurious feedback from the cavity. In

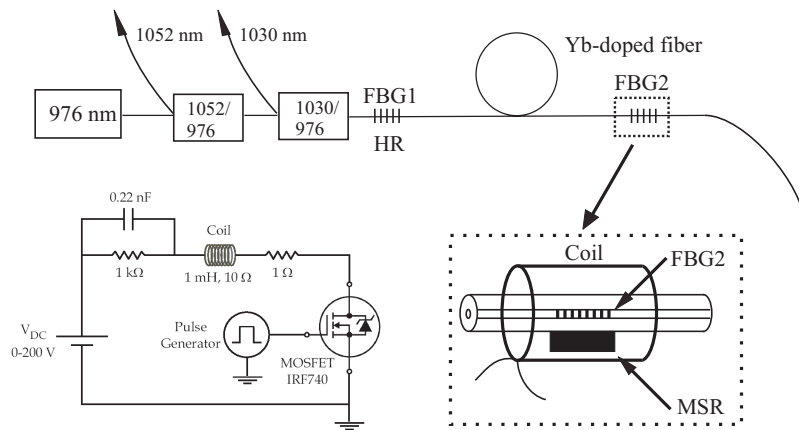


Figure 5.1: Experimental setup. The fiber Bragg grating in the output end of the fiber (FBG2) is fixed on a magnetostrictive rod and placed inside a electric coil. The high-reflecting grating (FBG1) is fixed to a translational stage and stretched with a constant strain. All fiber ends are terminated with angle polished connectors. The circuit used to drive the current in the coil is depicted.

this particular setup 1.5 m of heavily doped Yb-fiber is used as gain medium. The fiber has a small signal absorption of 200 dB/m at 976 nm, a core diameter of 4.6 μm and a NA of 0.16. Two gratings have been written directly in the

doped fiber by UV-exposure through a phase mask [80]. The estimated linewidths of the gratings are 0.07 nm and both gratings have a Bragg wavelength of 1051.5 nm. One grating (FBG2) is 12 mm long and has a reflectivity of 85 % while the other (FBG1) reflects 99 %. A $1 \times 1 \times 15$ mm rod of the magnetostrictive material Terfenol-D [81] is fixed to the doped fiber at the site of FBG2 and Q-switching is performed by placing the rod and the fiber inside a small coil and applying current pulses. The rod, and thereby the grating, are then stretched and relaxed by the resulting magnetic field. The modulation frequency can be tuned continuously from 1-200 kHz in this way.

FBG1 is stretched with a constant strain in order to shift the reflectance curve towards longer wavelengths. When the magnetic pulses stretch FBG2, the two gratings are brought to coincide in wavelength for short periods of time which results in an increased Q-value - as illustrated in figure 5.2. It is necessary

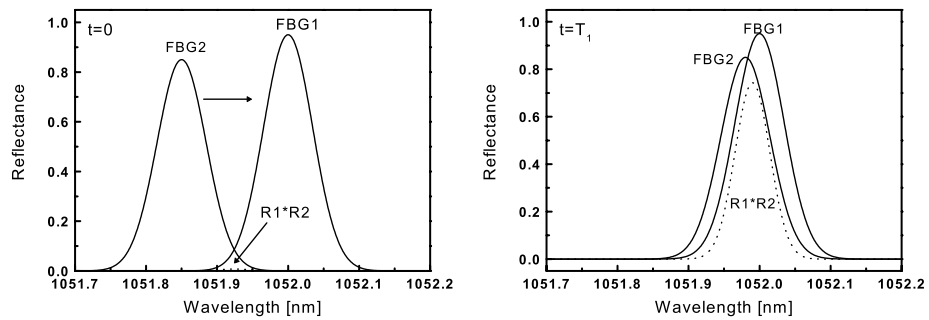


Figure 5.2: Illustration of Q-switching. A constant strain is applied to FBG1 to shift the reflectance curve (R1) towards longer wavelengths. At time $t=0$ (left) current is applied to the coil and FBG2 is gradually stretched. As a result, the reflectance of FBG2 (R2) is shifted towards that of FBG1 and at time $t=T_1$ the gratings overlap in wavelength and the Q-factor of the cavity is high - as illustrated by the product of the two reflectance curves, $R1 \cdot R2$.

to apodize the gratings to avoid pre-lasing on reflective sidebands. A FBG is made by doping the fiber (with e.g. Germanium, Hydrogen) and subsequently exposing the fiber to UV light. The energetic UV photons create defects at the dopant sites which cause an increase of the index of refraction of up to a few percent. Phase masks are used to ensure spatial periodicity of the UV-exposure since it is the periodic variation in the refractive index which cause the reflection. Figure 5.3 (left) shows such an index modulation schematically. The resulting reflectivity of the grating can be approximated by Fourier transforming the index variation [80] as shown in figure 5.3 (right). The finite length of the index modulation invariably leads to sidebands on the reflectivity curve (the Fourier transform of a top-hat distribution is a sinc-function).

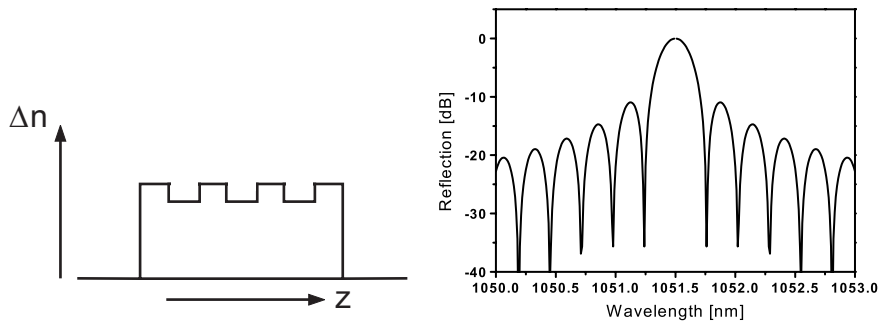


Figure 5.3: Left: Illustration of an index profile along the length of the fiber after UV-exposure. The periodic variation in the refractive index cause multiple reflection which interfere constructively and thereby add up to a strong reflection. Right: The reflectivity of the index variation in the left panel can be approximated by Fourier transforming it. Since the Fourier transform of a 'top-hat' distribution is a sinc-function the resulting reflectivity displays sidebands.

Such sidebands are detrimental to the performance of the Q-switched laser presented here. Since the reflectance profile of FBG2 is shifted back and forth in wavelength during operation, the sidebands cause lasing before the main reflective peaks are coinciding. When this 'parasitic' lasing takes place, satellite pulses are emitted and the gain is clamped at a low value, resulting in a weak multi-pulse output. To minimize such problems, the used gratings are subjected to a Gaussian apodization. Apodization implies varying the intensity of the UV-light along the length of the grating in order to make a gradual transition from high to low index instead of the steep edges shown in the left panel of figure 5.3. It is desirable to make 'gaussian wings' since a near gaussian index modulation gives rise to a near gaussian reflective profile i.e. a profile without sidebands (not shown). In practice it is however difficult to completely remove the sidebands and the gratings used for these experiments still have sidebands about 25 dB below the main reflective peak. In spite of this weak reflectivity, the sidebands actually cause lasing in the highly inverted Yb-doped fiber. This turns out to be a limiting factor for the setup and further development of the apodization technique is therefore needed.

The electronic circuit is designed to be able to drive square current pulses with amplitudes of up to 250 mA through a small electrical coil. The current in the coil is supplied by a DC voltage source and a MOSFET, driven by a low voltage pulse generator, is used to switch the DC current on and off. The natural rise time for the current in the coil is approximately 100 μ s and is determined by the coils self-inductance and resistance of about 1 mH and 10 Ω ,

respectively. The rise time can be reduced to $1 \mu\text{s}$ by placing a capacitor of 0.22 nF and a resistance of $1 \text{ k}\Omega$ in the circuit as depicted in figure 5.1. Under these conditions, the maximum repetition rate of the optical pulses is not limited by the electronics but by the magnetostrictive frequency response and the lifetime of the excited state of Yb^{3+} .

The magnetostrictive rod responds linearly to the magnetic field and at repetition rates below 100 kHz there is no significant frequency dependence. The shift of the Bragg wavelength as a function of the current applied to the coil was determined by using a narrow line-width tunable laser and was found to be 0.4 nm/A [79]. Currents of 200 mA are thus sufficient to shift the wavelength by more than the spectral width of FBG1. As a result, Q-switching can be obtained with current amplitudes of less than 100 mA at these frequencies. If the frequency is increased, the magnetostrictive response of the rod decreases and higher currents are needed. At 200 kHz the response of the rod is significantly reduced and about 250 mA are needed to obtain Q-switching.

5.3 Results

The Q-switched laser in figure 5.1 has distinct regimes of operation which can be chosen by stretching FBG1 with an appropriate constant strain. If the reflectance of FBG1 is shifted to a longer wavelength than the reflectance of FBG2, high Q-values are obtained when current is applied to the coil and the magnetic pulses stretch FBG2 far enough for it to coincide with FBG1 (see figure 5.2). This is the method used in the following. On the other hand, without strain on FBG1, the two gratings are initially matched and a high Q-factor is established when the current is switched off and FBG2 relaxes to its initial state. In between these two regimes of operation, an intermediate strain applied to FBG1 leads to un-interrupted lasing and a weakly modulated continuous wave output with higher average power than when Q-switching takes place. This is due to FBG2 being shifted within the bandwidth of FBG1 and thereby keeping the cavity Q-factor high.

Since the spectral overlap of the two gratings determines the Q value of the cavity, the pulse parameters are highly dependent on the exact strain applied to FBG1. To make reproducible measurements, the following method is adopted: FBG1 is stretched until the intermediate regime of continuous wave operation is found. This is easily done by optimizing the average power. From here FBG1 is further stretched until stable, clean pulses are obtained.

Figure 5.4 shows a pulse train at 150 kHz and a representative pulse at 60 kHz . The asymmetric pulse shape in both panels is typical for Q-switching and is due to reduced gain at the trailing edge of the pulse which leads to slower energy extraction [43]. In this particular case the extraordinary long tail of the pulses is however due to the response of the detector.

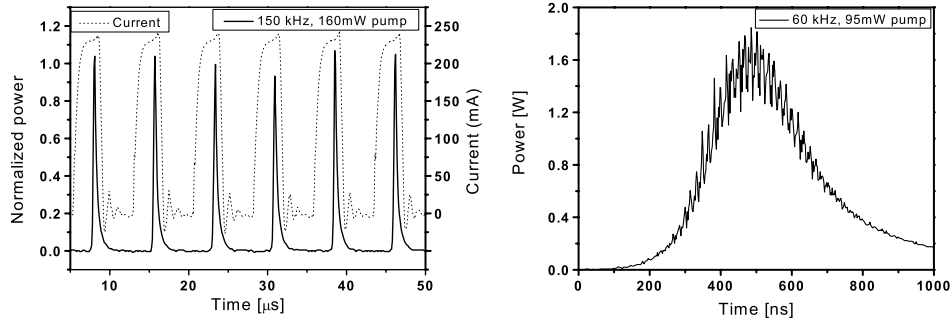


Figure 5.4: Left: Measured pulse train at 150 kHz and 160 mW of pump power. The dashed line shows the current through the coil. Right: Representative pulse at 60 kHz. The envelope of the pulse is modulated with the cavity mode spacing which indicates beating between longitudinal modes.

The amplitude fluctuations seen on the pulse train are mainly due to the sampling of the oscilloscope, but more precise measurements reveal that there is real amplitude jitter of up to 10 %. These fluctuations might be caused by irregular modulations of the pulse envelope as seen on figure 5.4 (right). Although the resulting spikes cause large amplitude fluctuations, they are too short to carry substantial energy and, in fact, the total pulse energy is stable within 3 %. The modulation of the pulse envelope is periodic with the round trip time of the cavity, indicating beating between longitudinal cavity modes. This is surprising since the spectral width of the gratings should allow many longitudinal modes to oscillate, which in turn should wash out any interference effects. Similar pulse modulations have also been reported when fast Q-switching devices (AOMs) are used. In that case the modulation originates from repetitive amplification of the initial ASE waves injected by the fast switch [82]. Such effects are however only relevant when the rise time of the switch is of the order of the cavity round trip time and the slow switching employed in the present experiments ($5 \mu\text{s}$) should therefore not cause any modulation of the pulse envelope. To study these effects in more detail, a numerical model has been developed and is presented in Appendix B. The model indicates that the modulation is not caused by the switching time, but arises due to a time-dependent phase-shift caused by the moving grating (FBG2). When the sweeping process is started, waves are initiated by FBG2 at $z = L$ and these waves propagate towards the input end of the fiber where they are reflected by the stationary grating with a frequency dependent phase-shift [83]. However, at the moving grating, the waves also obtain a time-dependent phase shift and the resulting phase difference between frequency components generates a beating over the pulse envelope. Figure 5.5 (left) shows a theoretical pulse envelope from a simulation where a

time-dependent phase shift is included at FBG2. The pulse has noise spikes with a period corresponding to the cavity round trip time as is observed experimentally. Similar effects have been reported previously [84] and the modulation is therefore believed to originate from the motion of the grating. This idea is supported by experiments with pulsed distributed feedback fiber lasers where the gratings are stationary. Amplitude modulations are not observed with such configurations [85]. Figure 5.5 (right) depicts the average output power as a

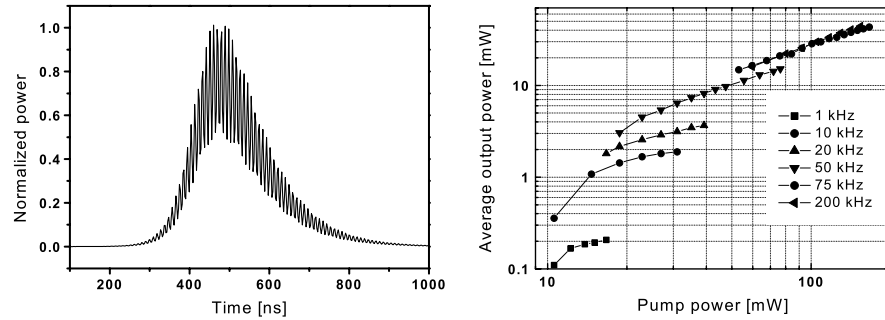


Figure 5.5: Left: Theoretical pulse based on a coherent model where the moving grating induces a time-dependent phase-shift. The beating between modes leaves a modulated pulse envelope. Right: Average output power versus pump power for different repetition rates. Curves are truncated when additional pulses appear. At high frequencies the threshold for stable pulsed operation increases.

function of pump power for different repetition rates. For a given repetition rate there is a pump level beyond which extra pulses appear and the curves are truncated at that point. Such multi-pulsing is a well-known problem in actively Q-switched lasers and is an indication of slow Q-switching [43]. Furthermore, the weak sidebands of the gratings overlap before the central reflective peaks coincide, causing pre-lasing and even relaxation oscillations, before the main pulse. As a result, the extractable pulse energy is low and the quality of the pulse train is compromised by weak satellite pulses. These effects are strongly gain-dependent and are not observed at repetition rates above 100 kHz. In contrast, at a repetition rate of 10 kHz, extra pulses appear already at 18 mW of applied pump power.

Figure 5.6 (left panel) shows the average and peak output power as functions of repetition rate for a fixed pump power of 70 mW. The average power approaches a constant level as the repetition rate is increased towards a quasi-CW regime and the lower gain per pulse results in decreasing peak power. There is an optimal frequency range between 70-85 kHz where a reasonable compromise between peak power and average power can be made. Figure 5.6 (right) shows the pulse duration and peak power versus pump power when the laser op-

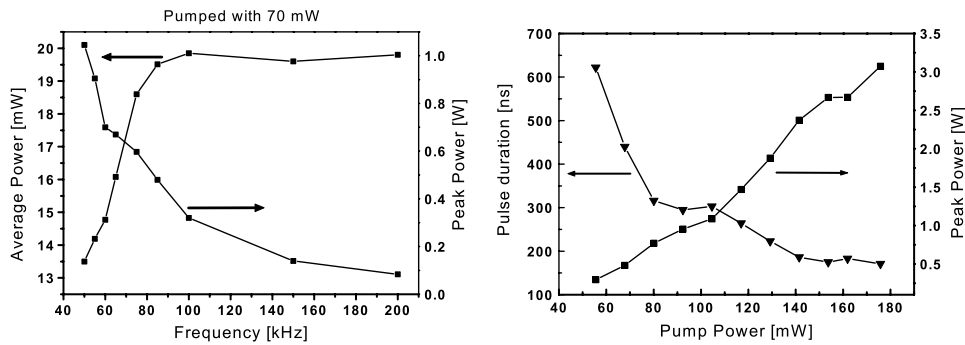


Figure 5.6: Left: Average power and peak power versus frequency for a fixed pump power of 70 mW. Right: Pulse duration and peak power versus pump power for operation at 85 kHz

erates at 85 kHz. The pulse duration is seen to decrease with increasing pump power while the peak power increases accordingly. Peak powers of 3 W and pulse durations of roughly 180 ns, corresponding to pulse energies of more than 500 nJ, were realized at this frequency. The trends illustrated in both panels of figure 5.6 are general for Q-switched lasers [22, 43], and are also reproduced by the model in Appendix B.

5.4 Outlook

Industrial applications, such as marking or welding, require pulse energies in the mJ range so for the present setup to be interesting in this context, significant amplification of the output is needed. Initial attempts have been made with a high power diode pumped double clad LMA fiber amplifier. By seeding the LMA fiber with the Q-switched pulses, a pulse energy of 60 μJ (gain of 14 dB) was obtained when the Q-switch operated at 50 kHz. Figure 5.7 shows the amplified output power as function of diode pump power. The obtainable pulse energy was limited by ASE in the amplifier fiber. Beyond 7 W of pump power, the level of ASE grew rapidly and no further signal amplification took place. This indicates that the amplifier fiber was not saturated with signal power and more seed power is therefore needed.

To reach mJ pulse energies it is necessary to operate the amplifier fiber at low repetition rate in order to ensure high gain for each pulse. On the other hand, build-up of ASE between pulses must be avoided so a repetition rate of 10 kHz is beneficial. Unfortunately, operation at low repetition rates seriously limits the output power from the Q-switched laser (see figure 5.5). As explained previously, low repetition rates lead to multi-pulsing due to the high gain and

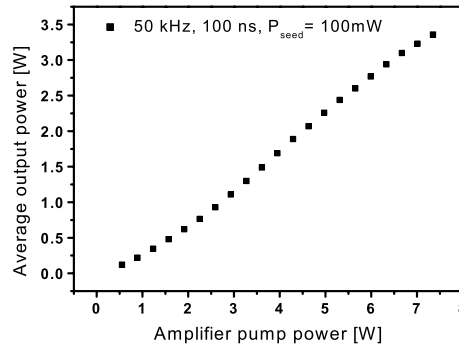


Figure 5.7: Output power from the DC-fiber amplifier as function of pump power.

spectral overlap of the FBG sidebands. Two routes can therefore be followed to reach the necessary output levels: Several amplifier stages can be built after the cavity in order to boost the average power from the present configuration. The inclusion of more stages and the need of ASE-filtering will however increase the complexity, size and cost of the setup, making it un-attractive from a practical point of view. The remaining option is to perform the Q-switching directly in a LMA double clad fiber. This can be done by either writing the gratings directly into a doped LMA fiber or by simply splicing the presently used gratings to the LMA fiber. The increased core area and low NA of such a fiber will reduce ASE and lead to much higher energy storage. It will be possible to extract sufficient average power to saturate a high power fiber amplifier [86] and the two components, cavity and amplifier fiber, can be integrated in one compact setup. Further improvements could be obtained by replacing the current Gaussian-apodized gratings with sinc-apodized gratings [87]. This type of apodization leads to nearly square reflection profiles without sidebands, so the limiting pre-lasing, caused by the early spectral overlap of the gratings, could be avoided.

5.5 Summary

An all-fiber actively Q-switched laser is demonstrated. By fixing a fiber Bragg grating to a magnetostrictive rod, it is possible to modulate the grating continuously at up to 200 kHz by exposing the rod to a changing magnetic field. This is done by placing the rod and the grating in a small electrical coil which is driven by a simple circuit. The Q-factor of the cavity is rapidly changed as the Bragg wavelength of the grating is varied and a pulsed output is realized. Depending on pump power and repetition rate, it is possible to obtain pulse durations as short as 200 ns and peak powers over 3 W. At all repetitions rates

there are pulse amplitude fluctuations of about 10 % due to beating between longitudinal modes. The resulting spikes are short and carry very little energy and the pulse-energy fluctuations are therefore small (3 %).

Amplification of the pulsed output in a high power double clad LMA fiber resulted in 60 μJ pulses but the seed power was not sufficiently high to saturate the amplifier. Consequently, further power scaling depends on the ability to generate more seed power. The output from the Q-switched laser is limited by ASE and pre-lasing which lowers the gain and constrains the applicable pump power.

It would be interesting to use this technique to Q-switch a LMA fiber. The increased energy storage would allow better power extraction and provide enough seed for a power amplifier. Further research will reveal whether this concept can deliver sufficient pulse energy to address industrial applications.

Chapter 6

Fiber dispersion measurements with white-light interferometry

A compact and user friendly setup for dispersion measurement, based on the white-light-interferometry spectral technique, is presented. The setup was made on request from NKT-Research and is now used to characterize the products from Koheras and Crystal Fibre. The work was done in collaboration with Carsten Krogh Nielsen.

6.1 Introduction

Control of the group velocity dispersion and higher order dispersion terms become paramount when working with femtosecond pulses. As seen in previous chapters, the dispersion plays a key role in phasematched nonlinear processes and actually defines the wavelengths which can be generated through FWM and emission of NSR. Furthermore, the use of air guiding photonic bandgap (PBG) fibers for intracavity dispersion compensation or extra-cavity pulse compression are emerging as an attractive applications of these fibers. To take advantage of the new technology, it is therefore necessary to develop reliable and simple setups to measure the dispersion.

The commercially available systems for this task employ the differential phase shift method in which light from a broadband source is intensity modulated at high frequencies and sent through the fiber. The propagation speed of the modulation depends on the optical wavelength and can be measured accurately by comparison with a reference oscillator [88]. This method requires a broadband laser which can be modulated at high speeds (up to GHz) and also relies on complicated electronic filtering. Alternatively, the dispersion can be measured by time of flight experiments [89]. A tunable pulsed laser source is used to map the propagation time through the fiber as function of wavelength. Apart from the need of a complex laser system, the method requires long pieces of fiber in order to reach reasonable accuracy and suffers from rather long recording times.

Therefore, it is of interest to look into simpler and less expensive alternatives. The white-light-interferometry technique [63] is based on a very simple setup, where the interference signal from a Michelson interferometer (with the fiber under test in one arm) is used to extrapolate the dispersion. In reference [63] the temporal interference signal is recorded, while the length of the reference arm of the interferometer is scanned. The dispersion is calculated via a Fourier Transform (FT) of the temporal signal and subsequent analysis of the spectral phase. Since the FT requires high temporal resolution, the interference pattern from a HeNe laser is used to monitor the scanned length. As a consequence, both signal and the HeNe calibration laser require a highly stabilized environment - which is a serious limitation for any practical implementation.

We therefore tested a different approach to whitelight interferometry for dispersion measurements in which the signal is recorded with a spectrum analyzer [90]. This has several advantages: The spectrum of the signal is also the FT of the temporal signal and the need of the HeNe laser is thereby removed. Furthermore, the short recording time of a few seconds greatly reduces the stability requirements and finally, the data processing is faster as the computationally demanding FTs are done immediately.

6.2 Experimental setup

Figure 6.1 presents a sketch of the experimental setup. A short piece of Yb-doped fiber is pumped by a 150 mW 980 nm diode laser and the resulting ASE is sent through an interferometric setup with the fiber under test in one arm and an air path of variable length in the other. Lasing in the doped fiber is prevented by using angled end facets and optical isolators between the interferometer and the Yb-fiber. A fiber coupled 50/50 thin film beam splitter is used to divide the

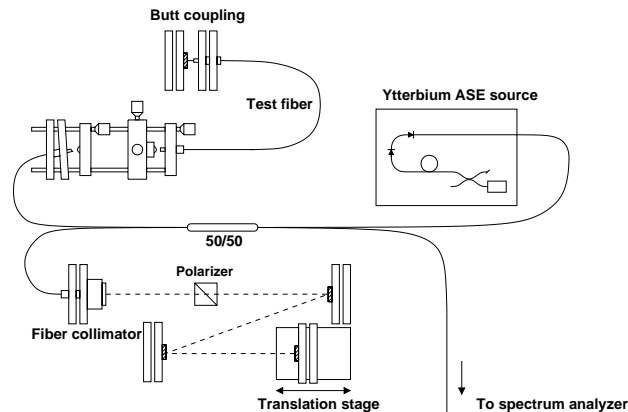


Figure 6.1: Sketch of the experimental setup of the whitelight interferometer. Light is coupled into the testfiber via a lens system which enable proper excitation of the fundamental mode.

signal in the Michelson-like interferometer. In one arm the test fiber is inserted and a lens system is used to maximize the coupling between the standard fiber of the 50/50 coupler and the test fiber. The other end of the test fiber is butt coupled to a mirror.

In the reference arm, the beam is collimated and reflected on a mirror positioned on a translational stage. In case of birefringent test fibers, a polarizer is placed in the reference arm to pick out one polarization. The correct angle of the polarizer is easily found by minimizing the amplitude of the beats in the spectrum. Each axis of the birefringent fiber can then be tested independently, assuming that there is no significant polarization evolution in the coupler fiber.

It is advantageous to use a fiber based interferometer since the setup can be made very compact and the output is easily directed towards the various detectors. The drawback is an increased sensitivity to environmental perturbations such as vibrations and especially air disturbances around the fibers. With the

fiber lying freely, phase fluctuations of 2π occur on a timescale of a few hundred milliseconds, but by placing the setup in an air tight box, the few-seconds measurements can be made with a stable phase.

6.3 Theory

Let E_r and E_f be the electric fields of the reference arm and fiber arm at the output of the interferometer

$$\begin{aligned} E_r &= E_{0,r} \exp(ik2d - i\omega t) \\ E_f &= E_{0,f} \exp(i\beta 2L - i\omega t + i\phi_0) \end{aligned}$$

where L is the length of the test fiber and d is the length of the air path in the reference arm. β and $k = \frac{\omega}{c}$ are the propagation constants in the fiber and air path respectively and ϕ_0 is any relative phase difference that may appear due to unbalanced arms in the interferometer.

The intensity measured by the detector in the spectrometer is then given by

$$I(\omega) = |E_{0,r}|^2 + |E_{0,f}|^2 + 2E_{0,f}E_{0,r} \cos(\phi(\omega)) \quad (6.1)$$

where $\phi(\omega) = \phi_0(\omega) + 2[\beta(\omega)L - \frac{\omega}{c}d]$. By expanding the propagation constant around a center frequency ω_0 , we get the following expression for $\phi(\omega)$

$$\begin{aligned} \phi(\omega) &= \phi_0(\omega) + 2[\beta(\omega_0)L - \frac{\omega_0}{c}d + [L\frac{\partial\beta}{\partial\omega}(\omega_0) - \frac{d}{c}](\omega - \omega_0) \\ &\quad + \frac{L}{2}\frac{\partial^2\beta}{\partial\omega^2}(\omega_0)(\omega - \omega_0)^2 + \frac{L}{6}\frac{\partial^3\beta}{\partial\omega^3}(\omega_0)(\omega - \omega_0)^3 + \dots] \end{aligned} \quad (6.2)$$

$\phi(\omega)$ can be constructed from the spectral interference pattern by noting that each peak of the fringe pattern implies a phase increase of 2π . The group velocity dispersion (GVD), $\frac{\partial^2\beta}{\partial\omega^2}$ is then calculated by making a suitable polynomial fit to the found phase and deriving it twice:

$$\beta_2(\omega) \equiv \frac{\partial^2\beta(\omega)}{\partial\omega^2} = \frac{1}{2L} \left[\frac{\partial^2\phi(\omega)}{\partial\omega^2} - \frac{\partial^2\phi_0(\omega)}{\partial\omega^2} \right] \quad (6.3)$$

The GVD from the components of the setup, $\frac{\partial^2\phi_0(\omega)}{\partial\omega^2}$ is easily removed by making a background measurement without a test fiber inserted. As before the phase is reconstructed and a polynomial fit is used to calculate the second derivative now given by

$$\frac{\partial^2\phi(\omega)}{\partial\omega^2} = \frac{\partial^2\phi_0(\omega)}{\partial\omega^2} \quad (6.4)$$

Subtracting this from the previously found value gives the GVD originating from the fiber under test and thereby the dispersion

$$D(\omega) = \frac{-2\pi c}{\lambda^2} \beta_2(\omega) \quad (6.5)$$

6.4 Example - HC 1060-02 air guiding fiber

To illustrate how the calculations are made, an example based on a PBG fiber from Blaze Photonics (now Crystal Fibre) is presented below. Figure 6.2 (left) shows a typical spectrum at near-temporal overlap of the fields in the two arms. An interference pattern is clearly seen and a zoom reveals smooth regular oscil-

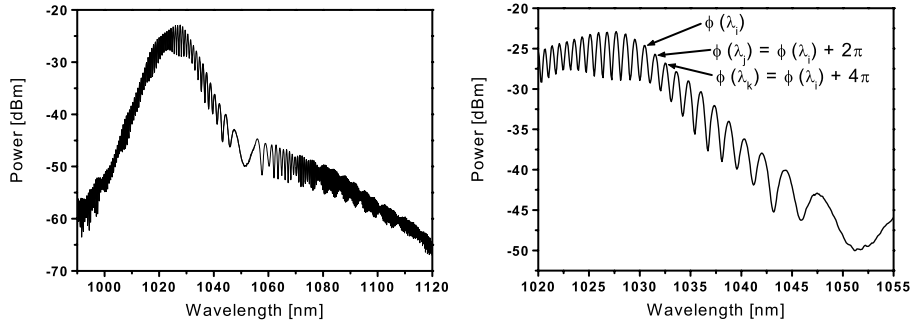


Figure 6.2: Left: Measured spectrum when the fields are temporally overlapped. The position of exact temporal overlap is found around 1050 nm where the slow modulation reveals that the linear term in eq. 6.2 is small or zero. Right: Zoom on the region around 1035 nm. The fringes are well resolved and the phase is easily constructed by adding 2π at each local maximum.

lations as illustrated in the right panel. The phase, $\phi(\omega)$, is easily constructed by adding 2π at each oscillation peak. Figure 6.3 (left) shows the resulting spectral phase. Note that the curve has a turning point at which the phase starts to decrease. The location of this point coincides with the slow modulation near 1050 nm in figure 6.2 (left), which is roughly the point of temporal overlap for just that wavelength region. This can be understood by noting that the linear term in eq. 6.2 is small when the two signals are nearly overlapped in time. The turning point can therefore be shifted by changing the length of the reference arm, and it is advantageous to position it in the middle of the spectrum to have resolved fringes over a wide range.

When the phase is known, a suitable polynomial fit to the data is made. Figure 6.3 (right) shows how 4th and 7th order polynomials can be used to accurately represent the data. The chosen polynomial is then derived twice

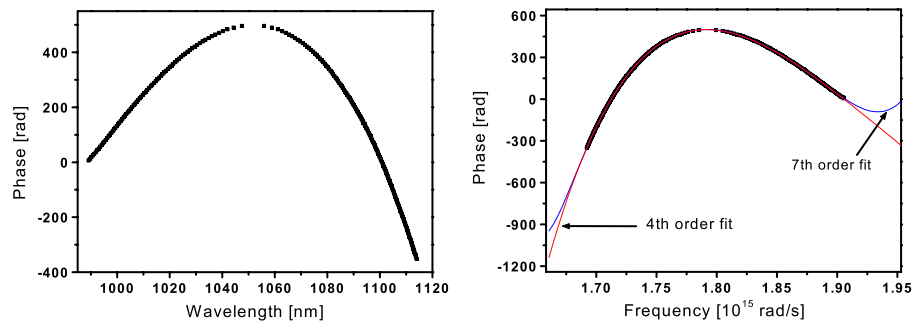


Figure 6.3: Left: Phase versus wavelength as determined from the measurement shown in figure 6.4. Right: Same data but plotted against frequency. Two polynomial fits of order 4 and 7 are shown. While both fits represent the data well, the curvature of the functions are clearly different at the edges of the data-set.

to give $\beta_2(\omega)$ and thereby the dispersion (as shown in figure 6.4). Note that the resulting dispersion is sensitive to the order of the polynomial fit. While polynomials of different orders can make equally good fits to the phase, the second derivative may change significantly with the order. As a result, the dispersion is accurately determined only in the middle of the data-set where the curvature of the fit is set by the data points and not by the choice of polynomial. Figure 6.4 indicates that this particular measurement is reliable in the interval

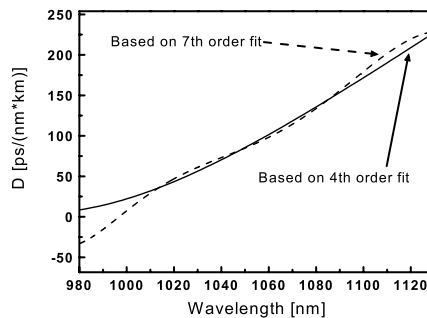


Figure 6.4: The calculated dispersion for the two polynomial fits shown in figure 6.3. The curves are almost coinciding in the middle of the interval while they differ significantly at the edges.

1010-1090 nm and comparison with measurements made by Blaze Photonics [91] confirms the dispersion in this interval.

The setup was also tested by measuring the dispersion of well-known fibers

such as HI-1060 Flexcore [92] and SMF28 [93] and in both cases excellent agreement with known values were found.

Figure 6.4 illustrates how the choice of the polynomial order can influence the calculated dispersion, especially in the edges of the measured wavelength range. To improve accuracy and extend the measurable wavelength region, the Yb-based ASE source is replaced with Koheras' SuperK whitelight source which has a bandwidth from 600-1700 nm [94]. However, the effective bandwidth of the setup is limited by the 50/50 coupler which has a bandwidth of 300 nm centered at 1050 nm. Although limited, this spectral range is of special interest since the development of Yb-based femtosecond oscillators requires accurate determination of the dispersion in the involved fiber components.

Figure 6.5 (left) shows a background measurement made with the SuperK whitelight source (black curve) and a transmission curve for a newly developed solid core PBG fiber. The bandwidth of the setup clearly stretches beyond 300 nm while the transmission window of the fiber is only roughly 200 nm (marked with dashed lines). An insert in figure 6.5 (right) shows a microscope image of

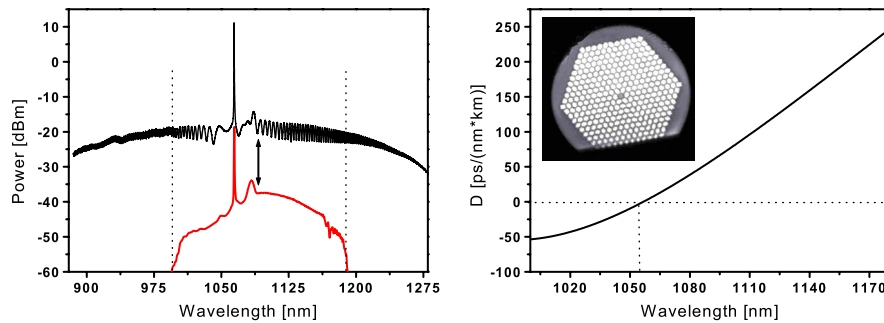


Figure 6.5: Left: Background spectral measurement indicates the bandwidth of the setup (black). A transmission curve of the fiber reveals a bandgap from ~ 1000 - 1180 nm (red) - the curve has been lowered 20 dBm for the illustration. Right: Dispersion as function of wavelength. The parameters were obtained from a 5th order polynomial fit of the measured phase. Insert shows a microscope image of the solid core PBG fiber. Guiding is ensured by surrounding the silica core with Germanium doped, high index 'rods'. Picture provided by Crystal Fibre.

this fiber which, in contrast to "traditional" PBG fibers, does not rely on air holes to trap the light in the core. The bandgap effect is obtained by surrounding a silica core with Germanium doped high index 'rods' which act as anti-resonant defects. This type of fiber is highly interesting for dispersion compensation in cavities since the absence of air holes allows it to be spliced to standard fiber

components [95]. The obtained fiber dispersion is shown in the right panel of figure 6.5.

6.5 Summary

Fiber dispersion is a critical parameter when working with ultrashort pulses and careful characterization is necessary if nonlinear devices or laser oscillators are based on fiber components. Through spectral analysis of the output from a simple Michelson-interferometer, the dispersion in a test fiber can be extrapolated by simple calculations. By implementing a PCF-based white light source, accuracy as well as bandwidth are enhanced and characterization in the important Yb-window is possible. The setup has been used to characterize various types of fiber and is now routinely used at NKT-Research.

Chapter 7

Dual-wavelength pumping of photonic crystal fibers

Two-pump super continuum generation in PCFs is described and the dual-pumping scheme is shown to increase the spectral bandwidth in the visible. A similar setup is used in the SuperK whitelight source from Koheras, so proper understanding of the process is useful for further development of this type of light source.

7.1 Introduction

Usually SCG in microstructured fibers has been obtained by pumping the fiber in the anomalous dispersion regime where fission of solitons provides a wide spectrum through SPM, Raman-scattering and FWM. The fission of a higher order soliton into its constituent fundamental solitons also gives rise to growth of dispersive waves which are often found deep in the visible [2]. However, it was recently reported that extraordinary wide and flat spectra could be obtained in the visible by simultaneously pumping a PCF in the normal and anomalous regime with picosecond pulses [96]. By co-propagating the second harmonic (SH) at 532 nm and the fundamental at 1064 nm it was found that the discrete Raman lines in the visible were smoothed out, resulting in a flat spectrum centered at 532 nm. This was believed to originate from an arrest of stimulated Raman scattering (SRS) due to a four wave mixing (FWM) process which, in case of phasematching, has higher gain [12]. The demonstration of a broadband visible light source with a simple setup, spurred interest in dual-wavelength pumping of photonic crystal fibers and it was later suggested that co-propagating two femtosecond pulses could lead to significant spectral broadening of the SH pulse due to cross phase modulation (XPM) imposed by fundamental solitons [36]. Simulations showed that a co-propagating SH pulse at 450 nm could be broadened with more than 100 nm in this way. In this chapter, it is demonstrated experimentally that femtosecond dual pumping indeed leads to a spectral broadening of the co-propagating SH pulse due to cross phase modulation.

7.2 Experimental setup

The experimental setup is shown in figure 7.1. A Yb:KGW oscillator is delivering 1028 nm, transform-limited 380 femtosecond pulses at a repetition rate of 9.8 MHz and a pulse energy up to 250 nJ. The pulses are frequency doubled in a 17 mm long LBO (Lithium Triborate) crystal with an efficiency of up to 60%. The fundamental and second harmonic beams are then separated with a dichroic mirror reflecting 1028 nm and transmitting 514 nm. Each beam is re-collimated and sent through appropriate telescopes in order to ensure proper mode matching at the position of the fiber tip. The IR beam is sent through a delay stage before it is recombined with the SH and coupled into 35 cm of the PCF. Using a regular aspheric lens (C230TM from Thorlabs) with a focal length of 4.5 mm it is possible to get approximately 30 % of both colors through the fiber simultaneously. After the fiber, an achromatic microscope objective collimates the super continuum.

The fiber is birefringent and half-wave plates are used to ensure that both beams are coupled into the main axis of the fiber. Temporal overlap is conveniently found by monitoring the spectrum diffracted off a grating onto a white

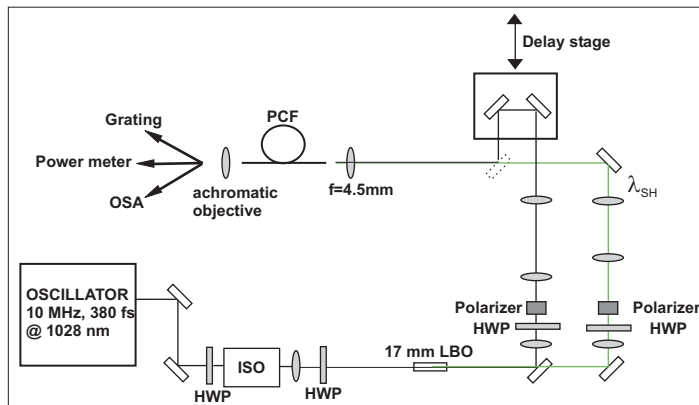


Figure 7.1: Experimental setup. ISO: Optical isolator, HWP: Half-plate, LBO: Lithium Triborate crystal, PCF: Photonic crystal fiber, OSA: Optical spectrum analyzer.

surface while scanning the delay stage. When the pulses overlap in the fiber, intense visible components appear in the spectrum. Depending on the position of the stage, red or blue frequency components can be emphasized as illustrated in figure 7.2

7.3 Results

Figure 7.2 shows the dramatic effect of launching two pulses into the PCF. Red curves show the spectrum of the fundamental IR pulse in absence of the SH pulse, green curves show the 514 nm pulse alone and black curves show the result of the interaction of two pulses. In the left figure, the temporal overlap is adjusted to optimize the blue part of the spectrum while the red part is optimized in the right figure. In both figures, the fundamental pulse alone causes a broad spectrum in the infrared due to SRS and also weak NSR around 420 nm. When the SH pulse is launched into the fiber, the visible part of the spectrum is shifted almost 100 nm towards the blue (left figure). In the right figure, the 514 nm pulse is redshifted and the visible part of the spectrum almost merges with the NIR part. Figure 7.3 shows the spectral evolution as function of IR input power in more detail. The visible pump power is kept constant at 6 mW (0.67 nJ) and the IR power is gradually increased but kept below the threshold for emission of NSR in order to highlight the effect of the dual pumping. The left figure shows how increased IR power leads to red-shifting of the soliton and finally emergence of several fundamental solitons. In figure 7.3 (right) a significant blue-shift is observed with increasing pump power. Integration

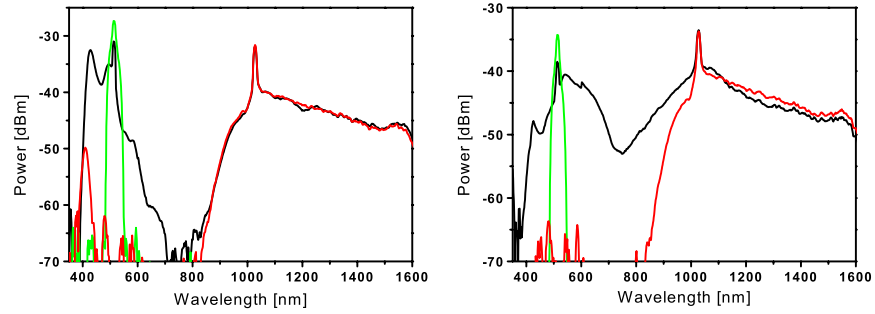


Figure 7.2: Black curve shows the enhancement of the blue (left) and red side (right) of the XPM shifted SH signal. Green and red curves represent the isolated SH and fundamental signals respectively. In both figures the IR pump power is 20 mW and the SH power is 12 mW.

of the spectra shows energy conservation in the spectral range 350 nm - 650 nm, so there is not energy transfer between pulses. This indicates that the underlying mechanism is XPM. Numerical simulations based on the extended nonlinear Schrödinger equation confirm the energy conservation in the visible and clearly show how fundamental solitons pass through the visible pulse and cause XPM-shifts. The enhanced blueshift of the visible pulse with increasing

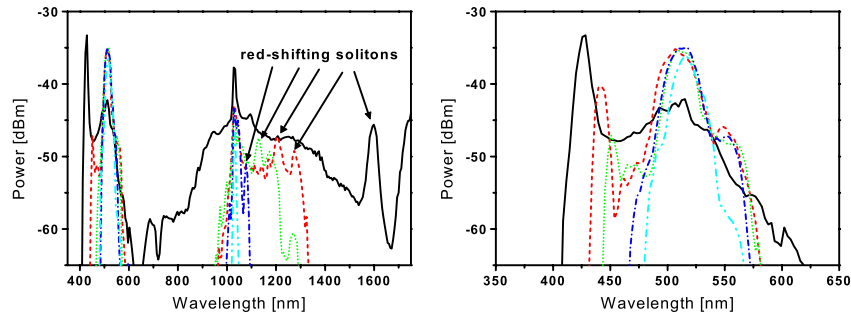


Figure 7.3: Left: Spectral evolution as function of increasing IR power. Maximum IR power is 18 mW and the green power is constant at 6 mW. Right: Same evolution in the spectral range close to the SH pump. Cascaded XPM leads to a large blue-shift of the green pulse.

IR pump power is a result of increased peak power of the first fundamental soliton (eq. 2.35). At higher IR powers, the interaction becomes complicated as more solitons are formed and may overlap with the SH pulse.

The physical origin of XPM is a change of the refractive index induced by a

co-propagating optical pulse. XPM thus induces a frequency chirp given by [97]

$$\partial\omega = -2\gamma \frac{\partial}{\partial T} |A(z, T)|^2 \cdot dz \quad (7.1)$$

where dz is the effective interaction length. Equation 7.1 shows that the trailing edge of an intense pulse will cause a blueshift of the co-propagating pulse while the leading edge will cause a redshift. A soliton is a symmetric pulse so if a solution walks through another pulse its spectrum will be unchanged since each side of the soliton imposes equal but opposite phaseshifts. However, if dispersion is present, the group velocity mismatch between the soliton and the XPM-shifted wavelength may cause them to separate temporally and thereby prevent the cancelling shift from the opposite side of the soliton. The result is a permanent XPM-shift - even if the soliton walk-through is complete [97]. Figure 7.4 shows four frames from a simulation where a fundamental soliton passes through the visible pulse. In the second frame the leading edge of the soliton has caused a

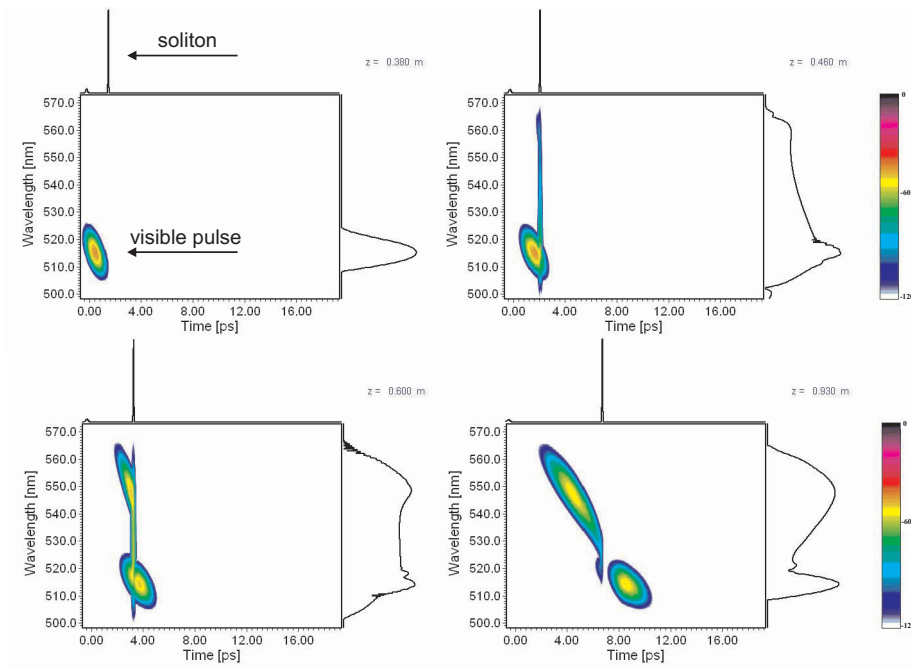


Figure 7.4: Simulation showing a soliton passing through the SH pulse. The leading edge of the soliton causes a redshift which is only partially compensated by the trailing edge because the red components walk away from the soliton. The simulation is made with a 150 fs, 0.1 nJ IR pulse and a 100 fJ, 300 fs green pulse and a relative delay of 5 ps. Time is relative to the pump at 1030 nm.

redshift of more than 50 nm. In the third and fourth frame, the trailing edge of the soliton blueshifts the previously redshifted components back again but, because of dispersion, some of the red intensity separates from the soliton and does not get shifted back. The result is a permanent red-shift.

Figure 7.5 (left) shows experimentally obtained spectra of the IR pulse as function of IR power after propagation through 4.3 m of the PCF. The spectra

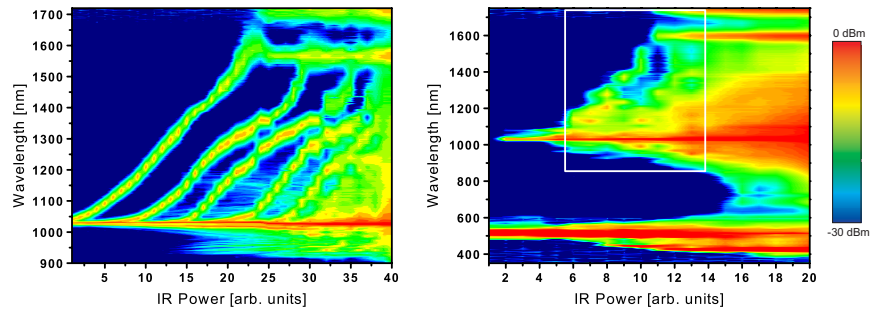


Figure 7.5: Left: Experimental spectral evolution with increasing power of the IR pulse. Right: Same evolution but with two pump wavelengths. The onset of significant blue-shifting of the SH pulse coincides with a red-shift of the first fundamental soliton to approximately 1200 nm. At this wavelength, the soliton has the same group velocity as the SH pulse - see figure 7.6. Green power is kept constant at 6 mW and the IR power is gradually increased up to 15 mW.

are shown for each IR power level and the figure clearly shows how isolated fundamental solitons are emitted and red-shifted as the input power is increased. Firstly, one soliton is formed and shifts towards the infrared. At higher power (spectrum ~ 10), a second soliton is emitted and so forth. Figure 7.5 (right) shows the same evolution but with the additional SH pulse launched into the fiber. A white box highlights the measurement shown in the left figure. The power of the green pulses is kept constant at a low power of 6 mW. No changes in the infrared spectra are observed due to the green pump pulse. In contrast, the spectrum of the 514 nm pulse is influenced significantly. After the first soliton is emitted, the spectrum of the green pulse starts to extend to the blue ("8" on power axis). At the highest IR power, the cascaded action of several solitons results in a maximum blue shift down to approximately 420 nm.

Figure 7.6 shows the dispersion and the group delay relative to 1028 nm for the fiber under investigation. The relative group delay increases when the solitons redshift (they slow down), causing their group velocity to approach the group velocity of the SH pulse. This explains the size of the observed XPM-shifts - the enhanced temporal overlap increases the effective interaction length. The

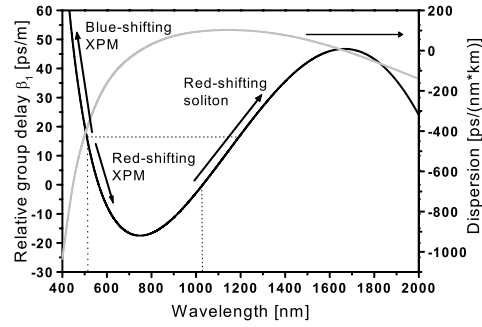


Figure 7.6: Calculated group delay relative to 1028 nm (black) and dispersion (gray). Red-shifting solitons slows down and are eventually caught by the SH pulse. With an appropriate temporal overlap between pulses, cascaded XPM can take place.

step slope of the curve in the visible implies a large group velocity mismatch between the soliton and XPM-shifted components and the resulting walk-off is responsible for the permanent frequency shift.

Since the results above apparently can be understood by simple analysis of the group delay curve, it is interesting to repeat the experiment with another fiber. Figure 7.7 shows the dispersion and group delay relative to 1028 nm for the widely used NL-PM-750 (from Crystal Fibre). Comparison with figure 7.6

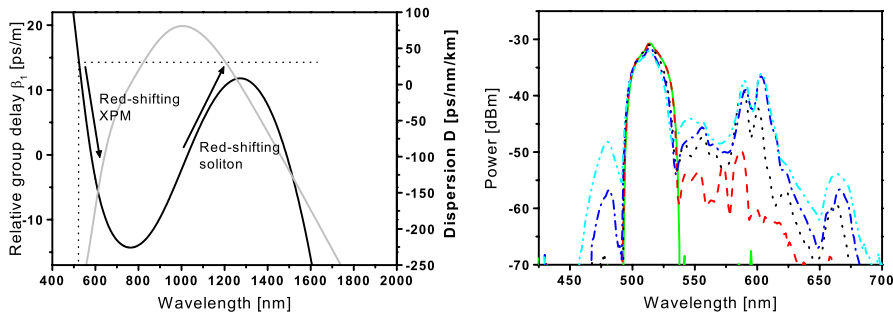


Figure 7.7: Left: Calculated group delays with respect to 1028 nm (black) and dispersion (gray). The red-shifting solitons are always faster than the SH pulse. Right: Measured spectral broadening in the visible as the IR power is increased. Regardless of the chosen delay it is not possible to induce a blue-shift. The blue peak at approximately 480 nm is NSR.

reveals an important difference between the group delays in the two fibers. In NL-PM-750 it is not possible for a red-shifting soliton to obtain the same group

velocity as the SH pulse at 514 nm and the size of the XPM shift is therefore expected to be smaller than in the previous fiber. The soliton is always faster than the SH pulse so it is not possible to make the trailing edge of the soliton blue-shift the SH pulse. However, by delaying the soliton with respect to the SH pulse, it is possible for the faster soliton to catch up and walk through the visible pulse. Group velocity mismatch then allows red-shifted components to escape from the soliton, leaving a permanent red-shift. Figure 7.7 (right) shows spectra obtained by femtosecond pumping of the fiber, which illustrates this point. Regardless of IR power and choice of delay, it is not possible to blueshift the visible pulse. The blue peak at 485 nm is emerging NSR, which grows as the soliton number increases.

In conclusion, the outcome of the dual-wavelength pumping experiment can be understood by analyzing the group delay curve. The critical parameter is the group velocity mismatch between the XPM shifted components and the interacting soliton. For a given set of pump wavelengths, it is thus possible to calculate the obtainable frequency shift solely from the group velocity curve [3]. Therefore new light sources can be developed by a proper choice of pump wavelengths and suitable design of the fiber dispersion.

7.4 Picosecond dual-wavelength pumping

Similar experiments with picosecond pulses have been made by Carsten Thomsen from NKT-Research. A fiber oscillator, delivering 5 picosecond pulses at 1060 nm at a repetition rate of 80 MHz, was used to drive a setup like the one presented in figure 7.1. The results are remarkably similar to the ones obtained by femtosecond pumping as seen by comparison of figure 7.8 and figure 7.3 (same fiber). Again, integration of spectra and numerical simulations show that there is no energy transfer from the IR to the visible. The blue-shifted components in figure 7.8 originate from the SH pulse and are merely spectrally shifted by the IR pulse. It has previously been shown that picosecond pulses, as well as nanosecond pulses, break up into very short pulses due to modulation instabilities in presence of negative GVD [98, 99]. The short pulses subsequently form solitons, which then evolve as described in the previous section. So, although other nonlinear effects such as FWM and SRS may contribute to the spectral broadening [96], the governing mechanism is still soliton fission and soliton XPM. In comparison to the femtosecond scenario the only important difference is the number of solitons created. As the soliton number scales with the pulse duration, a picosecond pulse will split into a much higher number of solitons. This implies a complicated interaction with the SH pulse as there will be many XPM-shifts from several solitons. This explains the improved flatness of the spectra in figure 7.8 compared to the spectra shown in figure 7.3. It should be noted that the spectra in figure 7.8 also contains a contribution at

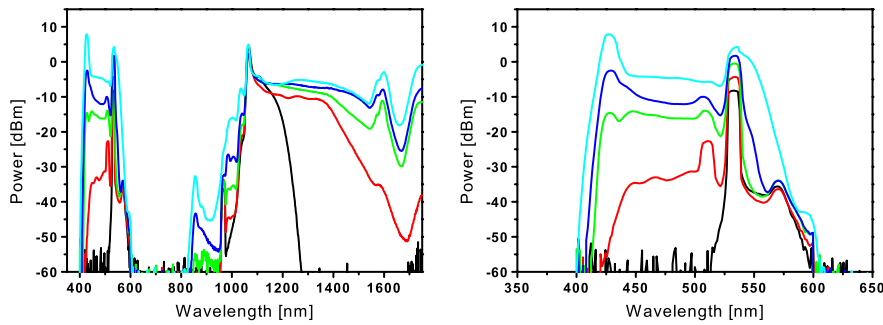


Figure 7.8: Left: Spectral evolution for increasing power. Right: Zoom on the visible part of the spectrum. Cascaded XPM leads to a significant blue-shift of the green part of the pulse. The increased flatness in the visible is attributed to an increased number of solitons, each imposing XPM on the visible pulse. Data provided by Carsten Thomsen.

420 nm from NSR. The presence of NSR shows that soliton fission is indeed taking place.

7.5 Nanosecond dual-wavelength pumping

Considering the results presented above, it is not surprising that nanosecond pumping of the fiber leads to similar results as for femtosecond and picosecond pumping. A nanosecond pulse launched in the anomalous regime will break up into short pulses due to modulation instabilities and (many) solitons will be created. As before, the XPM interaction of the SH and the fundamental solitons cause a frequency shift of the SH pulse and create a continuum with high spectral density in the blue part of the spectrum. The resulting spectra of such an experiment are shown in figure 7.9. The similarity with the previous results indicates that soliton dynamics play a key role, and the flat spectrum and merging of discrete Raman lines can be explained by the XPM induced shifts imposed by numerous solitons. Again, the presence of NSR indicates that soliton fission is taking place, which further validates this suggestion.

The use of nanosecond pump pulses is highly attractive from a practical point of view as it enables use of compact microchip pump sources. Passive Q-switching of such lasers has been shown to enable few-nanosecond pulses with peak powers in the kW range. Dual-pump setups can thus be made in extremely compact form employing relatively simple components and such a setup is the basis of the SuperK-Blue white-light source from Koheras [94]. The drawback of nanosecond pumping is the relatively high pulse energies which can cause damage to the fiber. As a consequence, the average power is limited to about

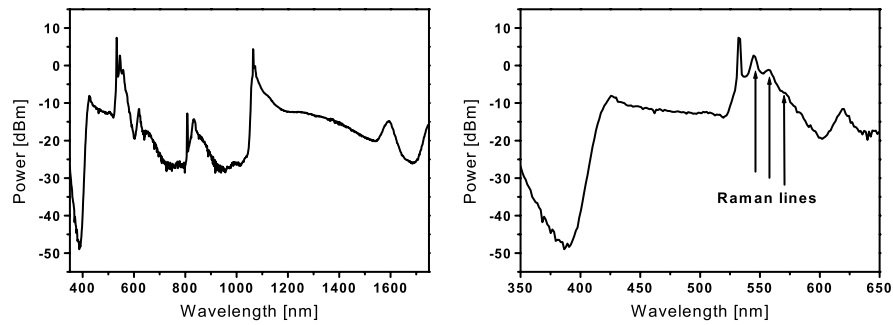


Figure 7.9: Left: Spectrum from nanosecond dual-wavelength pumping. The sharp feature at 808 nm is residual pump from the microchip cavity. Right: A flat plateau extends from 420 nm to 540 nm. The bumps to the right of the 530 nm pump are 13.2 THz shifted Raman-peaks. Curves provided by Yujun Qian, NKT-Research

50 mW. High repetition rate picosecond or femtosecond pumping would remove this constraint and allow higher average power. The price is however added complexity of the setups.

7.6 Summary

Dual-wavelength pumping of PCFs has shown to enable broadband bright light sources with high spectral density in the visible. Experiments with femtosecond pulses, in combination with numerical simulations, show that the governing mechanism is XPM of the visible pulse imposed by fundamental solitons. The group velocity mismatch between XPM-shifted components and red-shifting solitons cause temporal walk-off and thereby a permanent XPM-shift in spite of full walk-through of the soliton. Dual-pump experiments with picosecond and nanosecond pulses gave similar results as the ones obtained with femtosecond pumping. It is well known that modulation instabilities cause longer pump pulses to break up into shorter pulses which evolve into solitons so the only difference between the three pumping regimes is actually the number of interacting solitons.

The use of dual-wavelength pumping of PCFs has enabled novel picosecond and nanosecond white-light sources and has already led to the commercially available SuperK whitelight source. Since the effect of dual-wavelength pumping is governed by the choice of pump wavelengths and the group delays in the used fiber, it is fairly straight-forward to extend the accessible wavelength range. Existing and coming products of this type will certainly find applications in spectroscopy, tomography and bio-imaging.

Chapter 8

Fiber laser pumped optical parametric amplifier

Optical parametric amplification of a super continuum from a PCF enables a high power tunable femtosecond source in the visible and near infrared. The large bandwidth of the seed, as well as the amplifier, is used to generate sub-50 fs pulses and simulations indicate that it may be possible to obtain pulse durations below 20 fs. The setup is power scalable and represents an interesting route towards compact high power ultra-fast laser systems.

In summer 2005 I visited the fiber laser group in Jena to carry out experiments with optical parametric amplification (OPA). Fiber lasers are ideal pump sources for OPA and I made a fiber laser pumped OPA based on the idea from chapter 3 of amplifying a super continuum from a PCF. The first attempt had failed due to limited pump power but, with access to almost unlimited pump power in Jena, that was no longer a limitation. The following pages describe the resulting high power fiber laser pumped femtosecond source and the experiments with ultra-short pulse amplification.

8.1 Introduction

Sources of tunable ultrashort laser pulses are essential tools for probing fast phenomena in physics, chemistry and biology. Kerr-lens modelocked Ti:Sapphire lasers [42] have proven to be very reliable sources of femtosecond pulses and "turn-key" devices supplying sub-20 fs are now commercially available [100]. However, in spite of the outstanding performance of these lasers, the tunability is restricted to the region around 800 nm and the second harmonic around 400 nm. The limited tuning range can be greatly expanded through OPA, which has become a widely used technique [101]. In OPA, coupling of three waves via the nonlinear polarization enables photons from the intense pump wave to be efficiently converted into (lower energy) signal photons and the same number of idler photons. Such a scheme requires fulfilled energy and momentum conservation, also termed as phase-matching, determining the interacting wavelengths and, in particular, the tunability and bandwidth of the parametric amplification.

It has been demonstrated that waiving of traditional collinear pumping geometry leads to a significant increase of the phase-matched bandwidth which can be obtained in OPA [102]. As a result, ultrashort laser pulses are now routinely generated throughout the visible and near infrared spectral region with high efficiency employing non-collinear optical parametric amplifiers (NOPAs) [50, 101, 103].

A typical NOPA is driven by an amplified Ti:Sapphire laser system delivering 100-200 fs pulses with energies up to a few mJ. The high pulse energy and resulting peak power ensure highly efficient nonlinear conversion in the OPA stages, and several tens of μJ can usually be obtained across the desired wavelength range [101]. However, the average power from the Ti:Sapphire systems is limited by the thermal load on the gain crystal as thermal lensing deteriorates the beam quality. Without special precautions, the available pump power is therefore of the order of a few Watts [104]. In contrast, the parametric amplification itself does not suffer from thermal effects. The fulfilled energy conservation and high optical quality of the nonlinear crystals ensure minimal heating of the crystal. For that reason parametric amplification is well suited

for high repetition-rate and high average power applications.

In this context, fiber lasers and amplifiers represent an interesting alternative to the conventional Ti:Sapphire-based systems since they can supply high average powers as well as high pulse energies [9]. Due to excellent heat dissipation and strong confinement of the light in fibers, diffraction limited beam quality can be obtained even with continuous wave powers well above 1 kW [67]. Additionally, the high optical conversion efficiencies (up to 80%) from low-brightness laser pump diodes [105] enable a great reduction in price as well as complexity of such systems. Short-pulse fiber lasers are therefore predestinated pump sources for high repetition rate parametric amplifiers.

In this chapter, the implementation of a 1 MHz repetition rate parametric amplifier pumped by a chirped pulse fiber amplification system is described. The setup is based on a single pass fiber amplifier and yet femtosecond pulses with energies above 1 μJ can be obtained and tunability in the range < 700 nm to > 1500 nm has been observed. A broadband signal generated in a PCF provides a reliable and nearly flat supercontinuum which is an ideal seed for OPA when tunability is desired. Additionally, short pulse generation is demonstrated. By reducing the power in the PCF, soliton fission is avoided and the amplified spectrum is compressed to sub-40 fs pulses. Simulations indicate that pulse durations as low as 20 fs are feasible.

8.2 Theory of optical parametric amplification

OPA is a $\chi^{(2)}$ process in which a high intensity beam (pump) amplifies a weak signal and generates a third wave, an idler, in the process. Quantum mechanically, a pump photon is divided into lower energy signal and idler photons under energy and momentum conservation (phasematching)

$$\hbar\omega_p = \hbar\omega_s + \hbar\omega_i, \quad \hbar\mathbf{k}_p = \hbar\mathbf{k}_s + \hbar\mathbf{k}_i \quad (8.1)$$

Assuming $\chi^{(2)} \gg \chi^{(3)}$, the nonlinear polarization is approximated by $P_{nl} \approx \chi^{(2)}\mathbf{E}\mathbf{E}$. The electric field can be represented by a sum of three pulses with central frequencies $\omega_p, \omega_s, \omega_i$

$$E(\mathbf{r}, t) = F(x, y) \sum_{n=p,s,i} A_n(z, t) \exp(ik_n z - i\omega_n t) + c.c. \quad (8.2)$$

where $F(x, y)$ is the frequency independent transverse area and A_n is the slowly varying envelope. Choosing the polarization terms oscillating at $\omega_p, \omega_s, \omega_i$, the wave equation (eq. 2.9) can be solved for each frequency component to give the following set of equations for the slowly varying amplitudes of pump, signal and

idler respectively ($j = \sqrt{-1}$ is used to avoid confusion with the idler index i)

$$\frac{\partial A_p}{\partial z} + \frac{1}{v_{g,p}} \frac{\partial A_p}{\partial t} = -j \frac{\omega_p d_{eff}}{n_p c} A_i A_s \exp(j\Delta kz) \quad (8.3)$$

$$\frac{\partial A_s}{\partial z} + \frac{1}{v_{g,s}} \frac{\partial A_s}{\partial t} = -j \frac{\omega_s d_{eff}}{n_s c} A_i^* A_p \exp(-j\Delta kz) \quad (8.4)$$

$$\frac{\partial A_i}{\partial z} + \frac{1}{v_{g,i}} \frac{\partial A_i}{\partial t} = -j \frac{\omega_i d_{eff}}{n_i c} A_s^* A_p \exp(-j\Delta kz) \quad (8.5)$$

where v_g is the group velocity for the pulses, d_{eff} is the effective nonlinear coefficient and $\Delta k = k_p - k_s - k_i$. Dispersion has been neglected which is a reasonable approximation since the pulses in these experiments are longer than 100 fs. Equations 8.3-8.5 can be solved numerically but with a few approximations, an analytical solution can be derived as well: Assuming negligible difference in group velocity the equations reduce to

$$\frac{\partial A_p}{\partial z} = -j \frac{\omega_p d_{eff}}{n_p c} A_s^* A_i \exp(j\Delta kz) \quad (8.6)$$

$$\frac{\partial A_{s,i}}{\partial z} = -j \frac{\omega_{s,i} d_{eff}}{n_{s,i} c} A_{i,s}^* A_p \exp(-j\Delta kz) \quad (8.7)$$

This approximation is valid for long pulses for which a small temporal walk-off does not change the amplitudes significantly. Section 8.2.1 will show how group velocity matching can be obtained even with ultrashort pulses by applying a non-collinear geometry between the beams. Furthermore, assuming phasematching and un-depleted pump, the equations can be simplified to

$$\begin{aligned} \frac{\partial A_p}{\partial z} &= 0 \\ \frac{\partial A_{s,i}}{\partial z} &= -j \frac{\omega_{s,i} d_{eff}}{n_{s,i} c} A_{i,s}^* A_p \end{aligned} \quad (8.8)$$

which are readily de-coupled to show that the intensity of the signal and idler grows exponentially with pump power and the interaction length. In practice, gains of the order of $10^3 - 10^6$ can be obtained in short (1-5 mm) nonlinear crystals [101].

Apart from the huge gain, OPA has another important quality which becomes apparent when eq. 8.6-8.7 are solved for the phase of the amplitude. Assuming $A_{s,i} = |A_{s,i}| \exp(j \phi_{s,i})$ the following solutions for the phase of the signal and idler can be found [106-108]

$$\phi_s(z) = \phi_s(0) - \frac{\Delta kz}{2} + \frac{\Delta kz}{2} \cdot K \quad (8.9)$$

$$\phi_i(z) = \phi_p(0) - \phi_s(0) - \frac{\Delta kz}{2} - \frac{\pi}{2} \quad (8.10)$$

where K is a constant depending on the degree of pump depletion. Until now, signal and idler have been treated equally but, with the phases above, it is understood that a seed is present at the signal wavelength while the idler grows from noise. The result shows that the phase of the signal beam is preserved in case of phasematching, and just shifted with a constant if $\Delta k \neq 0$. In contrast, the phase of the idler depends on the phase of the pump and the signal. Physically, the idler power is generated from noise and the waves with the 'right' phase are coherently amplified. In other words, the idler phase self-adjusts to ensure phasematching and in the process, it compensates for whatever phase the pump and signal might have. The signal pulse is therefore amplified without any phase distortion even if the pump pulse has spatial or temporal chirps. Section 8.5 will describe experiments with broadband amplification of ultrashort pulses and shows how high quality signal phase is maintained in the amplification process, leading to ultrashort high power pulses.

8.2.1 Non-collinear optical parametric amplification

As mentioned before, a non-collinear geometry of the signal and pump beams leads to increased phasematched bandwidth [102]. This is easily understood by simple geometric considerations illustrated in figure 8.1. The phase mismatch

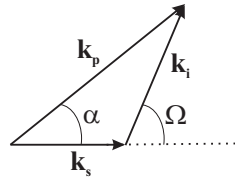


Figure 8.1: When overlapping pump and signal at an angle the resulting idler is emitted such that phasematching is fulfilled. Broadband phasematching is obtained when signal and idler have the same 'horizontal' group velocity.

can be divided into components parallel and orthogonal to the signal wave vector k_s

$$\Delta k_{\parallel} = k_p \cos \alpha - k_s - k_i \cos \Omega \quad (8.11)$$

$$\Delta k_{\perp} = k_p \sin \alpha - k_i \sin \Omega \quad (8.12)$$

where α is the angle between the signal and the pump beam and Ω is the angle between signal and idler beams. Ω depends on frequency and it is therefore interesting to look at the phase mismatch as function of a (small) change in

frequency. The phase mismatch can then be estimated by

$$\Delta k_{\parallel} \approx \frac{\partial k_s}{\partial \omega_s} \Delta \omega + \frac{\partial k_i}{\partial \omega_i} \cos \Omega \Delta \omega - k_i \sin \Omega \frac{\partial \Omega}{\partial \omega_i} \Delta \omega \quad (8.13)$$

$$\Delta k_{\perp} \approx \frac{\partial k_i}{\partial \omega_i} \sin \Omega \Delta \omega + k_i \cos \Omega \frac{\partial \Omega}{\partial \omega_i} \Delta \omega \quad (8.14)$$

For broadband phasematching, $\Delta k = 0$ over a wide range of frequencies so both equations must equal zero. By multiplying eq. 8.13 with $\cos \Omega$ and eq. 8.14 with $\sin \Omega$ and adding the two, the following equations are obtained

$$\frac{\partial k_i}{\partial \omega_i} - \cos \Omega \frac{\partial k_s}{\partial \omega_s} = 0 \quad \iff \quad v_{g,s} = v_{g,i} \cos \Omega \quad (8.15)$$

which show that broadband phasematching is obtained when Ω is chosen such that the projection of the idler group velocity matches the group velocity of the signal. In practice, α is the controllable angle so, by choosing the right angle between the pump and signal beams, it is possible to obtain broadband phasematching *and* match the group velocities at the same time. This is very fortunate from an experimental point of view as both effects greatly increase the efficiency of the OPA process and enable amplification of ultrashort pulses. Figure 8.2 shows phasematching curves for different angles α , between a 514 nm pump beam and the signal beam. The curves are made with the freely available SNLO software [109] and show that an internal angle of $\alpha = 2.6^\circ$ between the pump and signal beams results in broadband phasematching over roughly 200 nm. The large achievable phase-matching bandwidth enables amplification of

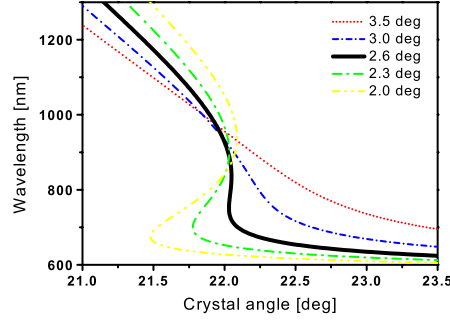


Figure 8.2: Calculated phasematching curves for different angles between pump and signal (internal angle). The 'magic' angle 2.6° results in phasematching over more than 200 nm and simultaneously matches the group velocities.

ultrashort laser pulses and few-cycle pulses have been realized from the UV to the NIR [50, 110, 111]. Such pulses are interesting for directly probing very fast

phenomena but also for high-order harmonic generation resulting in ultrashort soft X-ray pulses [112].

Short, high power pulses can also be obtained directly from fiber and bulk amplifiers, but the performance is limited by either temporal (self phase modulation) or spatial (thermal lensing) distortion of the phase, which makes recompression to ultra-short pulse durations (sub-10 fs) impossible. Parametric amplification is therefore superior for short pulse amplification and the combination of fiber lasers and OPA is especially attractive due to the scalability of both concepts.

8.3 Experimental setup

The high repetition rate tunable femtosecond source consists of a single stage parametric amplifier pumped by a frequency doubled Yb-doped fiber based chirped pulse amplification system. The seed is provided by a super continuum generated in a PCF. The experimental setup is shown in figure 8.3. An Yb:KGW

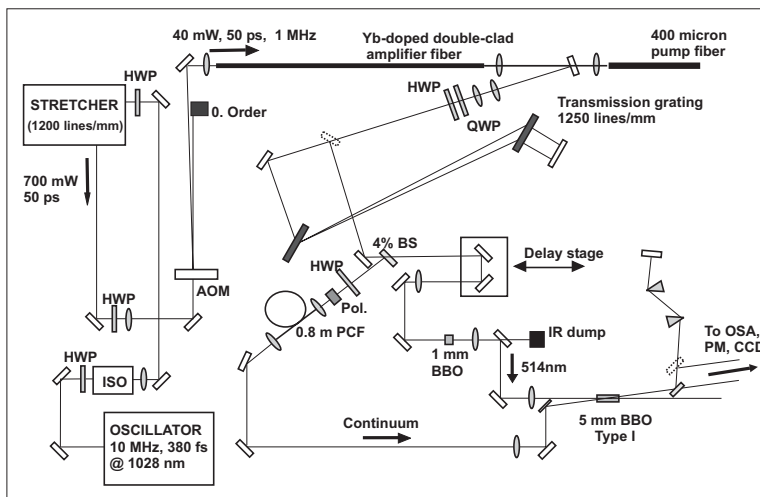


Figure 8.3: Experimental setup. ISO: optical isolator, HWP: half-wave plate, QWP: quarter-wave plate, AOM: acousto-optic modulator, BS: beam splitter, OSA: optical spectrum analyzer, PM: power meter.

oscillator (Amplitude Systemes tpulse 200) delivering transform-limited 380 fs, sech^2 pulses at a repetition rate of 9.8 MHz at 1028 nm is used to seed a fiber amplifier consisting of 1.2 meters of a large mode area double clad Ytterbium-doped PCF [113]. The fiber has a 40 μm core and is intrinsically single-mode

with a NA of 0.03 at 1030 nm. The extremely low nonlinearity of the amplification fiber allows, to a large extent, avoidance of restricting nonlinear effects by stretching the pulses to only 50 ps. Therefore, the stretcher employing a gold-coated grating with 1200 lines/mm, can be made with 2 inch optics and stays compact in size. After the stretcher, an acousto-optic modulator (AOM) is used to lower the repetition rate to 1 MHz before coupling into the amplifying fiber. The fiber is pumped from the opposite end by a fiber coupled diode laser emitting at 976 nm. After amplification, the pulses are re-compressed by a pair of fused silica transmission gratings with 1250 lines/mm [114]. Figure 8.4 (left) shows the compressed power at 1028 nm as function of pump power coupled into the fiber. A slope efficiency of 48% is obtained taking into account the efficiency of the amplifier and the compressor. Upon compression, the pulses

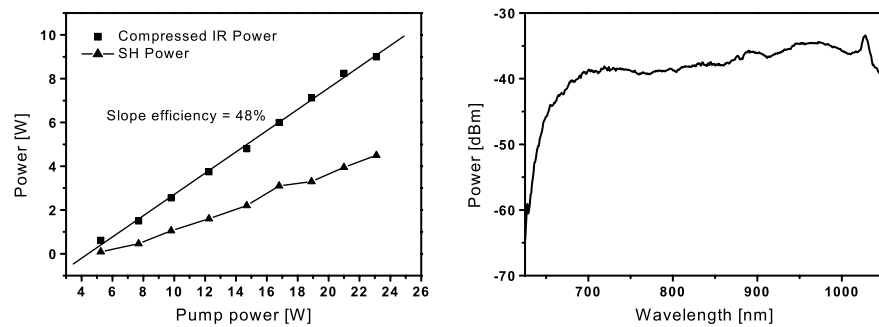


Figure 8.4: Slope efficiency of the fiber amplifier and resulting second harmonic power as functions of pump power coupled into the fiber.

are divided by a 4% beam-splitter and the weak signal is coupled into a 80 cm long PCF with a $3\ \mu\text{m}$ core diameter and ZDW at 975 nm (Crystal Fibre). A half-wave plate and an isolator are used to control the power launched into this fiber. The resulting SC (right panel of figure 8.4) stretches from about 600 nm to 1600 nm and provides a signal for the OPA of high spectral density and excellent beam quality. The remaining 1028 nm light is frequency doubled in a 1 mm BBO crystal cut for type I phase-matching with a conversion efficiency above 60%. The measured SH average power as a function of diode power is also shown in figure 8.4 (left). Based on measured autocorrelation traces of the IR pulses and simulations made with the SNLO software, the pulse duration of the SH is estimated to be 700 fs.

Finally, the super continuum and the SH are overlapped non-collinearly in a 5 mm long BBO crystal (type I) and temporal overlap is obtained by means of a delay stage. The SH beam is focused to a spot-size of roughly $100\ \mu\text{m}$ which enables peak-intensities of up to $70\ \text{GW}/\text{cm}^2$ while ensuring a proper spatial overlap with the seed.

8.4 Tunable parametric amplification

8.4.1 Broadband phasematching

Figure 8.5 a) shows the calculated broadband phase-matching curve for NOPA in a BBO crystal pumped at 514 nm in more detail. At an assumed non-collinearity angle of 2.6° (internal angle) between the pump and signal, the plot reveals a large amplification bandwidth ranging from 700 nm to 900 nm at a constant crystal angle of about 22° . A tunable output can therefore be realized by temporally scanning the pump pulse across the chirped broadband signal in the BBO crystal. Figure 8.5 b) shows the resulting spectra when the time delay

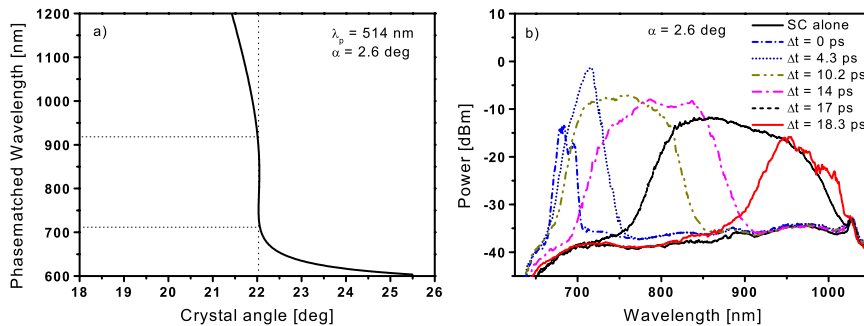


Figure 8.5: a) Broadband phase-matching for a type I BBO crystal pumped at 514 nm with a pump tilt angle of 2.6° . b) Amplification in the wavelength range 650-1000 nm by changing the temporal delay between pump and signal.

between signal and pump pulses is varied with a pump-signal angle of 2.6° and a fixed crystal angle. In effect, figure 8.5 b) shows a cross correlation of the chirped signal pulse with the much shorter pump pulse. The 18.3 ps measured between the time where the pump pulse overlaps with the narrow spectrum around 670 nm and the time where it overlaps with the broader spectrum around 970 nm, indicates the dispersion of the signal. To confirm this, a simulation of the pulse propagation through the 80 cm PCF was made by solving the extended nonlinear Schrödinger equation with a commercially available software [115]. Figure 8.6 depicts how the spectral region from 620 nm to 1040 nm of the simulated SC disperses relative to the pump wavelength at 1028 nm. A delay of roughly 18 ps between wavelengths around 670 nm and 970 nm is observed in concordance with the results presented in figure 8.5 b).

The broadband phasematching has significant influence on the duration of the amplified pulses as different delays cause spectral parts of different bandwidths to be sliced out by the pump pulse. Autocorrelation measurements have revealed pulse durations between 400 fs and 700 fs across the spectral range

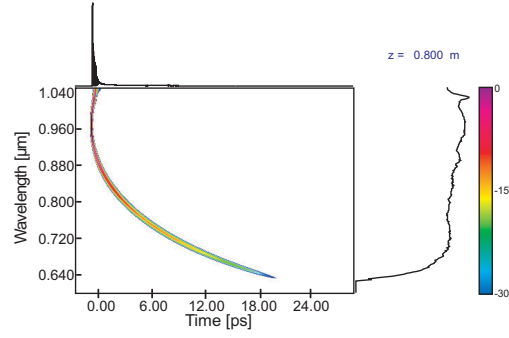


Figure 8.6: Simulated spectrogram of the supercontinuum generated in 80 cm of the PCF for the spectral range of 620 nm to 1040 nm. Time is measured relative to the 1028 nm center wavelength.

shown in figure 8.5 b).

8.4.2 Narrowband phasematching

When the pump-signal angle is different from 2.6° , the phasematching properties change considerably. Figure 8.7 a) shows the calculated and measured phase-matching curves when the two beams form an angle of 4.9° . Excellent

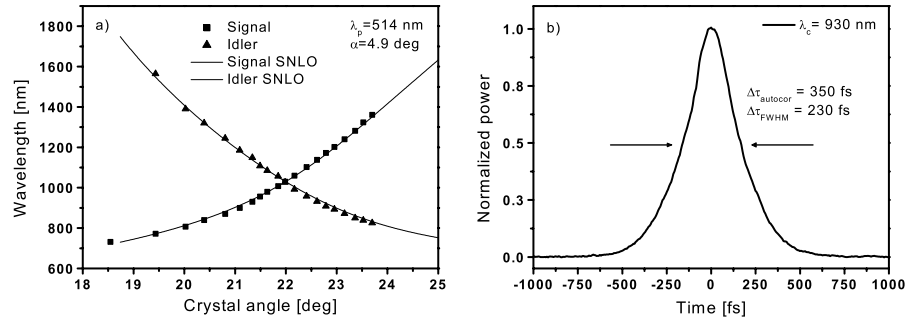


Figure 8.7: a) Phasematching for signal (squares) and idler (triangles) as found experimentally and calculated using SNLO software (line) when the angle between pump and signal is 4.9° . b) Autocorrelation trace when the center wavelength is approximately 930 nm.

agreement between experiment and theory is found for both signal and idler wavelengths, and tunability in the range 700 nm to 1500 nm is realized. The slopes in figure 8.7 a) illustrate that the phase-matching is spectrally narrow

compared to the situation described in the previous section, which results in shorter pulses as only a small part of the spectrum is picked out by the pump pulse. Autocorrelations show pulse durations of 250-320 fs as depicted in figure 8.7 b). Further compression of the pulses has been attempted but without significant reduction in pulse duration. Section 8.5 will describe the experiments on short pulse OPA in more detail.

Figure 8.8 a) shows the conversion efficiency for this configuration as a function of wavelength. Tuning is performed by rotating the crystal and the highest gain is found from 900 nm - 1000 nm. At the highest conversion, more than

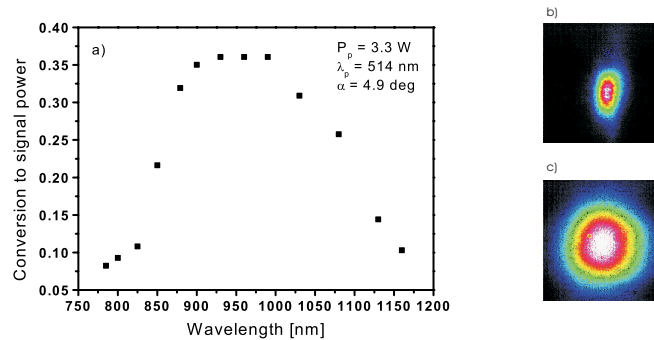


Figure 8.8: a) Signal conversion efficiency at a pump power of 3.3 W at 514 nm. Right: Beam profile at b) 30 % and c) 10 % conversion. The difference in spot-size is due to different scaling of the images.

1.2 W of average power, corresponding to a signal pulse energy of 1.2 μJ , is obtained. At this power level, the pump pulse energy in the fiber amplifier is roughly 8 μJ and the resulting peak power causes a nonlinear phase contribution which is not compensated by the compressor. As a consequence, the duration of the compressed pump pulses increases, which causes a decreasing pump peak power and reduced efficiency of the OPA stage. The lower trace in figure 8.4 shows the second harmonic power as function of pump power coupled into the amplifier fiber and the 'kink' at 17 W of pump power marks the onset of pulse-lengthening. At even higher pump powers, filamentation takes place in the BBO crystal which indicates too high pump intensity.

Figure 8.8 b) and 8.8 c) show measured amplified beam profiles for two different conversion efficiencies. Due to the generation of the continuum in a PCF, the signal has a Gaussian-like spatial profile. This is confirmed by the centrosymmetric mode shape at moderate conversion efficiencies. However, the beam profile deteriorates with increasing pump intensity and thus higher conversion efficiency. This effect can be explained by a saturation of the parametric am-

plification in the center of the beam which causes the mode to spread out in the direction of the highest gain, which coincides with the parametric fluorescence cone [116]. Depending on seed power, pump intensity and crystal length, a compromise between conversion efficiency and beam quality has to be found. Figure 8.8 b) shows the beam profile recorded with a CCD-camera when a 30% conversion was obtained. Although the beam is slightly elliptical and the fluorescence cone is present, it is still of acceptable quality. Looser focusing of the pump beam always results in improved beam quality as illustrated in figure 8.8 c) where the pump spot size is increased to $150 \mu\text{m}$. However, the conversion drops to about 10% with this configuration. Proper power scaling must therefore be made by expanding the beam size in the nonlinear crystal and increasing the pump power accordingly. With the present setup, the nonlinearity in the amplifier fiber restricts the pump power but future work will enable an increased spotsize and thereby a higher power output with perfect beam quality.

8.5 Short-pulse amplification

In this section, experiments with ultra-short pulse generation are described. First a proof of principle is made by spectral broadening in a standard fiber and subsequent OPA and recompression. Then the PCF from the previous sections is used to further increase the bandwidth, resulting in sub-40 fs pulses.

Although amplification of the SC from the PCF led to pulse durations of 250 fs (see figure 8.7), the wings on the autocorrelation trace indicate low pulse quality. Attempts to compress the pulses with a prism compressor did not lead to shorter pulses which indicates that the phase of the pulse is distorted. The phase problem can be understood by studying the SCG in more detail. Figure 8.9 shows a simulated spectrogram of the supercontinuum and illustrates how different parts of the spectrum appear as isolated peaks (NSR, FWM, XPM) at different times. Higher order solitons breathe and emit NSR at each spectral expansion and these NSR-peaks are therefore separated in time and phase. Later on, FWM and XPM add more peaks and the spectrum is seen to consist of several distinct features. The spectral coherence is reduced and compression is inhibited since the dispersive compressor can not be optimized for each spectral feature independently [117, 118]. Soliton fission must therefore be avoided if high quality pulses are the goal.

To reduce nonlinearity, the PCF is therefore replaced with a 9 cm piece of standard single-mode step-index fiber (Flexcore HI 1060) with a core diameter of $6 \mu\text{m}$. The dimensions of the fiber limit the nonlinear effects to SPM which, to a large extent, can be compensated in a prism compressor (section 2.2.3). Compression to sub-50 fs is however demanding and accumulation of nonlinear phase must be minimized. The standard fiber is therefore placed before the

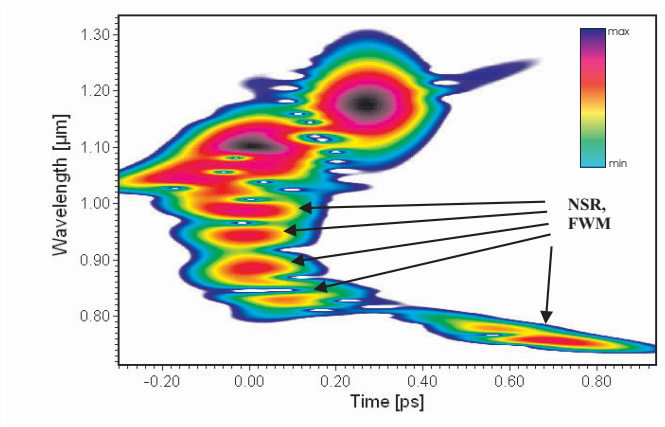


Figure 8.9: Simulated spectrogram of SCG in the used PCF. 200 fs, 1 nJ pulses at 1030 nm result in emission of several dispersive waves, and subsequent FWM and XPM, means that coherence is limited to small regions around each feature.

amplifier fiber in order to pump it with clean pulses from the oscillator instead of distorted pulses from the fiber amplifier. As a consequence textbook SPM spectra are generated and compression to high quality pulses is possible - as shown in figure 8.10.

The experimental setup is basically identical to the scheme shown in figure 8.3 except from the following modifications: The AOM is placed before the stretcher and a beam-splitter is used to send 50% of the 1 MHz beam (50 mW) into 9 cm of the standard fiber while the remaining part is stretched to 50 ps and coupled into the amplifier fiber as described before. The amplified pulses are re-compressed and again frequency doubled in the 1 mm BBO crystal. The SPM-broadened spectrum from the standard fiber is overlapped near-collinearly with the 514 nm pump in the 5 mm BBO crystal. With the crystal oriented for degenerate phase-matching, the entire 85 nm broad spectrum is amplified as seen in figure 8.10 a). Figure 8.10 b) shows the autocorrelation trace of the amplified pulse after compression in a simple fused silica prism-sequence. The initial 380 fs pulses from the oscillator have been reduced to only 46 fs, assuming a sech^2 pulse shape. With 3 W of green pump power, a signal average power of 0.5 W corresponding to a peak power of 10 MW is obtained. As expected, the autocorrelation trace is not affected by the parametric amplification, and the pulse wings, seen on the autocorrelation trace, originate from uncompensated nonlinear SPM-chirp (see section 2.2.3).

Even shorter pulses can be obtained by returning to the non-collinear geometry where phasematching can be obtained over 200 nm (see figure 8.5). To get a seed in the spectral region 700-900 nm, the standard fiber is replaced with the

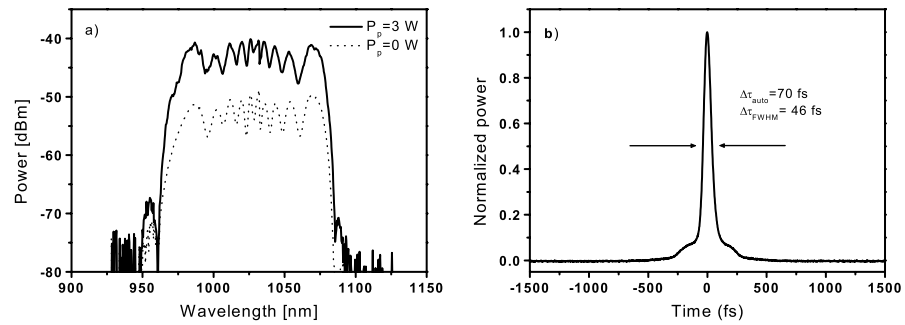


Figure 8.10: a) Measured spectrum after 9.1 cm of standard fiber (dotted black) and after amplification in the BBO crystal (red). b) Autocorrelation trace of the 46 fs re-compressed pulse just after the prism compressor.

PCF from before. As illustrated in figure 8.9, soliton fission must be avoided if a compressible output is desired. Simulations show that, by keeping the power coupled to the PCF below the soliton formation threshold, the pulse propagation will be dominated by SPM. Due to the high nonlinearity, it is possible to SPM broaden the spectrum more than 400 nm in this way. Figure 8.11 shows a spectrogram of such a 'continuum' which, in contrast to the spectrum shown

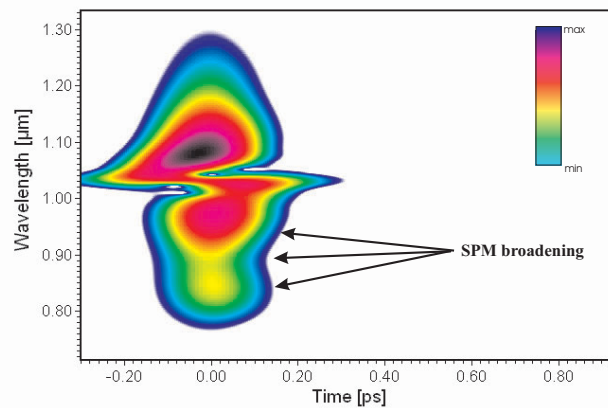


Figure 8.11: Simulated spectrogram when the power coupled to the PCF is kept below the threshold for soliton formation ($N < 0.5$)

in figure 8.9, is coherently broadened. The spectrum is seen to extend into the gain region of the NOPA configuration (700-900nm) and amplification of a part of the spectrum is therefore possible. The upper left corner of figure 8.12 shows the simulated spectrum from figure 8.11 while the upper right panel shows how

the spectral range from 800-900 nm can be compressed to 16 fs (assuming sech^2 pulse) in a simple prism sequence. The lower row of the figure shows the experimental realization of this idea. By coupling few-pJ pulses into the PCF, soliton dynamics is avoided and the part of the spectrum below 900 nm can be amplified and re-compressed. The shown autocorrelation trace has a FWHM

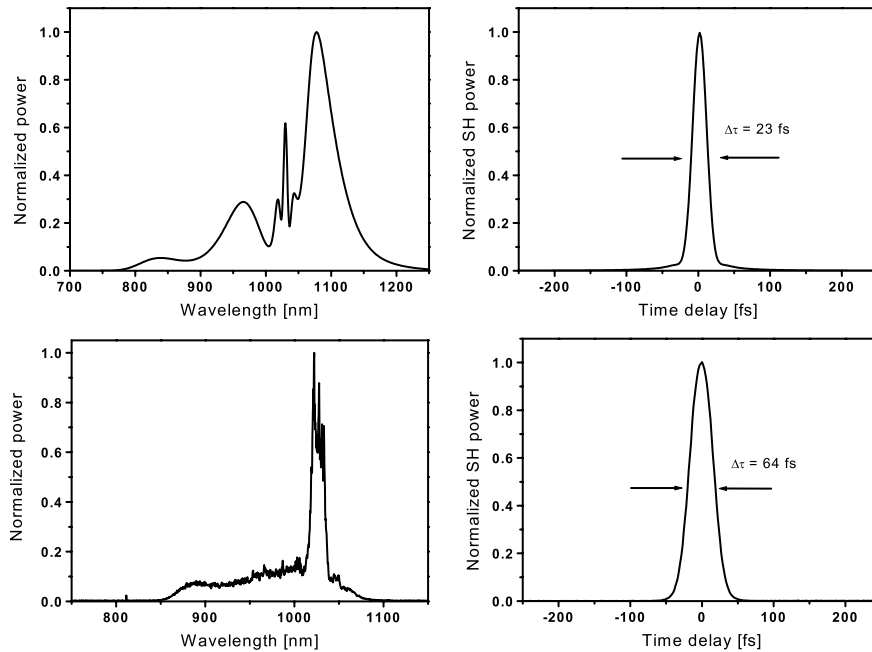


Figure 8.12: Upper row shows simulated spectrum and autocorrelation trace. The bandwidth from 800-900 nm is compressible to 16 fs. Bottom row shows experimental results. The autocorrelation trace indicates a pulse duration of 40 fs which is also the maximum resolution of our autocorrelation setup.

of 64 fs, corresponding to a 40 fs sech^2 pulse. The thickness of the nonlinear crystal in the autocorrelator limits the temporal resolution to 40 fs, so the pulses could actually be as short as 25 fs.

The average power of the amplified compressed signal is limited to 2 mW due to the very weak seed from the PCF which is not enough to saturate the OPA stage. To get high power ultrashort pulses a second, and possible third, OPA stage must be implemented. It is straightforward to split the pump into more beams in order to pump several OPA stages and future work will employ this strategy.

Since a high pulse quality is obtained without any optimization of the compression scheme, further improvements of these results are certainly possible.

Furthermore, the amount of power coupled to the PCF must be optimized since more bandwidth should be possible while still avoiding soliton dynamics. It would also be interesting to experiment with different PCFs as varying the ZDW may allow increased bandwidth within the NOPA gain region.

8.6 Summary and outlook

In conclusion, an efficient optical parametric amplifier pumped by a fiber amplifier is demonstrated and shows the potential of this approach. Tunable femtosecond pulses at a repetition rate of 1 MHz and pulse energies up to 1.2 μJ are obtained. The simplicity of the setup and the potential for power scaling makes this configuration an interesting alternative to traditional Ti:Sapphire based NOPA-schemes.

Inability to compress the amplified SC pulses to less than 250-300 fs is found to originate in soliton dynamics and avoidance of soliton fission is necessary for high quality pulse compression. By using a standard fiber to SPM-broaden the spectrum, compression to 46 fs corresponding to peak powers of 10 MW, is achieved. Numerical simulations predict that sub-20 fs pulses are possible if a PCF is used for spectral broadening while keeping the power below the soliton formation threshold. Preliminary experiments indicate that this might actually be achievable in practice and sub-40 fs pulses are demonstrated without any optimization of the SC or the compression scheme.

Future work will focus on power scaling and further reduction of the pulse duration. It will be necessary to improve the performance of the fiber amplifier in order to avoid the accumulation of nonlinear phase and the resulting pump pulse-broadening when operating at high powers. It is fairly straight-forward to solve this problem as it is simply a matter of reducing the peak-intensity in the fiber. Using gratings with higher groove density and large-aperture optics, it is possible to stretch the pulses to more than 1 ns as opposed to the 50 ps used here. The onset of pulse-broadening will then be pushed with factor of 20 or more. Additionally, the amplifier fiber will be replaced with a short-length, LMA Ytterbium doped rod-type fiber which can deliver the same gain as the present fiber but with significantly reduced nonlinearity [28]. With relatively simple changes, the fiber amplifier will therefore be able to deliver compressible pulses at power levels many times higher than presented here. Using this concept as pump laser for two or more OPA-stages will enable generation of high average power, high peak power ultrashort (potentially sub-10 fs pulses) laser pulses.

Chapter 9

Summary and acknowledgements

9.1 Summary

This thesis has investigated several applications of nonlinear optics and optical fibers.

Chapter 3 described how an intra cavity frequency doubled Ti:Sapphire laser was used to pump an optical parametric amplifier seeded by a super continuum from a photonic crystal fiber (PCF). Amplification of the super continuum was demonstrated but the limited available pump power reduced the impact of the experiment to a proof of principle.

Chapter 4 investigated four wave mixing in a highly nonlinear PCF. The unusual dispersion of the fiber enabled four wave mixing to take place over a wide wavelength range when the fiber was pumped in the anomalous regime and close to the zero-dispersion wavelength. A tunable output was therefore possible even with low pump powers and wavelength conversion with continuous wave lasers was demonstrated. Fibers with this type of dispersion profile may be interesting media for optical parametric oscillation.

Chapter 5 described an all-fiber Q-switched fiber laser based on magnetostrictive modulation of a fiber Bragg grating. An Yb-doped single-mode fiber was used as gain medium and 500 nJ, 200 ns pulses were demonstrated. The output was limited by pre-lasing on the weakly reflective sidebands of the gratings and employment of strongly apodized gratings is required for further progress. It may be possible to use the magnetostrictive technique to directly Q-switch a large mode area fiber which would greatly enhance the power extraction.

Chapter 6 described a fiber based interferometric setup to measure dispersion in optical fibers. The method is simple, fast and allows accurate determination of the fiber dispersion in the wavelength range 900-1200 nm.

In Chapter 7, dual-wavelength pumping of PCFs was studied. Experiments, as well as simulations, showed that co-propagating two femtosecond pulses at opposite sides of the zero dispersion wavelength led to spectral broadening due to cross phase modulation of the dispersive pulse by fundamental solitons. The mechanism is used commercially in a white-light source from Koheras and the improved understanding of the process may lead to further product development.

In Chapter 8 the idea of amplifying a super continuum from a PCF in an optical parametric amplifier stage was pursued with a high power fiber laser pumped setup. The performance of the fiber laser allowed demonstration of a MHz repetition rate, μ J-level, tunable femtosecond source. Furthermore, pulses from the amplified super continuum were compressed to sub-40 fs and simulations indicated that sub-20 fs pulses are possible. Since the setup is power scalable, it may represent a new route to a compact, high power ultra-fast laser system.

9.1.1 Perspectives

Optical fibers and PCFs in particular, are 'hot topics' in the research community and will continue to be so in the coming decade. Compact fiber based devices and lasers are already emerging and will without doubt replace many conventional solid state lasers in research labs and eventually in industry. The potential simplicity of fiber based systems may even allow real-world applications of the ultra-fast laser technology. Femtosecond laser systems are now invaluable tools in many branches of science, but industrial implementation has so far been excluded by the complexity of the setups. Lifting this technology out of the science labs is certain to bring new and interesting applications.

Since the first demonstration of the PCFs in 1996, a lot of research activity has been focused on understanding the properties of these fibers. The spectacular super continua from small core, highly nonlinear PCFs are now understood and have already found applications in tomography and frequency metrology. The frequency standard of today is actually based on the frequency comb in the output from a PCF [119].

But the PCF technology offers many other possibilities than high nonlinearity and dispersion management. High birefringence, multi-core and multi-clad designs, high power carriage and hosting of Rare-Earth dopants can all be implemented in the fiber design. The latter has enabled a new generation of high power fiber lasers which are performing as well or better than conventional solid state lasers. High power fiber lasers are actually emerging as an increasingly hot topic on their own. Apart from the interesting physics of high power generation, there is also a significant financial motivation to improve the performance of these lasers. The prospect of getting a share of a prosperous laser market has encouraged investments in the development of these fiber lasers, and as a result the technology has matured in just a few years. It will be most interesting to see what the future brings for high power fiber lasers. If they can be made to fulfil the necessary requirements for durability and stability, there is no doubt that they will successfully take over many laser applications.

9.2 Acknowledgements

I have had a great time as a student at the Aarhus University and I wish to thank a number of people for contributing to this experience. First of all I acknowledge my supervisor Søren Keiding for his support during the last 4 years. I am most grateful for Søren accepting me as a PhD student and it has been a thrill to be a member of his group. Søren has managed to function as professor, protector and supervisor while still maintaining an informal and humorous atmosphere. I also thank Jan Thøgersen for all his help - Jan has been an inspiration in the lab and has contributed to most of the work presented here. Likewise, I thank Jakob Juul Larsen for his support. Jakob functioned as external supervisor for the NKT-Academy students in Århus for about two years and was an invaluable help for all of us.

All members of Femtolab and NKT-lab are gratefully acknowledged for their companionship and for creating an inspiring and pleasant environment. Special thanks to Victoria Birkedal for proof-reading this thesis.

I also acknowledge the helpfulness of the people at Crystal Fibre and Koveras and thank NKT Academy for partially financing my Ph.D. studies. NKT-Research is especially acknowledged for their financial and technical support during the last four years. Visiting NKT-Research has always brought inspiration and drive to my projects and I am most grateful for the attention and help I have received from their side. Special thanks to Claus Friis Pedersen for his support and engagement in the work in Aarhus.

The members of the fiber laser group in Jena are thankfully acknowledged for their hospitality and excellent company. It was highly motivating to experience the attitude and work ethics in their labs and I really appreciate the time I spent there.

Finally, I would like to thank my friends and family outside the university. They have always been supportive and showed interest for my project. The last 'gracias' is for Dolores who has lived through four Danish winters to give me the opportunity to pursue this PhD. She has been extremely supportive and has also helped me with this thesis.

Thomas Vestergaard Andersen

Appendix A

List of Abbreviations

ASE	Amplified spontaneous emission
BBO	β -Barium Borate
BS	Beam splitter
CCD	Charge-coupled device
D	Dispersion parameter
DC	Double clad
Er	Erbium
FD	Finite difference
fs	Femtosecond
FT	Fourier transform
FWHM	Full-width at half maximum
FWM	Four wave mixing
FOPO	Fiber optical parametric oscillator
GVD	Group velocity dispersion
HWHM	Half-width at half maximum

IR	Infrared
LMA	Large mode area
MF	Microstructured fiber
MOSFET	Metal oxide semiconductor field effect transistor
ns	Nanosecond
NA	Numerical aperture
Nd:YAG	Neodymium:Yttrium Aluminum Garnet
NIR	Near-infrared
NL	Nonlinear
NSR	Non-solitonic radiation
NOPA	Non-collinear parametric amplification
OPA	Optical parametric amplification
PBG	Photonic bandgap
PCF	Photonic crystal fiber
PM	Polarization maintaining
ps	Picosecond
RE	Rare Earth
SC	Supercontinuum
SCG	Super continuum generation
SEM	Scanning electron microscope
SPM	Self-phase modulation
Ti:Sapphire	Titanium Sapphire
TOD	Third order dispersion
WDM	Wavelength division multiplexing
XPM	Cross phase modulation
Yb	Ytterbium
ZDW	Zero dispersion wavelength

Appendix B

Numerical model

A numerical model is made to investigate the origin of the envelope modulation observed from the all-fiber Q-switched laser presented in chapter 5. The scheme presented here has also been used to simulate fiber amplifiers.

Q-switched fiber lasers have traditionally been modelled with so-called point models in which the gain is assumed constant along the length of the fiber [22]. In highly doped Yb-fibers this approach is no longer valid and a z-dependent inversion must be included in the model, z being the distance along the fiber. Furthermore, the short upper state life time of Yb³⁺ implies significant ASE which also influence the pulse formation. For accurate modelling it is therefore necessary to adopt a travelling wave model in which both forward and backward ASE waves are included.

The optically active energy levels in Yb³⁺ can be treated as a 2-level system with wavelength dependent cross-sections for emission and absorption (section 2.3). With the populations of the two levels given by N_1 and N_2 , the following rate equations can be derived [82, 120]:

$$N_T = N_1 + N_2 \quad (\text{B.1})$$

$$\begin{aligned} \frac{\partial N_2}{\partial t} &= \frac{\Gamma_p \lambda_p}{hcA} [\sigma_{a,p} N_1 - \sigma_{e,p} N_2] P_p - \frac{N_2}{\tau_0} \\ &\quad + \sum_{\nu} \frac{\Gamma_{\nu} \lambda_{\nu}}{hcA} [\sigma_{a,\nu} N_1 - \sigma_{e,\nu} N_2] (P_{\nu}^{+} + P_{\nu}^{-}) \end{aligned} \quad (\text{B.2})$$

$$\frac{\partial P_p}{\partial z} + \frac{1}{v_p} \frac{\partial P_p}{\partial t} = \Gamma_p [\sigma_{e,p} N_2 - \sigma_{a,p} N_1] P_p \quad (\text{B.3})$$

$$\begin{aligned} \frac{\partial P_{\nu}^{\pm}}{\partial z} \pm \frac{1}{v_{\nu}} \frac{\partial P_{\nu}^{\pm}}{\partial t} &= \pm \Gamma_{\nu} [\sigma_{e,\nu} N_2 - \sigma_{a,\nu} N_1] P_{\nu}^{\pm} \\ &\quad \pm 2\sigma_{e,\nu} N_2 \frac{hc^2}{\lambda_{\nu}^3} \Delta\lambda_{\nu} \end{aligned} \quad (\text{B.4})$$

where N_T is the dopant concentration, λ_{ν} is the wavelength of channel ν , h is Planck's constant, c the speed of light, τ_0 the lifetime of the upper state, A the area of the dopant distribution and σ_i is the cross section of absorption ($i=a$) and emission ($i=e$) for pump (p) and signal (ν). Γ_p, Γ_{ν} are the spatial overlaps between the fiber mode and the doped area of the fiber. The forward and backward propagating waves P_{ν}^{\pm} , are coupled through the population inversion, N_2 , and the pump and signal waves propagate with speed v_p and v_{ν} , respectively. The term $2\sigma_{e,\nu} N_2 \frac{hc^2}{\lambda_{\nu}^3} \Delta\lambda_{\nu}$ in eq. B.4 is the contribution from spontaneous emission in the wavelength interval $\Delta\lambda$ into the fundamental mode [22, 121]. The expression assumes that there is only one guided spatial mode in the fiber.

Figure B.1 illustrates the modelling scheme. The gain spectrum of Yb is divided into channels of width $\Delta\lambda$, and the power in each channel P_{ν}^{\pm} is propagated through the fiber according to the rate equations. Some of the channels experience feedback from the fiber Bragg gratings (FBGs), and Q-switching takes place when FBG2 moves into channels which already have feedback from

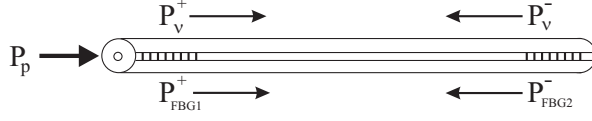


Figure B.1: ASE power P_ν , propagates backwards and forwards and steady state is obtained with the two Bragg gratings detuned. FBG2 is then moved to coincide with the wavelength (channels) of FBG1 and a cavity is formed.

FBG1, resulting in formation of a cavity (high Q-factor). A one-directional pumping scheme is assumed for simplicity.

Numerically, the Q-switching is done in two steps. Firstly, there is a build-up time where the gratings are in distinct channels and steady state is reached. The resulting power and inversion distribution are calculated from eq. B.1-B.4 with the time derivatives set equal to zero (steady state). The coupled differential equations are constrained by initial boundary conditions, namely $P_\nu^+(0) = 0$ and $P_\nu^-(L) = 0$. For the channels containing the FBGs, the conditions $P_k^+(0) = R_{FBG1} \cdot P_k^-(0)$ and $P_m^-(L) = R_{FBG2} \cdot P_m^+(L)$, where R_{FBG} is the reflectivity of the FBGs, must be fulfilled. The pump channel is subjected to $P_p(0) = P_0$, where P_0 is the input pump power.

When the steady state inversion and power distributions are known, the Q-switching is made by gradually increasing the feedback from FBG2 in the channels where there is already feedback from FBG1. The signal, P_s^\pm is now strongly amplified and the ASE channels become insignificant in comparison. It is therefore a reasonable approximation to ignore the remaining ASE contribution and simply solve the travelling wave problem for the signal channels. The problem is then reduced to the partial differential equations representing the (few) signal channels containing the resonant counter propagating waves. This is solved with a finite difference (FD) method [122, 123] in which the rate equations B.1-B.4 are evaluated on a grid where each point represents a set of (z,t) coordinates - as illustrated in figure B.2. The equations are discretized according to (assuming $\Gamma_p = \Gamma_\nu = 1$)

$$\begin{aligned}
 N_2(z, t_{i+1}) = & \left[\frac{\lambda_p}{hcA} [\sigma_{a,p} N_1(z_i, t_i) - \sigma_{e,p} N_2(z_i, t_i)] P_p(z_i, t_i) \right. \\
 & + \sum_{\nu} \frac{\lambda_\nu}{hcA} [\sigma_{a,\nu} N_1(z_i, t_i) - \sigma_{e,\nu} N_2(z_i, t_i)] (P_\nu^+(z_i, t_i) + \dots \\
 & \left. \dots P_\nu^-(z_i, t_i)) - \frac{N_2(z_i, t_i)}{\tau_0} \right] \Delta z + N_2(z_i, t_i) \quad (B.5)
 \end{aligned}$$

$$\begin{aligned}
 P_p(z_{i+1}, t_{i+1}) = & \left[\sigma_{e,p} N_2(z_i, t_i) - \sigma_{a,p} N_1(z_i, t_i) \right] P_p(z_i, t_i) \Delta z + P_p(z_i, t_i) \\
 & (B.6)
 \end{aligned}$$

$$P_{\nu}^{+}(z_{i+1}, t_{i+1}) = \left[[\sigma_{e,\nu} N_2(z_i, t_i) - \sigma_{a,\nu} N_1(z_i, t_i)] P_{\nu}^{+}(z_i, t_i) + 2\sigma_{e,\nu} N_2(z_i, t_i) \frac{hc^2}{\lambda_{\nu}^3} \Delta\lambda_{\nu} \right] \Delta z + P_{\nu}^{+}(z_i, t_i) \quad (\text{B.7})$$

$$P_{\nu}^{-}(z_{i-1}, t_{i+1}) = \left[[\sigma_{e,\nu} N_2(z_i, t_i) - \sigma_{a,\nu} N_1(z_i, t_i)] P_{\nu}^{-}(z_i, t_i) + 2\sigma_{e,\nu} N_2(z_i, t_i) \frac{hc^2}{\lambda_{\nu}^3} \Delta\lambda_{\nu} \right] \Delta z + P_{\nu}^{-}(z_i, t_i) \quad (\text{B.8})$$

The steady state calculations provides the initial distributions at $(z, t_{i=1})$, so the evolution of the Q-switched pulse can be simulated by simply stepping through the equations B.5-B.8. Figure B.2 shows a geometrical interpretation of pulse propagation through the fiber. The time axis is divided into steps of Δt , and the corresponding z -step is then given by $\Delta z = v \Delta t$. The total step is then given by $\frac{d}{dz} = \frac{\partial}{\partial z} + \frac{1}{v} \frac{\partial}{\partial t}$ and is therefore 'diagonal'. The figure illustrates

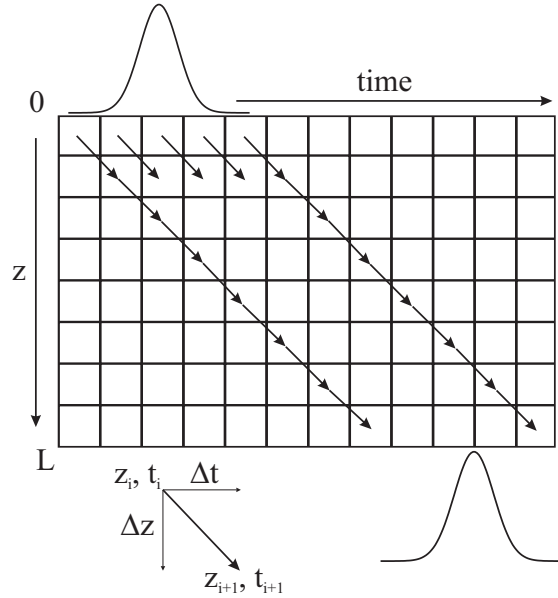


Figure B.2: Time and z are discretized and the propagation is modelled by moving diagonally across the grid.

a typical fiber amplifier scheme where a pulse is launched into the fiber at $t = 0$ and propagates through the fiber. This kind of single-pass is particularly simple to simulate since there is no feedback from the fiber ends. In the case of Q-switching, complexity is added by the fact that there is feedback from the

gratings and thereby multiple passes through the fiber. When stepping through the FD-grid, it is therefore necessary to 'inject' power at both $z=0$ and $z=L$ according to the conditions

$$P_{\nu}^{+}(0, t_{i+1}) = R_{FBG1} \cdot P_{\nu}^{-}(\Delta z, t_i) \quad (\text{B.9})$$

$$P_{\nu}^{-}(L, t_{i+1}) = R_{FBG2}(t) \cdot P_{\nu}^{+}(L - \Delta z, t_i) \quad (\text{B.10})$$

The output from the laser is monitored after FBG2 and is given by

$$P_{out}(t) = [1 - R_{FBG2}(t)] P_{\nu}^{+}(L, t) \quad (\text{B.11})$$

The following values are employed in the simulations: $N_T = 1.8 \cdot 10^{25}/\text{m}^3$, $L = 1.5$ m, $\tau_0 = 900$ μs , $A = 16$ μm^2 . For simplicity, the gratings are contained in one channel only and their reflectivity is described by $R_{FBG1} = 0.95$ and $R_{FBG2}(t) = 0.85 \cdot (t/\tau)$, with τ being the rise time of the switch. The linear time dependence of the switch is a simple approximation but it suffices for qualitative predictions. Since the dopant distribution and different mode areas are crudely approximated, the model does not provide quantitative results anyway. Additionally, the use of steady state distributions before Q-switching assumes that the fiber is fully inverted between pulses and this is only the case when working at repetition rates below 10 kHz. In spite of these flaws, the model is a useful tool for illuminating general trends and much can be learned about the system by varying parameters independently. Figure B.3 displays calculated steady state population of the upper level for pump powers of 200 mW, 300 mW

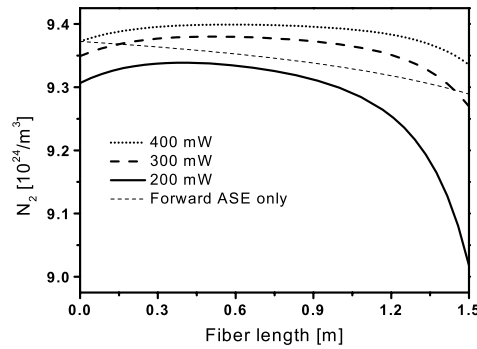


Figure B.3: Simulated upper state population N_2 for different pump powers. The thin dashed line represents a calculation with only forward inversion.

and 400 mW. N_2 is power and z -dependent, and for low pump powers the gain is reduced at the end of the fiber. The dip in the upper state population in

the beginning of the fiber is due to backward propagating ASE which builds up along the fiber and effectively drains the high inversion at the input end. The thin dashed line represents a calculation at 200 mW of pump power where only forward ASE is included. The difference between the two 200 mW curves illustrates the need of including the counter propagating ASE waves.

Figure B.4 (left) shows pulse duration and peak power as function of the applied pump power when the rise time of the switch is fixed at $10 \mu\text{s}$. Increased gain is seen to lead to shorter pulses with higher peak powers. The same parameters are plotted against the rise time of the switch, τ in figure B.4 (right). For this figure the pump power is kept constant at 50 mW. The used values of τ are not comparable to the experimental rise time but the figure illustrates that a faster switch has the same effect as higher gain, i.e. decreased pulse duration and increased peak power. To investigate the effect of the switching

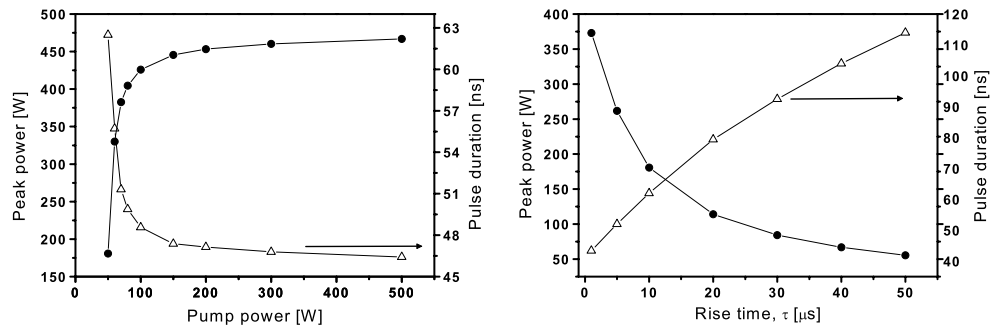


Figure B.4: Left: Simulated peak power and pulse duration as function of pump power. Increased pump power leads to shorter pulses with higher peak power. Right: Same parameters as function of the rise time of the switch. A fast switch leads to shorter pulses with higher peak power. Dots and open triangles mark calculated data.

speed on the pulse shape, a fixed pump power of 50 mW is applied and different values of τ are tested. Figure B.5 illustrates the pulse shape for $\tau=0.1, 0.5, 1$ and $5 \mu\text{s}$ and clearly shows that a fast switch can indeed induce a modulation of the pulse envelope. This effect is caused by repetitive amplification of the initial ASE wave which is injected into the cavity when the switch is turned on. The leading edge of this wave sees higher gain and is therefore preferentially amplified. Each time the front of this wave reaches the output coupler a peak is seen in the output pulse. More detailed calculations and experimental demonstrations have revealed that the rise time of the switch must be of the order of the round trip time before this effect is significant [82, 122]. As the switch in our experiment is roughly three orders of magnitude slower than the round trip time, the pulse envelope modulation does not originate from the switching

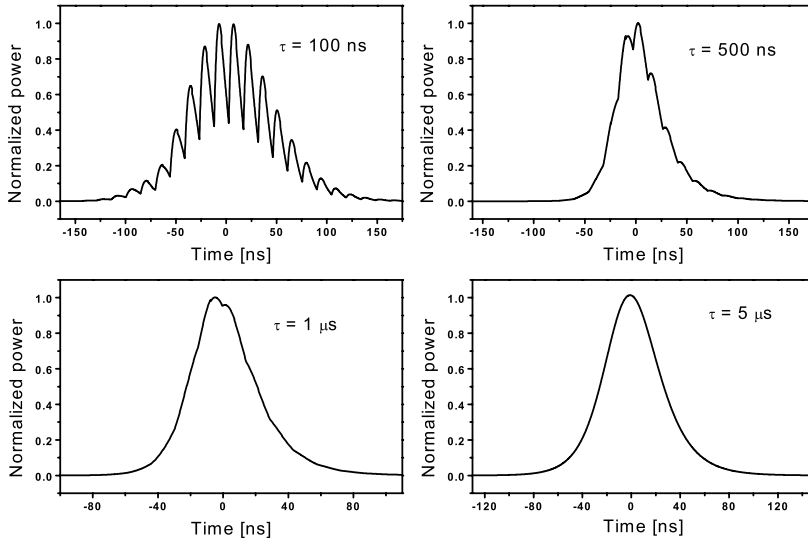


Figure B.5: Simulated pulse shapes for different rise times of the switch. A fast switch gives rise to a modulation of the pulse envelope corresponding to the round trip time in the cavity. The effect is caused by repetitive amplification of the initial ASE wave which is injected into the cavity when the switch is activated. Slow switching results in a clean envelope with a slightly asymmetric shape, characteristic for Q-switching [43].

process.

The modulation of the pulse envelope is therefore believed to be caused by coherent effects. To investigate this further, Ricardo Duchowicz [124], one of the collaborators of this project, made a slight modification of the model. The change consists of replacing eq. B.4, which describes the evolution of the signal power, with a corresponding equation for the electric field amplitude of the signal, A

$$\frac{\partial A_{\nu}^{\pm}(z, t)}{\partial z} \pm \frac{1}{v_{\nu}} \frac{\partial A_{\nu}^{\pm}(z, t)}{\partial t} = \pm \frac{\Gamma_{\nu}}{2} [\sigma_{e, \nu} N_2(z, t) - \sigma_{a, \nu} N_1(z, t)] A_{\nu}^{\pm}(z, t) \quad (\text{B.12})$$

where the signal power is then given by

$$P_s(z, t) = \left| \sum_{\nu} A_{\nu}^{+}(z, t) \right|^2 + \left| \sum_{\nu} A_{\nu}^{-}(z, t) \right|^2 \quad (\text{B.13})$$

This expression allows simulation of beating between co-propagating waves, and by dividing the bandwidth of the grating into k channels, a time and wavelength dependent phase-shift can be incorporated as well.

As before, a steady state solution to the rate equations is first obtained and the resulting power distributions are propagated through the FD grid. Counter-propagating waves are only coupled through the FBGs which are simulated by assuming a homogeneous refractive index distribution and an added phase shift when the frequency of the incoming wave is different from the Bragg frequency [83]. The boundary conditions, including the (complex) reflection coefficients of both gratings, are then given by

$$\begin{aligned} P_p(t, z = 0) &= P_0 \\ A_\nu^+(t, z = 0) &= A_\nu^-(t, z = 0)r_{0,\nu} \\ A_\nu^-(t, z = L) &= A_\nu^+(t, z = L)r_{L,\nu}(f(t)) \end{aligned} \quad (\text{B.14})$$

where P_0 is the incident pump power and r_i are the reflection coefficients in ref. [83]. The time dependent Bragg frequency, $f(t)$ is modelled by the following expression

$$f(t) = f_0 - \Delta f[1 - \sin^2(2\pi Ft)] \quad (\text{B.15})$$

where $\Delta f = 0.3$ nm and F is the frequency with which the grating is modulated.

The calculations give rise to the pulse shape displayed in figure 5.5 which shows qualitative agreement with the experimentally observed pulse. It should be noted that the time-dependent phase shift upon reflection at FBG2 is required for obtaining the modulation. Similar effects have been reported in other systems [84], and it seems probable that the motion of FBG2 is the cause of the envelope modulation. In this context, it is interesting that experiments with pulsed distributed feedback fiber lasers where the gratings are stationary, do not lead to these amplitude modulations [85].

References

- [1] (<http://www.nkt.dk>).
- [2] A. V. Husakou and J. Herrmann, “Supercontinuum generation of higher-order solitons by fission in photonic crystal fibers,” *Phys. Rev. Lett.* **87**, 901 (2001).
- [3] J. Herrmann, U. Griebner, N. Zhavoronkov, A. Husakou, D. Nickel, J. C. Knight, W. J. Wadsworth, and P. S. J. Russell, “Experimental evidence for supercontinuum generation by fission of higher-order solitons in photonic crystal fibers,” *Phys. Rev. Lett.* **88**, 901–904 (2002).
- [4] (<http://www.imra.com>).
- [5] (<http://www.aep.cornell.edu>).
- [6] J. R. Buckley, F. W. Wise, F. O. Ilday, and T. Sosnowski, “Femtosecond fiber lasers with pulse energies above 10 nJ,” *Opt. Lett.* **30**, 1888–1890 (2005).
- [7] (<http://www.ipgphotonics.com>).
- [8] (<http://www.iap.uni-jena.de>).
- [9] F. Röser, J. Rothhard, B. Ortac, O. Schmidt, T. Schreiber, J. Limpert, and A. Tünnermann, “131 W 220 fs fiberlaser system,” *Opt. Lett.* **30**, 2754–2756 (2005).
- [10] R. Boyd, *Nonlinear optics* (Academic Press, 1992).
- [11] K. J. Blow and D. Wood, “Theoretical description of transient stimulated Raman scattering in optical fibers,” *J. Quantum Electronics* **25**, 2665 (1989).
- [12] G. P. Agrawal, *Nonlinear fiber optics* (Academic, New York, 1995).

- [13] R. H. Stolen, J. P. Gordon, W. J. Tomlinson, and H. A. Haus, "Raman response function of silica-core fibers," *J. Opt. Soc. Am. B* **6**, 1159 (1989).
- [14] A. Ghatak and K. Thyagarajan, *Introduction to fiber optics*, chap. 17, pp. 384–386 (Cambridge, 2000).
- [15] P. V. Mamyshev and S. V. Chernikov, "Ultrashort-pulse propagation in optical fibers," *Opt. Lett.* **15**, 1076 (1990).
- [16] D. Gloge, "Weakly guiding fibers," *Appl. Optics* **10**, 2252 (1971).
- [17] J. D. Jackson, *Classical Electrodynamics* (John Wiley and Sons, 1999).
- [18] Z. Jiang, S.-D. Yang, D. E. Leaird, and A. M. Weiner, "Fully dispersion-compensated 500 fs pulse transmission over 50 km single-mode fiber," *Opt. Lett.* **30**, 1449 (2005).
- [19] P. Russel, "Photonic crystal fibers," *Science* **299**, 358–362 (2003).
- [20] O. E. Martinez, J. P. Gordon, and R. L. Fork, "Negative group velocity dispersion using refraction," *J. Opt. Soc. Am. A* **1**, 1003 (1984).
- [21] M. Suzuki, N. Edagawa, H. Taga, H. Tanaka, S. Yamamoto, and S. Akiba, "10 Gb/s, over 12200 km soliton data transmission with alternating-amplitude solitons," *IEEE Photonics Techn. Lett* **6**, 757 (1994).
- [22] M. J. F. Digonnet, *Rare-Earth-doped fiber lasers and amplifiers* (Marcel Dekker Inc., New York, 2001). (see page 389 for an extensive overview).
- [23] H. M. Pask, R. J. Carman, D. C. Hanna, A. C. Tropper, C. J. M. ans P. R. Barber, and J. M. Dawes, "Ytterbium-doped silica fiber Lasers : Versatile sources for the 1-1.2 μm region," *J. Quantum Electronics* **1**, 2 (1995).
- [24] J. C. Knight, T. A. Birks, P. S. J. Russell, and D. M. Atkin, "All-silica single-mode fiber with photonic crystal cladding," *Opt. Lett.* **21**, 1547–1549 (1996).
- [25] J. Broeng, S. E. Barkou, T. Søndergaard, and A. Bjarklev, "Analysis of air-guiding photonic bandgap fibers," *Opt. Lett.* **25**, 96 (2000).
- [26] T. A. Birks, J. C. Knight, and P. S. J. Russell, "Endlessly single-mode photonic crystal fiber," *Opt. Lett.* **22**, 961 (1997).
- [27] M. Koshiba and K. Saitoh, "Applicability of classical optical fiber theories to holey fibers," *Opt. Lett.* **29**, 1739 (2004).

- [28] J. Limpert, N. Deguil-Robin, I. Manek-Hönniger, F. Salin, F. Röser, A. Liem, T. Schreiber, S. Nolte, H. Zellmer, A. Tünnermann, J. Broeng, A. Petersson, and C. Jakobsen, “High-power rod-type photonic crystal fiber laser,” *Opt. Express* **13**, 1055–1058 (2005).
- [29] A. L. Gaeta, “Catastrophic collapse of ultrashort pulses,” *Phys. Rev. Lett.* **84**, 3582 (2000).
- [30] R. Holzwarth, M. Zimmermann, T. Udem, T. W. Hänsch, P. Russbüldt, K. Gäbel, R. Poprawe, J. C. Knight, W. J. Wadsworth, and P. S. J. Russell, “White-light frequency comb generation with a diode-pumped Cr:LiSAF laser,” *Opt. Lett.* **26**, 1376 (2001).
- [31] H. Lim, Y. Jiang, Y. Wang, Y. C. Huang, Z. Chen, and F. W. Wise, “Ultrahigh-resolution optical coherence tomography with a fiber laser source at 1 mm,” *Opt. Lett.* **30**, 1171 (2005).
- [32] A. Ortigosa-Blanch, J. C. Knight, and P. S. J. Russell, “Pulse breaking and supercontinuum generation with 200-fs pump pulses in photonic crystal fibers,” *J. Opt. Soc. Am. B* **19**, 2567–2572 (2002).
- [33] W. Wadsworth, A. Ortigosa-Blanch, J. Knight, T. Birks, T. Man, and P. Russell, “Supercontinuum generation in photonic crystal fibers and optical fiber tapers: a novel light source,” *J. Opt. Soc. Am. B* **19**, 2148–2155 (2002).
- [34] G. Genty, M. Lehtonen, H. Ludvigsen, J. Broeng, and M. Kaivola, “Spectral broadening of femtosecond pulses into continuum radiation in microstructured fibers,” *Opt. Express* **9**, 1083–1098 (2002).
- [35] J. Dudley, L. Provino, N. Grossard, H. Maillotte, R. Windeler, B. Eggleton, and S. Coen, “Supercontinuum generation in air-silica microstructured fibers with nanosecond and femtosecond pulse pumping,” *J. Opt. Soc. Am. B* **19**, 765–771 (2002).
- [36] G. Genty, M. Lehtonen, and H. Ludvigsen, “Route to broadband blue-light generation in microstructured fibers,” *Opt. Lett.* **30**, 756–758 (2005).
- [37] J. K. Ranka, R. S. Windeler, and A. J. Stentz, “Visible continuum generation in air-silica microstructure fibers with anomalous dispersion at 800 nm,” *Opt. Lett.* **25**, 25 (2000).
- [38] V. Petrov, D. Georgiev, and U. Stamm, “Improved modelocking of a femtosecond Titanium doped Sapphire laser by intracavity second harmonic generation,” *Appl. Phys. Lett.* **60**, 1550 (1992).

- [39] Y. Kang, Y. Chan, and C. Nam, "Intracavity frequency doubling in a femtosecond Ti:Sapphire laser using Lithium triborate and beta-Barium borate," *Jpn. J. Appl. Phys.* **38**, 85 (1999).
- [40] R. Ellingson and C. Tang, "High-repetition rate femtosecond pulse generation in the blue," *Opt. Lett.* **17**, 343 (1992).
- [41] S. Backus, M. Asaki, C. Shi, H. Kapteyn, and M. Murnane, "Intracavity frequency doubling in a Ti:Sapphire laser : Generation of 14-fs pulses at 416 nm," *Opt. Lett.* **19**, 399 (1994).
- [42] D. E. Spence, P. N. Kean, and W. Sibbett, "60-fs pulse generation from a self-mode-locked Ti:Sapphire laser," *Opt. Lett.* **16**, 42 (1991).
- [43] A. Siegmann, *Lasers* (University Science Books, 1986).
- [44] J. Zhou, G. Taft, C. Huang, M. Murnane, and H. Kapteyn, "Pulse evolution in a broad-bandwidth Ti:Sapphire laser," *Opt. Lett.* **19**, 1149 (1994).
- [45] Q. Lin and I. Sorokina, "Higher order dispersion effects in solitary mode-locked lasers : Sideband generation," *Opt. Commun.* **153**, 285 (1998).
- [46] T. Brabec and S. Kelly, "Third-order dispersion as a limiting factor to modelocking in femtosecond solitary lasers," *Opt. Lett.* **18**, 2002 (1993).
- [47] J. Elgin, T. Brabec, and S. Kelly, "A perturbative theory of soliton propagation in the presence of third order dispersion," *Opt. Commun.* **114**, 321 (1995).
- [48] J. Ranka, A. Gaeta, A. Baltuska, M. Pshenichnikov, and D. Wiersma, "Autocorrelation measurements of 6 fs pulses based on the two-photon-induced photocurrent in a GaAsP photodiode," *Opt. Lett.* **17**, 1344 (1997).
- [49] (<http://www.eksma.it/crystals.non/ultrath.htm>).
- [50] E. Riedle, M. Beutter, S. Lochbrunner, and J. Piel, "Generation of 10 to 50 fs pulses tunable through all of the visible and the NIR," *Appl. Phys. B* **71**, 457 (2000).
- [51] A. Steinmann, A. Killi, G. Palmer, U. Morgner, H. Bartelt, and J. Kobelke, "Tunable fs pulses from OPA with MHz repetition rate," Conf. contribution, *Advanced Solid State Photonics, ASSP*. p. TuC6 (2006).
- [52] K. M. Hilligsøe, T. V. Andersen, H. N. Paulsen, C. K. Nielsen, K. Mølmer, S. Keiding, and J. J. Larsen, "Supercontinuum generation in a photonic crystal fiber with two zero dispersion wavelengths," *Opt. Express* **12**(6), 1045–1054 (2004).

- [53] S. Watanabe, S. Takeda, and T. Chikama, "Interband wavelength conversion using a polarization-insensitive fiber four-wave mixer," *EU Conference on Optical Communication* **3**, 83–87 (1998).
- [54] J. E. Sharping, M. Fiorentino, and P. Kumar, "Optical parametric oscillator based on four-wave mixing in microstructured fiber," *Opt. Lett.* **27**(19), 1675–1677 (2002).
- [55] M. E. Marhic, K. K. Y. Wong, and L. G. Kazovsky, "Continuous wave fiber optical parametric oscillator," *Opt. Lett.* **27**(16), 1439–1441 (2002).
- [56] R. H. Stolen and J. E. Bjorkholm, "Parametric amplification and frequency conversion in optical fibers," *J. Quantum Electronics* **18**(7), 1062–1071 (1982).
- [57] S. Coen, A. H. C. Chau, R. Leonhardt, J. D. Harvey, J. C. Knight, W. J. Wadsworth, and P. S. J. Russell, "Supercontinuum generation by stimulated Raman scattering and parametric four-wave mixing in photonic crystal fibers," *J. Opt. Soc. Am. B* **19**(4), 753–764 (2002).
- [58] J. D. Harvey, R. Leonhardt, S. Coen, G. K. Wong, J. C. Knight, W. J. Wadsworth, and P. S. J. Russell, "Scalar modulation instability in the normal dispersion regime by use of a photonic crystal fiber," *Opt. Lett.* **28**(22), 2225–2227 (2003).
- [59] F. Biancalana, D. V. Skryabin, and P. S. Russell, "Four-wave mixing instabilities in photonic-crystal and tapered fibers," *Phys. Rev. E* **68**(4), 31–38 (2003).
- [60] R. A. Sammut and S. J. Garth, "Multiple-frequency generation on single-mode optical fibers," *J. Opt. Soc. Am. B* **6**(9), 1732–1735 (1989).
- [61] M. Yu, C. J. McKinstrie, and G. P. Agrawal, "Modulation instabilities in dispersion flattened fibers," *Phys. Rev. E* **52**(1), 1072–1080 (1995).
- [62] (<http://www.crystal-fibre.com/Products/nonlinear/datasheets/NL-PM-750.pdf>).
- [63] S. Diddams and J. C. Diels, "Dispersion measurements with white-light interferometry," *J. Opt. Soc. Am. B* **13**(6), 1120–1129 (1996).
- [64] H. Wenzel, A. Klehr, M. Braun, F. Bugge, G. Erbert, J. Fricke, A. Knauer, M. Weyers, and G. Trankle, "High-power 783 nm distributed-feedback laser," *Electron. Lett.* **40**(2), 123–124 (2004).
- [65] C. J. S. de Matos, K. P. Hansen, and J. R. Taylor, "Continuous wave, totally fiber integrated optical parametric oscillator using holey fiber," *Opt. Lett.* **29**(9), 983–985 (2004).

- [66] M. Karlsson, "Four-wave mixing in fibers with randomly varying zero-dispersion wavelength," *J. Opt. Soc. Am. B* **15**, 2269–2275 (1998).
- [67] Y. Jeong, J. K. Sahu, D. N. Payne, and J. Nilsson, "Ytterbium-doped large-core fiber laser with 1.36 kW continuous wave output power," *Opt. Express* **12**(25), 6088–6092 (2004).
- [68] J. Limpert, T. Schreiber, T. Clausnitzer, K. Zöllner, H. J. Fuchs, E. B. Kley, H. Zellmer, and A. Tünnermann, "High power femtosecond Yb-doped fiber amplifier," *Opt. Express* **10**(14), 628–638 (2002).
- [69] J. A. Alvarez-Chavez, H. L. Offerhaus, J. Nilsson, P. W. Turner, W. A. Clarkson, and D. J. Richardson, "High-energy, high-power Ytterbium-doped Q-switched fiber laser," *Opt. Lett.* **25**, 37–39 (2000).
- [70] L. A. Zenteno, H. Po, and N. M. Cho, "All-solid state passively Q-switched modelocked Nd-doped fiber laser," *Opt. Lett.* **15**, 115–117 (1990).
- [71] R. Paschotta, R. Häring, E. Gini, H. Melchior, and U. Keller, "Passively Q-switched 0.1 mJ fiber laser system at $1.53\mu\text{m}$," *Opt. Lett.* **24**, 388–390 (1999).
- [72] V. N. Filippov, A. N. Starodumov, and A. V. Kir'yanov, "All-fiber passively Q-switched low-threshold Erbium laser," *Opt. Lett.* **26**, 343–345 (2001).
- [73] M. Laroche, A. M. Chardon, J. Nilsson, D. P. Shepherd, and W. A. Clarkson, "Compact diode-pumped passively Q-switched tunable Er-Yb double clad fiber laser," *Opt. Lett.* **27**, 1980–1982 (2002).
- [74] A. A. Fotiadi, P. Mégret, and M. Blondel, "Dynamics of a self-Q-switched fiber laser with a Rayleigh-simulated Brillouin scattering ring mirror," *Opt. Lett.* **29**(10), 1078–1080 (2004).
- [75] S. V. Chernikov, Y. Zhu, J. R. Taylor, and V. P. Gapontsev, "Supercontinuum self-Q-switched Ytterbium fiber laser," *Opt. Lett.* **22**(5), 298–300 (2005).
- [76] L. Luo and P. L. Chu, "Passive Q-switched Erbium-doped fibre laser with saturable absorber," *Opt. Commun.* **161**, 257–263 (1999).
- [77] A. Chandonnet and G. Larose, "High power Q-switched Erbium fiber laser using an all-fiber intensity modulator," *Opt. Eng.* **32**, 2031–2035 (1993).
- [78] N. A. Russo, R. Duchowicz, J. Mora, J. L. Cruz, and M. V. Andrés, "High efficiency Q-switched Erbium fiber laser using a Bragg grating-based modulator," *Opt. Commun.* **210**, 361–366 (2002).

- [79] P. Pérez-Millán, A. Diez, M. V. Andrés, D. Zalvidea, and R. Duchowicz, “Q-switched all-fiber laser based on magnetostriction modulation of a Bragg Grating,” *Opt. Express* **13** (2005).
- [80] R. Kashyap, *Fiber Bragg Gratings* (Academic Press, 1999). Chapt. 5.
- [81] [Http://etrema-usa.com/products/terfenol/](http://etrema-usa.com/products/terfenol/).
- [82] Y. Wang and C. Q. Xu, “Switching-induced perturbation and influence on actively Q-switched fiber lasers,” *J. Quantum Electronics* **40**, 1583–1596 (2004).
- [83] G. Agrawal, *Applications of nonlinear fiber optics* (Academic Press, 2001).
- [84] C. C. Cutler, “Why does linear phase shift cause mode-locking?” *J. Quantum Electronics* **28**, 282–288 (1992).
- [85] D. Huang, W. Liu, and C. C. Yang, “Q-switched all-fiber laser with an acoustically modulated fiber attenuator,” *IEEE Phot. Tech. Lett.* **12**, 1153–1155 (2000).
- [86] Y. Sintov, O. Katz, Y. Glick, S. Acco, Y. Nafcha, A. Englander, and R. Lavi, “Extractable energy from Ytterbium-doped high-energy pulsed fiber amplifiers and lasers,” *J. Opt. Soc. Am. B* **23**, 218 (2006).
- [87] H. Deyerl, N. Plougmann, J. B. Jensen, F. Floreani, H. R. Sørensen, and M. Kristensen, “Fabrication of advanced Bragg gratings with complex apodization profiles by use of the polarization control method,” *J. Appl. Optics* **43**, 3513 (2004).
- [88] (<http://www.exfo.com>).
- [89] D. Ouzounov, D. Homoelle, W. Zipfel, W. W. Webb, A. L. Gaeta, J. A. West, J. C. Fajardo, and K. W. Koch, “Dispersion measurements of microstructured fibers using femtosecond laser pulses,” *Opt. Com.* **192**(3-6), 219 (2001).
- [90] D. Müller, J. West, and K. Koch, “Interferometric chromatic dispersion measurement of a photonic band-gap fiber,” *Proceedings of Spie, Active and Passive Optical Components for WDM Communications II* **II**, 4870 (2002).
- [91] (<http://www.crystal-fibre.com/datasheets/HC-1060-02.pdf>).
- [92] (<http://www.corning.com/photonicmaterials/pdf/pi1441.pdf>).
- [93] (<http://www.corning.com/photonicmaterials/pdf/pi1446.pdf>).

- [94] (<http://www.koheras.com>).
- [95] A. Isomäki and O. G. Okhotnikov, “All-fiber Ytterbium soliton mode-locked laser with dispersion control by solid-core photonic bandgap fiber,” *Opt. Express* **14**, 4368 (2006).
- [96] P. Champert, V. Couderc, P. Leproux, S. Février, V. Tombelaine, L. Labonté, P. Roy, C. Froehly, and P. Nérin, “White-light supercontinuum generation in normally dispersive optical fiber using original multi-wavelength pumping system,” *Opt. Express* **12**, 4366–4371 (2004).
- [97] G. P. Agrawal, P. L. Baldeck, and R. R. Alfano, “Temporal and spectral effects of cross-phase modulation on copropagating ultrashort pulses in optical fibers,” *Phys. Rev. A* **40**, 5063–5072 (1989).
- [98] A. V. Husakou and J. Herrmann, “Supercontinuum generation, four-wave mixing, and fission of higher-order solitons in photonic crystal fibers,” *J. Opt. Soc. Am. B* **19**, 2171–2182 (2002).
- [99] T. Schreiber, J. Limpert, H. Zellmer, A. Tünnermann, and K. P. Hansen, “High average power supercontinuum generation in photonic crystal fibers,” *Opt. Commun.* **228**, 71–78 (2003).
- [100] ([Http://www.femtosecondsystems.com](http://www.femtosecondsystems.com)).
- [101] G. Cerullo and S. Silvestri, “Ultrafast optical parametric amplifiers,” *Review of Scientific Instruments* **74**, 1–18 (2003).
- [102] G. M. Gale, M. Cavallari, T. J. Driscoll, and F. Hache, “Sub-20 fs pulses tunable pulses in the visible from an 82 MHz optical parametric oscillator,” *Opt. Lett.* **20**, 1562–1564 (1995).
- [103] R. Danielius, A. Piskarskas, A. Stabinis, G. P. Banfi, P. D. Trapani, and R. Righini, “Travelling-wave parametric generation of widely tunable highly coherent femtosecond light pulses,” *J. Opt. Soc. Am. B* **10**, 2222–2232 (1993).
- [104] S. Barkus, C. G. Durfee, M. M. Murnane, and H. C. Kapteyn, “High power ultrafast lasers,” *Review of Scientific Instruments* **69**, 1207–1223 (1998).
- [105] L. Goldberg, J. P. Koplow, and D. A. V. Kliner, “Highly efficient 4-W Yb-doped fiber amplifier pumped by a broad-stripe laser diode,” *Opt. Lett.* **24**, 673–675 (1999).
- [106] J. A. Armstrong, N. Bloembergen, J. Ducuing, and P. S. Pershan, “Interaction between light waves in nonlinear dielectric,” *Phys. Rev.* **127**, 1918–1939 (1962).

- [107] I. N. Ross, P. Matousek, G. H. C. New, and K. Osvay, "Analysis and optimization of optical parametric chirped pulse amplification," *J. Opt. Soc. Am. B* **19**, 2945–2956 (2002).
- [108] C. P. Hauri, P. Schlup, G. Arisholm, J. Biegert, and U. Keller, "Phase-preserving chirped-pulse optical parametric amplification to 17.3 fs directly from a Ti:Sapphire oscillator," *Opt. Lett.* **29**, 1369–1371 (2004).
- [109] (<http://www.sandia.gov/imrl/X1118/xxtal.htm>).
- [110] P. Baum, S. Lochenbrunner, and E. Riedle, "Generation of tunable 7-fs ultraviolet pulses : Achromatic phasematching and chirp management," *Appl. Phys. B* **75**, 427–443 (2002).
- [111] G. Cerullo, M. Nisoli, S. Stagira, and S. D. Silvestri, "Sub 8-fs pulses from an ultra broadband optical parametric amplifier in the visible," *Opt. Lett.* **23**, 1283–1285 (1998).
- [112] M. Drescher, M. Hentschel, R. Kleinberger, G. Tempea, C. Spielmann, G. A. Reider, P. B. Corkum, and F. Krausz, "X-ray pulses approaching the attosecond frontier," *Science* **291**, 1923–1927 (2001).
- [113] J. Limpert, A. Liem, M. Reich, T. Schreiber, S. Nolte, H. Zellmer, A. Tünnermann, J. Broeng, A. Petersson, and C. Jakobsen, "Low-nonlinearity single-transverse-mode Ytterbium-doped photonic crystal fiber amplifier," *Opt. Express* **12**, 1313–1319 (2004).
- [114] T. Clausnitzer, J. Limpert, K. Zöllner, H. Zellmer, H.-J. Fuchs, E.-B. Kley, A. Tünnermann, M. Jupé, and D. Ristau, "Highly efficient transmission gratings in fused silica for chirped pulse amplification systems," *Applied Optics* **42**, 6934–6938 (2003).
- [115] (<http://www.fiberdesk.com>).
- [116] A. Baltuska and T. Koayashi, "Adaptive shaping of two-cycle visible pulses using a flexible mirror," *Appl. Phys. B* **75**, 427–443 (2002).
- [117] J. M. Dudley and S. Coen, "Coherence properties of supercontinuum spectra generated in photonic crystal and tapered optical fibers," *Opt. Lett.* **27**, 1180–1182 (2002).
- [118] B. Schenkel, R. Paschotta, and U. Keller, "Pulse compression with supercontinuum generation in microstructure fibers," *J. Opt. Soc. Am. B* **22**, 687 (2005).
- [119] (<http://www.menlosystems.de>).

-
- [120] R. Oron and A. A. Hardy, "Rayleigh backscattering and amplified spontaneous emission in high power Yb-doped fiber amplifiers," *J. Opt. Soc. Am. B* **16**(5), 695 (1999).
- [121] A. Yariv, *Quantum Electronics*, 2nd ed. (John Wiley and Sons, 1967).
- [122] Y. Huo, R. T. Brown, G. G. King, and P. K. Cheo, "Kinetic modelling of high-power Ytterbium doped fiber lasers," *J. Appl. Optics* **43**, 1404 (2004).
- [123] J. W. Thomas, *Numerical partial differential equations: Finite difference methods* (Springer, 1995).
- [124] Centro de Investigaciones Ópticas, Camino Parque, 1900 La Plata, Argentina.